Microstructural Characterization of Aluminum Cables and Ultrasonically Welded Terminals for Electric/Hybrid Electric Vehicles

by

Brandon Hart

Submitted in Partial Fulfillment of the Requirements

for the Degree of

Master of Science in Engineering

in the

Mechanical Engineering Program

YOUNGSTOWN STATE UNIVERSITY

May, 2014

Microstructural Characterization of Aluminum Cables and Ultrasonically Welded Terminals for Electric/Hybrid Electric Vehicles

Brandon Hart

I hereby release this thesis to the public. I understand that this thesis will be made available from the OhioLINK ETD Center and the Maag Library Circulation Desk for public access. I also authorize the University or other individuals to make copies of this thesis as needed for scholarly research.

Signature:

Brandon D. Hart, Student Date

Approvals:

Dr. Virgil C. Solomon, Thesis Advisor Date

Dr. Hazel Marie, Committee Member Date

Dr. Pedro Cortes, Committee Member Date

Dr. Salvatore A. Sanders, Associate Dean of Graduate Studies Date

Abstract

Aluminum cables are much more cost effective and lightweight when compared to standard copper wiring. Without sacrificing conductivity, aluminum wiring can offer up to a 48% weight reduction versus copper wiring. This is particularly important in vehicle wiring, since any reduction in weight will improve fuel economy which will result in reduced carbon dioxide emissions. Although replacing copper wiring with aluminum wiring offers such advantages, it does come with its own set of challenges. One such challenge is creating successful terminal connections. Connecting aluminum cables to terminals by mechanical crimping is not nearly as effective as crimping copper cables to terminals. While crimping aluminum to terminals may work for smaller cables and wires, to connect larger aluminum cables, such as battery cables in vehicles, another method of connection should be used. A potentially effective connection alternative method is through ultrasonically welding the cables to the terminals.

Ultrasonic welding is a process of joining two overlapping metal pieces by applying pressure and high frequency vibrations to them, causing dynamic shear stresses high enough for plastic deformation to occur and bond the pieces. Aluminum and aluminum alloys are one of the most easily welded structural metals by this method. Since no electrical current actually passes through the aluminum being welded, the heat of the weld is not high enough to affect the mechanical properties of the welded sample. Ultrasonic welding does have some drawbacks, such as thickness limitations, but for the cables in this project, this limitation should not be a problem.

An area of particular interest in this project is the ultrasonic welding of aluminum and brass for aluminum cables/brass terminals applications in electric/hybrid electric cars. The purpose of this project is to understand the materials characteristics involved in the successful ultrasonic welding of aluminum cables to brass terminals used in electric/hybrid electric cars. In order to achieve this goal, three main research directions were pursued in this work. The first research project focused on the microstructural, chemical and surface characterization of aluminum wires to be used in manufacturing of aluminum cables for on electric/hybrid electric cars. The second project deals with the failure analysis of the ultrasonic welded aluminum cable/brass terminals. A side project was the microstructural characterization of impact modified polymers used in various applications in electric/hybrid electric vehicles. The materials to be investigated have been provided by a local company: aluminum cables (obtained for manufactures around the world), good and failed ultrasonic welded terminals, and impact modified polymers (manufactured at the local company).

Materials investigation was performed using a large array of analytical instrumentation and techniques, which include optical microscopy (OM), scanning electron microscopy (SEM), X-ray energy dispersive spectroscopy (XEDS), Auger electron spectroscopy (AES), X-ray diffraction (XRD), focused ion beam milling (FIB), and transmission electron microscopy (TEM).

Data analysis provided information on texture, chemistry and surface conditions (chemical composition and morphology) of the aluminum wires, the root cause of ultrasonic welding failure, as well as on the microstructure of the impact modified polymers. The results obtained in the present work might help the development of the applications of aluminum cable in electric/hybrid vehicles, in particular, and car industry, in general.

Acknowledgements

I would like to thank my father, Robin D. Hart III, for his unending support (even though we both knew his words of wisdom were cliché ridden BS, but they still helped), but without his assistance I never would have made it this far. I am proud to say that he is more than just my father, he is my best friend. Thanks for everything.

My grandparents, Robin D. Hart II and Joanne Leasure-Hart, also deserve a great deal of thanks for their support and (occasionally feigned) interest in my academics and research projects. The drive to make them proud of me kept me going through some of the rough times.

I definitely need to thank my advisor, Dr. Virgil C. Solomon, for always guiding me in the right direction and giving me new ideas when I was fresh out of them. I came to YSU with a lack of work ethic, but Dr. Solomon pushed me to be a harder worker and to be more professional. I hope that in the end I did not disappoint him. I appreciate everything he has done for me in these two short years.

I would like to thank Delphi, particularly George Drew and Gina Sacco, for giving me the opportunity to work on this ultrasonic welding project. I thoroughly enjoyed working on this project, and it gave me the chance to pursue my interests in electron microscopy.

I would also like to thank the Material Research Laboratory and Drew Hirt for the use of his Auger Electron Spectrometer and his assistance with the AES investigations. Drew, you undoubtedly have the coolest job ever.

Many thanks go to my thesis committee, Dr. Hazel Marie and Dr. Pedro Cortes. I know they both had busy schedules, but they took the time to be on my committee anyway.

Lastly I need to thank the Youngstown State University Mechanical Engineering Department for accepting me into its ranks, as well as the YSU Electron Microscopy Facility for giving me the chance to use the state-of-the-art equipment which I very much enjoyed working with.

Table of Contents

List of Figures

CHAPTER 1: INTRODUCTION

1.1 Aluminum Cables and Ultrasonic Welding of Aluminum

This project was a part of a larger work for a local company which was developing large size aluminum battery cables for electric/hybrid electric vehicles. This project was performed since replacing copper cables with aluminum cables would offer weight reduction and reduced cost in electric and hybrid electric vehicles. These cables would be attached to the battery terminals by ultrasonic welding due to the terminals being copper based, which is a dissimilar metal to the aluminum. The project encountered difficulties due to the ultrasonic weld joints. The project was then shared with Youngstown State University (YSU) to determine what was causing the inconsistent results. This investigation involved analyzing the base aluminum cables, provided by different manufacturers, the plastic coating on the cables, and finally the ultrasonic welds as themselves. The possible differences were analyzed by investigating the surface finish, crystallographic structure, and presence of an oxide layer on the aluminum wires of the cable, by using electron microscopy, X-ray diffraction (XRD), and Auger electron spectroscopy (SEM). The ultrasonic welds between the cable and the terminal were investigated by analyzing the weld interface by optical microscopy (OM) and electron microscopy.

Joining or adhesion of materials is one of the most important areas of fabrication and construction. The joining of dissimilar materials, which due to their nature do not bond well, is of particular interest in various industries. One method for joining dissimilar materials is ultrasonic welding[1]. Ultrasonic welding is not a direct replacement for conventional resistance welding or other welding methods, but is an alternative with its own distinct advantages and disasdvantages[2]. When compared to resistance welding, adhesive bonding, and brazing, ultrasonic welding is characterized by low input energy, low temperatures in the welding area, as well as short welding times which produce a solid state bond between the materials without melting those base materials[3,4]. When comparing ultrasonic welding to conventional resistance welding, power relationships for welding different materials are important to consider. For instance, welding aluminum by ultrasonic welding requires significantly less power than welding by resistance welding, but for making a similar weld with ferrous metals, the ultrasonic welder requires more power than the resistance welder[2].

The way ultrasonic welding works is by placing two materials which are to be joined together between what are known as an anvil and a horn. The anvil acts as a fixed base and the horn is connected to a transducer which applies an ultrasonic vibration at a set frequency. A pressure is applied to the horn in the direction of the subject materials and from this pressure and the ultrasonic vibration, the materials are welded together without fully melting the base materials[1].

1.2 Impact Modified Polymers

This sub-project was a part of another work performed by the same company that is working with ultrasonic welds. This project involved the analysis of the impact modified polymers for use in vehicle engines. These investigated polymers (nylon 6, nylon 6 6, and polybutylene terephthalate (PBT)) with different volume fractions of glass fiber were blended with an impact modifier. The modifier in these samples was polyolefin elastomers. The desired outcomes of this project was to successfully measure the length of the glass fibers in the blended samples which had been injection molded into tensile testing bars. Optical and electron microscopy was used to investigate and measure the lengths of the fibers. An additional goal of this sub-project was to prepare the samples in a way which would expose the distribution of the polymeric domains. This was done by trying various methods of polymer etching and then analyzing the sample surface with SEM.

Polymers are frequently used today because of their light weight, versatility and relative ease to manufacture. They are often weaker than traditional materials such as metals, so improving the strength and toughening properties is frequently an area of research. One method used to improve the impact strength of brittle polymers is to blend the base polymer with a type of rubber[5].

Polymer blends are notorious for being difficult to analyze with electron microscopy due to their similar electron densities, which makes their domains look the same. Additional difficulties are the charging and the sample surface damage resulting from the interaction of the polymers with the electron beam. Sample preparation methods of polymers for

electron microscopy imaging include staining and etching. A multitude of staining and etching techniques are available. To prevent charging of non-conductive samples imaged in the electron microscopes, in many cases the sample surface is coated with very thin layer of a conductive material[6].

CHAPTER 2: BACKGROUND

2.1 Aluminum Cables and Ultrasonic Welding of Aluminum

2.1.1 Aluminum Cables for Car Industry Applications

Two common trends in modern manufacturing are to reduce production costs and, especially in automotive manufacturing, to reduce the weight of the product. One way to achieve both goals is by replacing the copper wiring with aluminum wiring. In the current market, copper is slightly over 4 times more expensive than aluminum[7,8] and over 3 times as dense[9]. Figure 2-1 shows the approximate cost of aluminum and copper in US dollars over the past 5 years. This figure illustrates very clearly that although the price of both metals fluctuates, copper is always significantly higher.

When considering the two materials for electrical applications, the properties of each, especially the conductive properties, must be evaluated too. A research paper released by General Electric provided a concise comparison between the two materials. Since the material properties of both metals are dependent on the alloy used, common electrical application alloys were compared: cold worked copper alloy UNC C11000 and aluminum alloy 6101. The aluminum 6101 has only 56% conductivity of the copper alloy, which means that in order to achieve the same conductivity rating as the copper, the aluminum needs to have a larger cross section through which to pass current. Because of this, if space is an issue, copper is a better option, but even after the aluminum cross sectional

area increases to meet the coppers conductivity, the weight of the aluminum is still approximately half that of the copper[9].

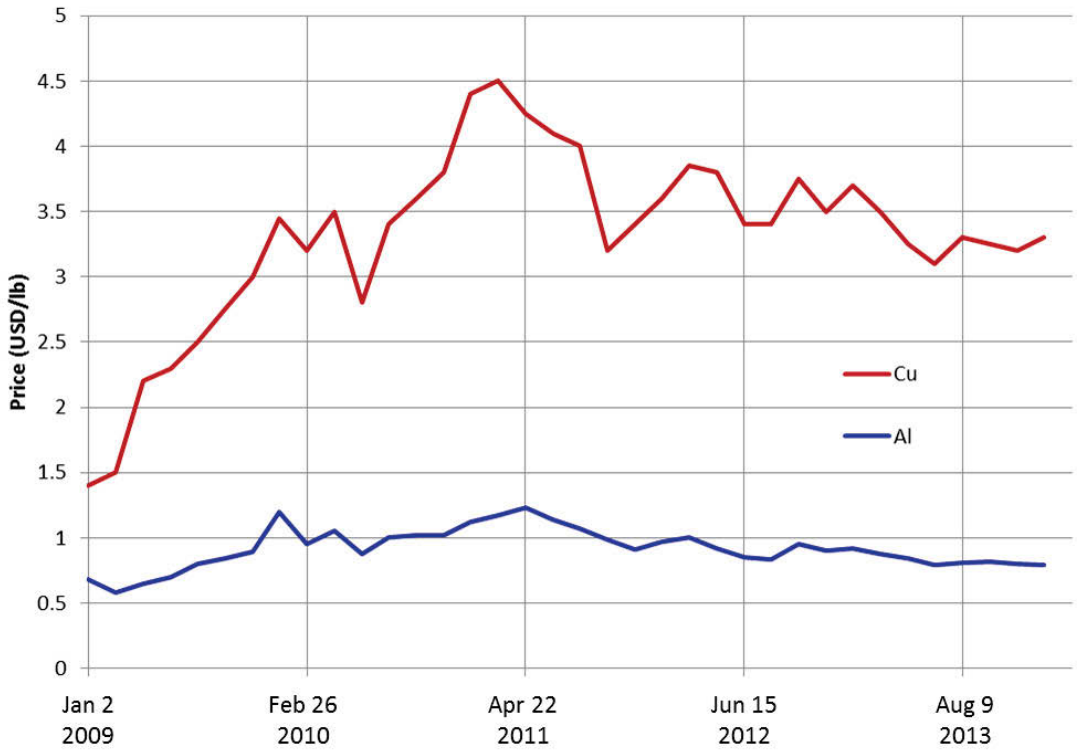

Figure 2-1: Approximate price chart of copper (Cu) and aluminum (Al) over a 5 year period[7,8].

While the General Electric paper compared specific alloys of aluminum and copper, as a general statement, aluminum is around 20 to 40 percent less electrically and thermally conductive than copper. Weighing this together with the price and density differences of both metals means that replacing copper wiring systems with aluminum wiring systems in automobile manufacturing would be a cost and weight reduction without sacrificing much electrical conductivity. The only problem is that some parts of the electrical system need to remain copper based, so an aluminum-to-copper joining technique would need to

be used such that the electrical continuity would not be interrupted[10]. Ultrasonic welding is an effective joining technique for dissimilar metals, such as aluminum and copper.

2.1.2 Introduction to Ultrasonic Welding of Aluminum

Ultrasonic welding was discovered during the Second World War by German engineers who were trying to use ultrasonics to improve the quality of weld in conventional resistance spot welds. Instead, they found that bonds could sometimes be created when the electrode was vibrated without a welding current. This phenomenon was later reviewed and further studied in the United States[11] and eventually the process of ultrasonic welding was introduced in the 1950s for joining small wires or thin metals together[12]. Currently, ultrasonic welding is known to be a joining method which excels at bonding the same metals together, as well as bonding dissimilar metals which may be unable to be joined by conventional resistance welding[13]. The process of ultrasonic welding is especially effective for joining aluminum (and its alloys) to itself, or to a dissimilar metal, like copper[4]. The joining of aluminum to copper is of significant interest because they have similar thermal and electrical conductivity, which is useful in many hybrid designs for lighter weight products such as automotive vehicles. This is due to aluminum being a lighter material than copper and also having slightly less, though still comparable, electrical conductivity. The problem with joining aluminum to copper, by conventional joining techniques like resistance welding, is that intermetallic compounds are formed very easily at the interface of the welded materials. Thus, ultrasonic welding

is a preferred method for joining these materials together due to its ability to easily join dissimilar metals, as well as not requiring flux for the bonding[1].

The process of ultrasonic welding is explained in depth in section 3.1.1.2, but a simple description is as follows: a power source supplies electrical energy to a transducer which converts that energy to mechanical vibration at a high frequency. This transducer is connected to the welding tip, or horn, and a clamping force is applied to the horn in the direction of the welder base, which is known as an anvil. The materials to be welded are placed between the horn and the anvil and are fixed in place by the clamping force from the horn. The mechanical vibrations, which oscillate in the plane of the materials to be welded, cause these materials, known as the work pieces, to be bonded together[2, 12].

The shear waves created by the vibrations acting between the work pieces, combined with the pressure from the clamping force cause local plastic deformation at the interface of the work pieces, which creates a metallurgical bond between the materials. Although this is the common explanation of the joining, there is still some debate over the actual mechanism. Various bonding mechanisms have been reported including the metallurgical bond from localized plastic deformation, as was just mentioned, along with local melting due to the heat of friction. Other less recognized theories have also been reported[12]. It has been shown through analysis of the welds that often the weld shows no evidence suggesting melting, which would support the claim of diffusion and plastic flow, but other analysis from welds created with high values of motion and stress occasionally show signs of some melting along with precipitation, recrystallization, and phase transformations[11].

The primary parameters in the ultrasonic welding process are the input power, frequency, clamping force, and weld time. For an optimum weld, each of these components are dependent on the material and the geometry of the pieces to be welded. In general, the power input is important since the vibration amplitude is directly related to the power, thus changing the power will change the stress at the weld interface. From this principle, the power should not be too high or the stresses in the weld will damage the weld, and conversely, if the power is too low the stresses will not be great enough to cause the materials to bond together[14]. Also within this general range, the material and geometry of the parts being welded determines how much power should be used. For harder and thicker work pieces, the power required to make a successful weld is greater than for thinner and softer materials. The principle for ultrasonically welding materials for different hardness is opposite to that used on conventional resistance welding. In resistance welding, more power is required to weld a softer material, such as aluminum, than for to welding a harder metal, like steel. This makes ultrasonic welding the preferable method over resistance welding for joining aluminum, especially if the aluminum parts are not very large[2]. When making an ultrasonic between materials with differing hardness, the power required to form the weld is the same as the power required to weld the harder material[14].

Ultrasonic welding has some limits which determine whether the material can be joined, and one of the major limitations is the part thickness. This limitation only applies for the part which is in contact with the welding tip; the part in contact with the anvil may be of any size or mass[11]. This limitation is because in thick samples the vibratory energy rapidly dissipates as it travels through the material. This is also why thicker parts require

more input power. Another reason for placing the thinner work piece in contact with the weld tip is because it has been found that when the thinner part is ultrasonically welded while placed between the thicker part and the anvil, the thin piece becomes highly deformed by the ultrasonic process[14].

The clamping force is another parameter which affects the welding quality. The main requirement of the clamping force is to restrain the pieces during the welding process, but like the other ultrasonic welding parameters, there is an optimal range for the amount of force used. When applying an excessive amount of force to the process, the weld tip can cause a significant amount of damage to the part which it is in contact with. On the other hand, if the clamping force is not large enough, the parts will slip across each other at the interface, which usually results in a lack of bonding[2].

Since most metals have a tendency to oxidize at their surfaces exposed to air (and aluminum not being the exception), this oxidation layer is usually an important variable in metal joining techniques. Ultrasonic welding, however, is a process where oxidation layers do not pose much of a problem. The friction between the work pieces caused by the high frequency vibration breaks up and disperses oxidation layers and some contamination. Because of this effect, cleaning work pieces is not required unless the contamination is significant, but cleaner surfaces of the work pieces produce a greater reproducibility, so even though part cleaning is not mandatory, it is recommended[21]. Since oxide layers have little effect on ultrasonic welds, it is not required that welding be performed in an inert atmosphere; although, this does not mean that ultrasonic welding is not able to be performed in other atmospheres. In certain applications where even small amounts of oxide are not desired, ultrasonic welding can be performed in the presence of

argon, or a similar inert gas, after the oxide layers have been previously removed[2]. Ultrasonic welding has also been shown to work adequately well in other environments as well, such as vacuum and even underwater. Studies have shown that welding in a water bath produces welds of a similar quality to welds in air, but they require a slightly longer weld time to achieve the same weld strength. In a study of ultrasonically welding aluminum to copper, the weld required a weld time of one second in the water bath, as compared to the weld time of half of a second in air, to reach the maximum producible weld strength under the same input parameters of the welder[1].

Contamination may not have a significant impact on the weld quality, but surface conditions do. The surface conditions of both the work pieces and weld anvil have an effect on the quality of the weld. Since the quality of a weld is determined by its performance in shear tests, the weld strength is the critical characteristic which determines the breaking point of a weld[2]. It was found in a study that work pieces with rougher surfaces produced welds with lower breaking force than those obtained with polished or smoother work pieces. Oppositely, it was found that the breaking force was higher in welds which were performed with a rougher anvil than those made with a smoother anvil. The welds with a rougher anvil also had greater reproducibility[14].

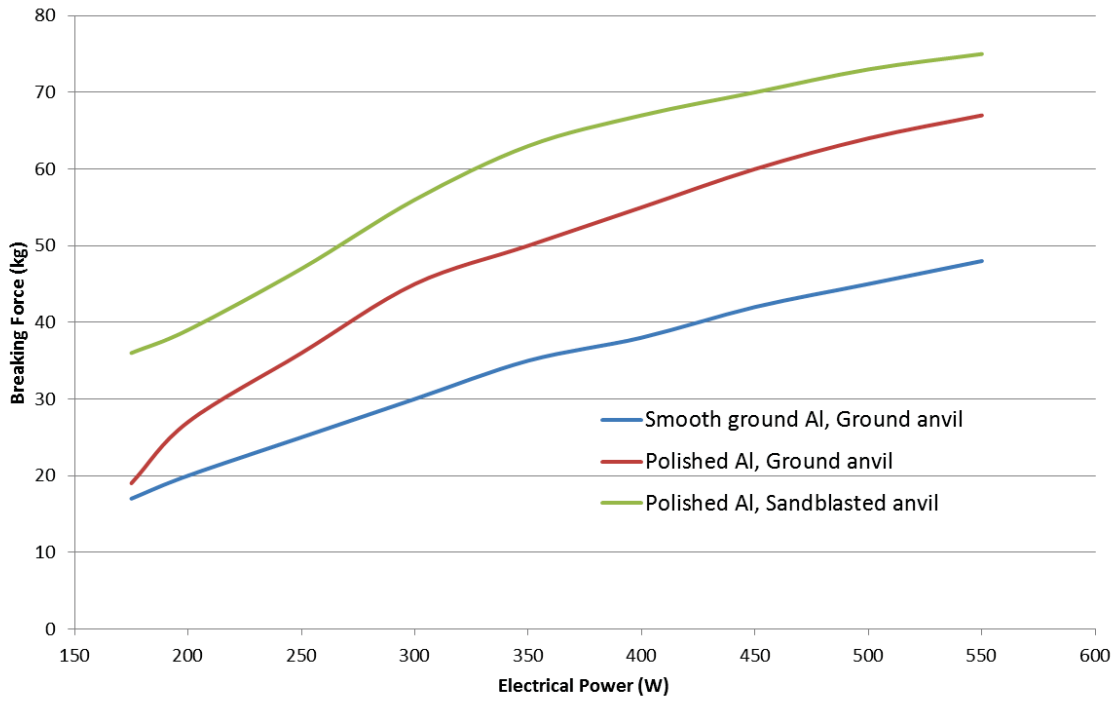

Figure 2-2: Graph showing weld strength as a function of input electrical power. This graph compares the welds made with two different roughnesses of the aluminum work pieces as well as welds made with two different anvil roughnesses. In this study, 'polished Al' is smoother than 'smooth ground Al', and 'ground anvil' is smoother than 'sandblasted anvil'[14].

Ultrasonic welding is not considered a replacement for conventional resistance welding, and ultrasonic welding is not to be thought as "better" process than resistance welding. Each welding method has its own advantages and disadvantages depending on the application. Some of the advantages of ultrasonic welding have been previously mentioned, such as the joining of dissimilar metals, but ultrasonic welding is also known for its low weld temperature. The amount of heat generated from the ultrasonic process is significantly less than the melting temperature of the parts (aluminum, specifically, only generates around 50% of its melting temperature during ultrasonic welding). This is a good property to have when welding materials which are heat sensitive, since the heat

generated is rarely high enough to affect the mechanical properties of the material. Also, ultrasonic welding does not create a cast nugget at the weld site like resistance welding does, which is an advantage for the ultrasonic method since weld nuggets can be the point of weakness in a welded joint. The absence of this cast nugget in ultrasonic welding is due to its low welding temperature characteristic, which also is why this process does not create any heat affected zones or impose grain growth.

Another advantage that the ultrasonic welding has over resistance welding is the fact that work piece surface cleaning is not required. In both methods, degreasing is considered a necessity, but removal of mild oxidation is much more important to resistance welding than it is in ultrasonic welding. Also, when referring to part cleaning, in ultrasonic welding cleaning is only performed on the part surfaces which contact each other, while in resistance welding it is important to clean both the interface as well as the outer surfaces of the work pieces[2]. There are also no contamination issues associated from the actual ultrasonic process since no electric current flows through the weld area. By contrast, the flow of current in the weld zone during resistance welding can cause contamination from sparking and/or arcing[11].

None the less, resistance welding has some major advantages over ultrasonic welding, such as the work piece thickness. In these terms, the ability to weld parts ultrasonically depends only on the thickness of the part in contact with the welding tip, while the limiting thickness for resistance welding is governed by the total thickness of both work pieces. Also, for good quality ultrasonic welds, the parts to be welded need to have smooth surfaces devoid of numerous pits or wrinkles at the interface, while in resistance welding, smooth part surfaces are recommended but in most cases not necessary[2]. These

differences between the two welding methods shows that each has advantages and limitations that will determine which is better suited for a specific application.

2.1.3 Literature Review of Finite Elemental Analysis of Ultrasonic Welding

Modeling of ultrasonic welding has been performed by Elangovan, *et al*[15] to simulate the temperature and stress distributions in the work pieces during the ultrasonic process. The model was designed as a simple welder setup which consisted of two work pieces, a welding tip, and an anvil, and this was simulated in 2D using ANSYS 8.0. The materials used for the weld tip and anvil were steel and the work pieces were thin plates of aluminum and copper. There, the copper was the part in contact with the anvil. Assumptions in the model were made to simulate typical weld conditions, and include perfect contact between the work pieces, uniform cross section area of the weld tip, and room temperature was taken to be 30°C and uniform. Another important assumption in this model is that the area of the welding tip is equal to the area of plastic deformation in the work piece interface, and this area is assumed to be the area of the weld itself. This simulation modeled the welding process, which started at room temperature and ran for a typical welding time of 0.5s. The model was simulated for various clamping forces, work piece thickness, and coefficient of friction between work pieces, to see how these properties effected the temperature distribution. The simulation was also observed at various times between 0 and 0.5s to determine the variation of temperatures as a function of time.

The first result of this simulation showed that when the clamping force was set to 1600N, a maximum temperature of 336.816°C at the weld interface was observed at the end of a

full 0.5s weld. This distribution is shown in Figure 2-3 A, which shows that the highest temperatures remain almost exclusively in the designated deformation area. It was also determined from this first simulation, by plotting the maximum temperature at each time step, that the variation of temperature during the welding is proportional to the weld time. In this first simulation, the Von-Mises stress distribution was found, and this is shown in Figure 2-3 B. It can be seen in this figure that the work pieces are being lifted away from the anvil due to the clamping force. It was suggested that a work piece geometry with a specific fixture needs to be used to keep the parts from moving away from the anvil. It can also be seen in the same figure that a maximum Von-Mises stress of 0.5×10^7 N/m^2 is located at the very center point of the welding tip.

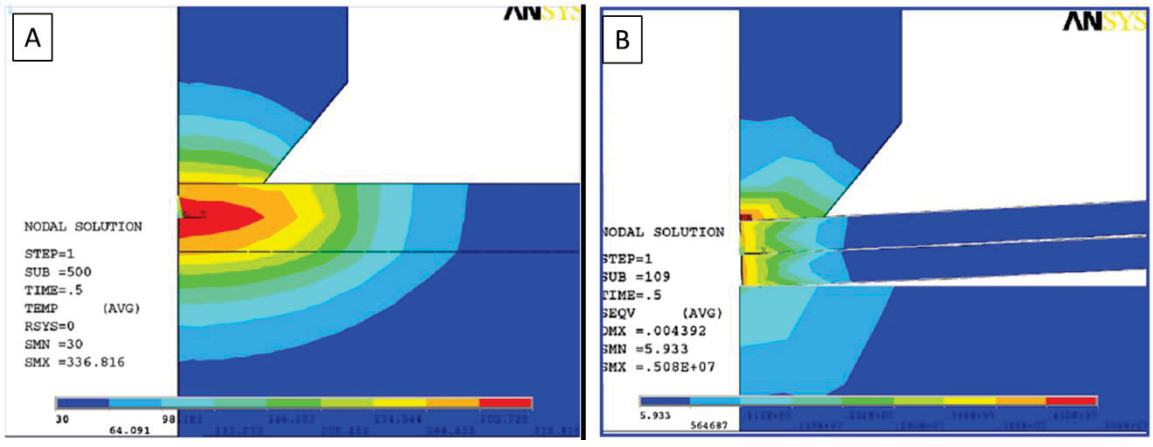

Figure 2-3: FEA analysis of a typical ultrasonic welder setup. (A) Temperature distribution, (B) Von-Mises stress distribution and part deformation[15].

The next simulation analysis was carried out by changing the other variables, clamping force, part thickness, and coefficient of friction between work pieces. The results of varying the clamping force show that applying less clamping force increases the weld temperature and lowers the Von-Mises stress at the interface. The lower temperature for

higher clamping force is due to the fact that the temperature at the interface is dependent on the weld force on the parts, and when the clamping force is higher, the weld force is lessened. When the part thickness was varied, it was found that thicker parts have lower weld temperatures, which is possibly due to the diffusion of heat over the larger area. It was inferred that for aluminum work pieces of thickness greater than 3mm, under the conditions used in this simulation, the heat generation at the weld interface is not enough to consistently weld the material. It was also found that higher coefficient of friction, which represents rougher aluminum part surfaces, increases the amount of heat generated at the weld. It was also inferred that surface films at the work piece interface will reduce the friction and therefore could lower the heat generation[15].

2.1.4 Literature Review of the Microstructure of Ultrasonic Welding of Aluminum

One study involving optical microscopy (OM) and orientation imaging microscopy (OIM) was performed on a cross-sectioned ultrasonic spot weld of an aluminum alloy by Kenik and Jahn[16]. This study showed that by OM, the grains of the base metal were obvious but the grains of the weld zone were not clear. Because of this, OIM was used to determine the grain structure of the weld zone. OIM is an electron microscopy technique which uses electron back-scattered diffraction patterns collected from a sample which is tilted to a certain angle. The collected pattern is analyzed and shows the orientation and microstructure of the grains in the sample[17]. The sample used by Kenik and Jahn was a cross section of an ultrasonic weld which was electropolished to minimize any deformation from the sample preparation. The results from OIM showed that the

misorientation across grain boundaries increased closer to the weld zone. It was also shown that the grains closer to the weld zone continually decreased in size, but the grain size at the weld zone boundary for the upper piece decreased sharply. The diameters of the grains at the weld zone boundaries were measured to be approximately 1 μm. There were also some sub-micron grains observed, but due to the pixel spacing of the OIM analysis, the sizes of these sub-micron grains could not be accurately measured. Though these sizes could not be accurately measured, the analysis showed highly random orientations of these small grains which would suggest recrystallization in the weld zone[16].

Another study on the microstructure of ultrasonic welds was performed by Allameh *et al*[18] using OM and transmission electron microscopy (TEM). This investigation also analyzed the polished cross section of an aluminum ultrasonic weld. The OM analysis showed weld zones, weld affected zones, and compression zones. The compression zones were considered as the areas at the interface where no weld was observed, and the grains, while typical of the bulk aluminum in size, were deformed from the compression and shear forces induced by the welder. These deformed grains were elongated parallel to the interface of the parts and were approximately 20-50 μm by 100-150 μm. The welded zones were the areas where flow of the material was observed by markings of a swirling flow pattern. These weld areas are seen as a circular core with the flow markings curving around this core. The core itself lacks distinguishable grains; it is possible that the grains in these areas were broken down from the welding process to a size that is not visible in OM. The cores and the flow swirls around them are spaced along the weld interface, scaling with the spacing of the ridges on the welder tip. Since the quality of the weld

depends on the quality of the interfacial strength, it is likely that optimizing the weld tip's geometry and texture will increase the interfacial strength, and therefore the quality of the weld. The last designated area were called weld affected zones, and were places where the grains near weld zones were either broken into smaller grains or were deformed differently than the elongated grains in the compression zones. These weld affected zones are located between the weld zones and the areas unaffected by the welding process.

The same sample used for the OM analysis was also used for the TEM analysis. A section in a weld zone was chosen for the TEM sample. The TEM sample was removed from the OM sample by focused ion beam milling (FIB). The TEM analysis of the welded zones showed that while grains were not visible in OM, they were revealed by TEM to be as small as 500-1000 nm. At a higher magnification, a selected area diffraction pattern (SADP) was performed and the result showed a crystalline structure with nano-scale sized grains. The variation of the grains in this sample would suggest a large amount of local structural deformation. Also, crystal defects, such as dislocations, were discovered by observing Moiré fringes at the boundaries of cellular structures found in certain areas of the TEM sample. These dislocations were not resolved due to the thickness of the TEM sample in this study[18].

2.2 Impact Modified Polymers

Polymers are very useful materials due to their versatility. To extend their usefulness, strengthening of polymers is an extensively researched field. The strengthening of polymers often results from blending a base polymer with other materials which exhibit properties that the original lacks[5].

Nylon 6, nylon 6,6, and polybutylene terephthalate (PBT) are a group of polymers which are commonly used for automotive engine parts. These polymers are known for their good strength and stiffness even at higher temperatures[19]. To obtain better impact properties in a polymer, such as the three systems previously mentioned, blending with various rubbers has proved to be effective. Commonly, rubbers used as modifiers of these polymers include: elthylene propylene dicyclopentadiene (EPDM)[20], acrylonitrile/butadiene (NBR)[21], carboxylated styrene-butadiene rubber (CSBR)[22], and styrene-ethylene-butylene-styrene (SEBS)[23]. The modifying properties depend on the mechanical properties of the material as well as their microstructure. The properties of the additives which have been found to be particularly influential on impact strength are the particle stiffness and particle size[22]. Another important property of the blend is the interparticle distance, which is determined by the particle size and the volume fraction of the rubber. This interparticle distance controls the temperature where the polymer makes the transition between brittle and tough. For smaller interparticle distances, the brittle-tough (BT) transition temperature lowers, and when this BT transistion temperature decreases the polymer exhibits better impact behavior[24].

This brittle to tough transition seems to be caused by crazing and shear yielding deformation mechanics. When crazing is the cause for failure, the fracture type is brittle, and when shear yielding is the cause of the failure, the fracture type is tough. When observing the fracture area of these two different fracture types, the tough fracture showed no visible rubber particles, while the brittle fracture showed rubber particles at the fracture surface. This suggests that for brittle type fractures, the crack follows the rubber particle matrix, and for tough fractures the crack avoids the rubber particles and

follows the base polymer matrix[25]. In polymers, this BT transition occurs at a specific temperature. For these rubber blended impact modified polymers, it is desired to have a lower BT transition temperature so that the fracture type is tough for the temperature at which the polymer will be used at. When below the BT transition, plastic deformation occurs before the crack happens, which causes it to break easily, therefore, 'brittle'. When above the BT transition, the plastic deformation happens as the crack propagates, slowing the break down, which is considered 'tough'. It has been found that higher volume percent of rubber in a polymer, such as nylon, will lower this BT transition temperature, as shown in Figure 2-4 A[26].

It was also found that the particle size of the rubber affects the BT transition temperature. The rubber particle size can be varied by changing the barrel temperature of the rubber extruder. It is shown in Figure 2-4 B that the smaller the rubber particle size, the lower the BT transition temperature. When the particle size is too large, the BT transition temperature is the same as the glass transition temperature of the base polymer (particle size of 1μm or more, for nylon 6) and the aim of increasing impact strength has been nullified. There are also limits to how small the rubber particles can be and to how high the rubber percent volume can be. For example, as the concentration of rubber increases, the BT transition temperature of the blend decreases, but at some point in this relation, the BT temperature for the blend is lowered to the point of the glass transition temperature of the rubber, and any further increase in rubber concentration will have no effect[25].

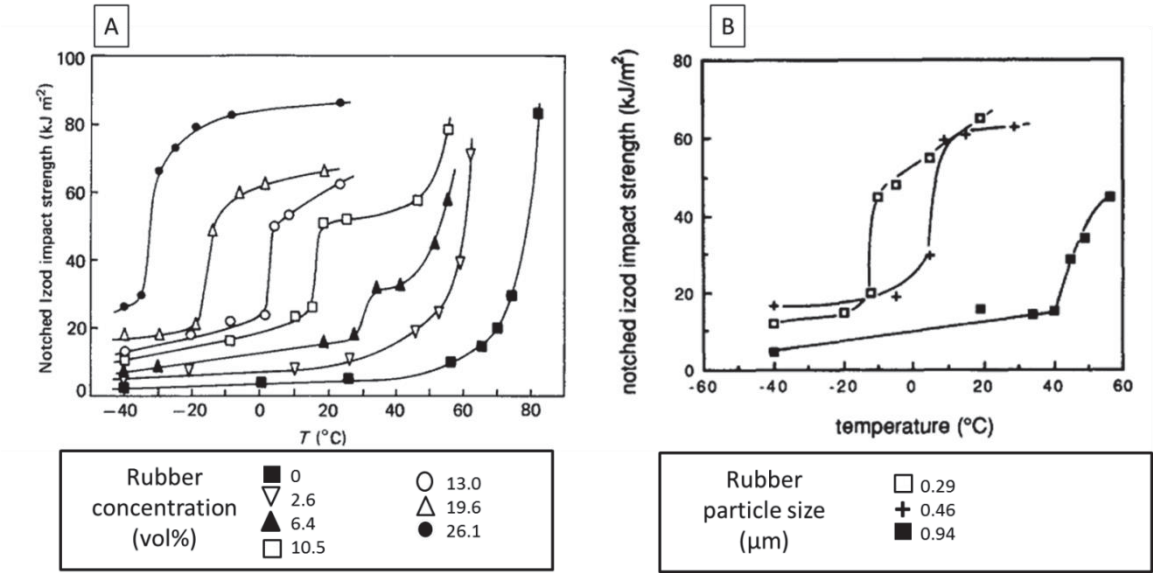

Figure 2-4: Graph of impact strength against temperature where, (A) rubber concentration volume is varied and rubber particle size is held constant[25], and (B) rubber particle size is varied and rubber concentration volume is approximately held constant[26].

The mechanism which causes the rubber to improve toughness is still debated, but a few theories are more accepted than others. One of these theories, it is suggested that the mechanism which makes blended rubber toughen a polymer is the ability of the rubber particles to generate stress concentrations around themselves within an applied stress field due to the difference in modulus of the rubber and polymer matrix. The rubber particles' stress fields will begin to overlap if the particles are close enough together, and the overlapping stress fields will further increase the toughening of the polymer blend. Another opposing theory is that the rubber particles' stress concentrations do not toughen the polymer, but instead the toughening of the polymer is due to the cavitation of the rubber particles. The idea behind this is, if the particles were rigid or if they were voids, they would not be able to stop cracks or sustain loads imposed in the deforming, but when the rubber particles cavitate to create voids this will relieve local hydrostatic

tension[26]. When tested with this idea in mind, it appeared that the stress concentration fields from other nearby rubber particles did not have an effect on the voiding in or around the particle, nor was it influenced by the particle size[24].

For imaging polymers with electron microscopy, specifically scanning electron microscopy (SEM), viewing features, such as domain morphology, have proved to be somewhat difficult without the aid of other analytical methods and sample preparation. The problem with viewing polymers with SEM lies with synthetic polymers having very slight variation in electron density, which creates a lack of contrast between polymer phases in the microscope. Another problem which arises in SEM imaging of polymers is that at higher voltages the electron beam can cause charging in the sample as well as impose beam damage to the sample[6]. To help with the viewing of polymers in the SEM, multiple methods can be employed, such as staining or etching the sample. Staining a polymer sample will help develop contrast differences in the different domains or phases (unless the domains of a polymer blend are of a similar chemical structure), while etching will remove one domain and leave the other relatively untouched. To avoid charging of the polymer sample, the surface of the sample can be sputtercoated with a layer of conductive material, usually gold or another highly conductive metal. To avoid surface damage to the sample induced by the electron beam, the voltage of the beam can be lowered, but this comes at a cost of reducing the quality of the image.

Here, the focus will be on the method of etching, in which there are two different ways to etch the materials of a polymer sample: chemical etching and plasma/ion etching. In chemical etching, the chemical used to etch the polymer is often an acid, which diffuses into a specific region and breaks down the material[6]. The acid used should be specific to

the material that is desired to be removed while not reacting with the other. For example, formic acid is often used to dissolve nylon 6 and nylon 6,6[27,28], while PBT can be selectively etched with potassium hydroxide[29]. After chemical etching, the dissolved material is washed away so that the remaining domain is all that is left behind. By viewing this remaining structure or matrix, it clearly shows how the two polymers are blended together. Another method of etching is with plasma or ion etching, in which the sample is bombarded with charged particles to remove atoms from the sample surface. In terms of sample preparation, etching is the most prone method to produce artifacts in polymers. These etch induced artifacts appear as ripples, striations, or corrugations and are typically either 5-20nm or 100nm and greater in size. When the texture falls into the lower range of size, the features are more likely to be indicative of the materials microstructure, while the 100nm and greater features are commonly found to be artifacts from etching. Artifacts are usually reduced on a sample which has smoother sample surface. Also, when compared to ion etching, plasma etching imposes fewer artifacts and they are less directional. Care must be taken for all etching processes, as other analytical techniques may be required to determine the actual polymeric structure since etching can obscure the finer component details of the sample[6].

CHAPTER 3: EXPERIMENTAL

3.1 Sample Preparation

This chapter will detail the materials obtained for analysis, as well as the reasoning and procedure for the various analytical methods used. This chapter will also give a brief description of the main instrumentation techniques which were used in the analysis.

3.1.1 Aluminum Cables and Ultrasonically Welded Terminals

The samples for analysis were obtained from the local company running the project. Looking for an explanation for why they were not getting consistent results in their ultrasonic welds of aluminum cable to brass (which is an alloy made from copper and zinc) terminals, the first batch of samples for testing were cables from the six different aluminum cable manufacturers they had been using. Three of the six of these cables are shown in Figure 3-1 A. The process by which these cables were made is outlined later in section *3.1.1.2*. These cables were to be analyzed for any possible differences which could be causing better or worse ultrasonic welds. These cables were analyzed for the quality and composition of the surface of the wires which make up the cable by scanning electron microscopy (SEM), energy dispersive X-ray spectroscopy (EDS), Auger electron spectroscopy (AES), and X-ray diffraction (XRD).

Another set of samples were received at a later time, which included several ultrasonic welds of the aluminum cables to brass terminals. The cables used in these welds, were

one of the previously analyzed cables, specifically the one manufactured by the company's local plant. The samples in this group included two sets of welded samples, where one set of weld samples were considered successful and the other one was considered unsuccessful. The consideration of 'successful' and 'unsuccessful' welds was determined by whether the weld passed the local company's shear test. In this test, the weld was pulled in tension from either end until the weld separated. Depending on the amount of force required to break apart the weld, the sample either passes or fails the test. The naming convention used for these samples was based on the cable insulation color, where the weld samples from the group which passed the shear test had red insulation, and the weld samples from the failing group had pink insulation. Therefore, within this work, the samples will be referred to as 'red' and 'pink' for the successful and unsuccessful weld, respectively. One sample of each is shown in Figure 3-1 B. The analysis of these terminals was performed by exposing the weld interface and observing it with optical microscopy (OM) and SEM.

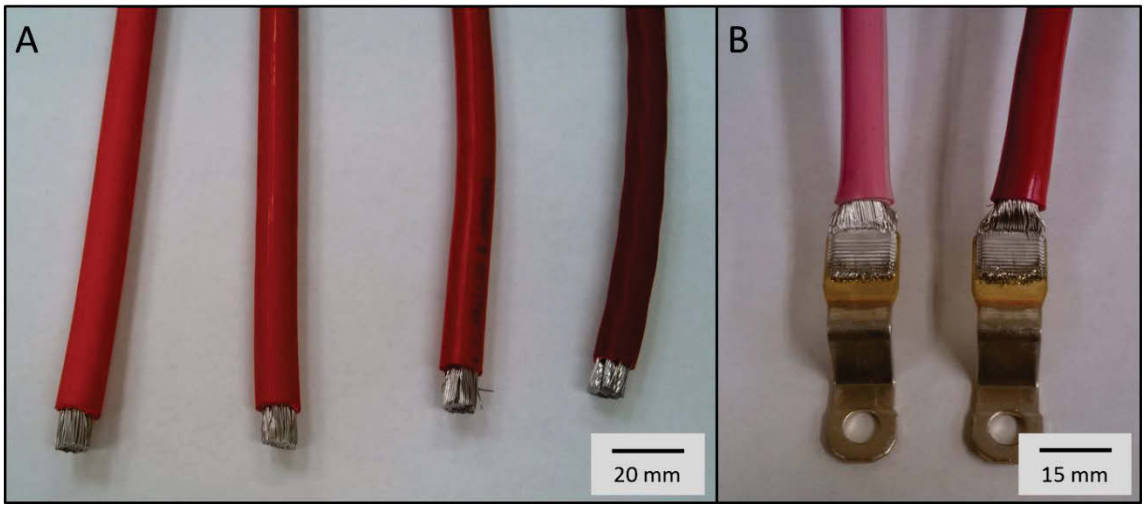

Figure 3-1: (A) Four of the six unwelded aluminum cable samples. (B) One of the sets of ultrasonic welded samples. Based on the shear test, the left weld (pink insulation) was considered a 'fail' while the right weld (red insulation) was considered a 'pass'.

3.1.1.1 Wire Drawing

The aluminum cables analyzed in this project were made by bundling aluminum wires. These aluminum wires were manufactured by drawing. Drawing is a process in which a material, usually a metal, is pulled through a hole in a drawing die which has a smaller area than the material being fed into it. This reduces the cross section area and elongates the length. This process can be done repeatedly, causing a larger piece of material to be manufactured into a very long, thin wire.

In the die, compressive forces act on the material in two directions (σ_2 and σ_3 shown in the upper right corner of Figure 3-2) while in the third direction (σ_1 in Figure 3-2) is applying tension. A simple approximation of the drawing force can be found by the equation:

$$F = a_f \times Y \times \ln\left(\frac{a_o}{a_f}\right) \tag{3.1}$$

where a_o is the original cross sectional area, a_f is the cross sectional area after drawing, and Y is the mean yield stress of the metal. The ratio (a_o/a_f) is known as the drawing ratio and is usually between 1.25 and 1.3 in industry.

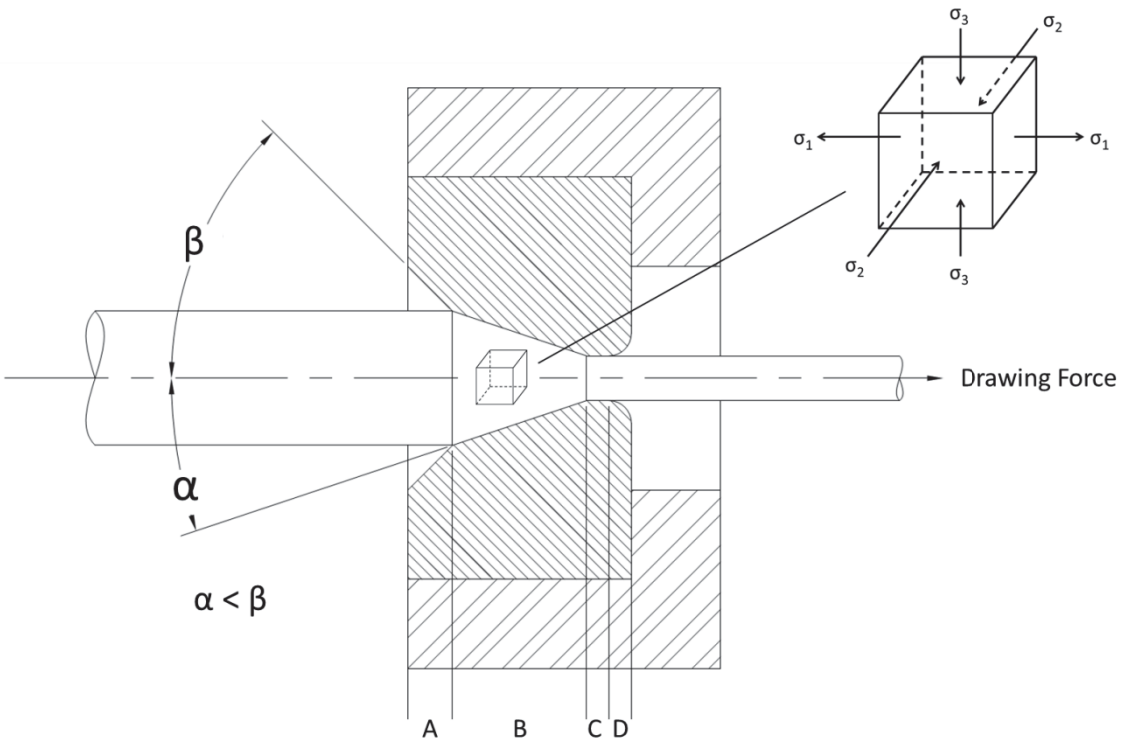

Figure 3-2: Diagram of a drawing die with zones labeled as A) entry zone, B) working zone, C) die bearing, and D) exit zone. The stress cube in the upper right corner shows how the forces act on the material as it goes through the die[30].

The metal which is to be drawn is called a blank. Before drawing, the blank material is first heat treated, then descaled since the process of heat treating causes scaling of the metal surface. Pickling is the most common method of descaling; it often involves applying acid to the material. After descaling, the material is cleaned of residues from pickling and is quickly dried to avoid what is known as pickling brittleness.

When the material is ready to be drawn, the end which is to be pulled through the die is brought to a long point by hammering, which is known as swagging, so it can be easily fed through the die and grabbed by the pulling mechanism. The die itself has four zones: entry zone, working zone, die bearing, and exit zone, as shown in Figure 3-2. The entry

zone is an opening larger than the blank which allows lubricant to reach the working zone and also keeps the material from being scored from sharp edges. The working zone is the area which reduces the material. This zone is tapered at an angle of anywhere from 6° to 24°, which is dependent on the material that is being drawn. The zone after the working zone is the die bearing. The die bearing is a short section which is not tapered and is the cross sectional area of the exiting material. This zone is used to define the dimensions of the wire accurately. The final zone is the exit zone, which has a sloping opening at the back to avoid scoring that would result if the exit had sharp edges. All these die zones are a part of the die body which is enclosed in a steel piece with high toughness, known as a die holder.

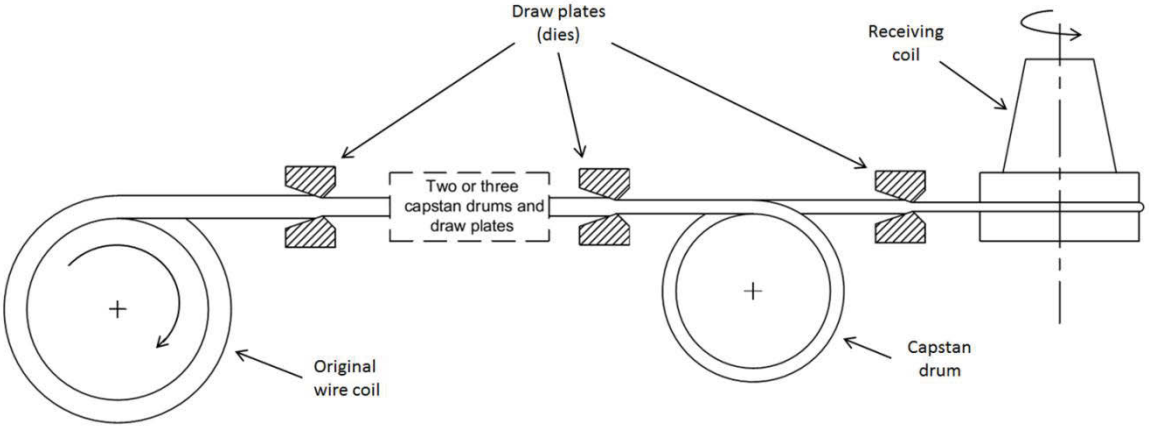

Figure 3-3: Diagram of a drawing bench[30].

Since one pass through a die usually isn't much of a reduction, multiple passes are often required. Multi-draw setups are called draw benches; an example is shown in Figure 3-3. Between each drawing die, the wire is coiled around a drum, known as a capstan, two or three times. Draw benches can consist of anywhere from two to twenty-two dies. The

more times the wire is drawn, the faster the wire exits the bench and this speed can approach 50 m/s. The metal is drawn by this process until the desired final wire diameter is acheived[30].

3.1.1.2 The Process of Ultrasonic Welding

The process of ultrasonic welding can be used for various types of welds and connections, including regular spot, overlapping spot, continuous seam welds, as well as connecting cables and wires to terminals. The general design and mechanics of the ultrasonic welder are nearly the same for each type of connection type. This design has the materials which are to be welded pressed between the anvil, which is a solid surface acting as a base, and the horn, which is the welding tip. A transducer is attached to the horn which converts a high frequency power, usually between 10,000 and 60,000 Hz, to vibratory power. This vibratory power causes the horn to oscillate parallel to the weld interface. The shear waves created by this oscillation, along with the pressure applied to the materials, causes dynamic shear stresses in the interface which leads to local plastic deformation resulting in a bond between the base materials without melting them[2].

Transducers are the primary drive of the ultrasonic welder. The transducer is the part which takes the AC electrical energy and converts it into the mechanical energy which creates the vibratory motion of the machine. The transducers are made of components which are magnetostrictive or electrostrictive. Between these two, magnetostrictive transducers are more commonly used due to the fact that their materials are more resistive to the mechanical and thermal damages brought on by the process. The transducer is then coupled to the horn in a certain arrangement, and a clamping force is applied to the horn

perpendicularly to the plane of the work pieces. The arrangement of the transducer and horn can vary depending on the desired type of ultrasonic weld, but for standard spot welds and wire joining, the setup has the transducer parallel to the work pieces and clamping force applied perpendicular at the end of the horn, shown in Figure 3-4 A. Another setup has the transducer perpendicular to the work pieces with the clamping force applied through the transducer and into the work pieces, shown in Figure 3-4 B. This particular arrangement makes controlling the frequency difficult since the clamping force applies pressure on the transducer, and without good frequency control, the welds become difficult to reproduce.

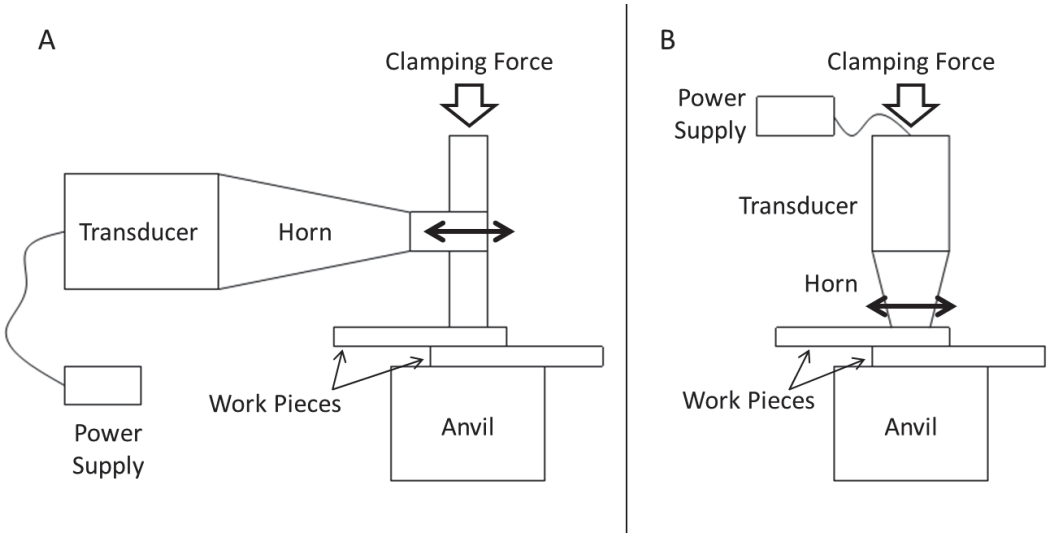

Figure 3-4: Simple diagram of two common ultrasonic welder setups. See text for details.

The anvil of the welder is the fixed base which the weld materials are clamped to, and the geometry of the anvil is only important for very specialized applications. The primary requirement of the anvil is to make a solid base for the materials to be clamped upon which is massive and ridged enough to not be affected by the vibrations of the horn. The clamping force, on the other hand, is more specified to the materials being welded. Also,

depending on the size of the welder, different systems can be used to deliver the clamping force. In larger welders the force is often supplied by hydraulics, in medium sized welders the force system can be pneumatic, while in smaller welder setups, where the work pieces do not require a significant force to be welded, a simple spring-actuated system is sufficient.

The welding tip can have varying shapes depending on the weld type, and depending on the material being welded, the material of the weld tip can be different. In ultrasonic welding, the weld tip, as well as the anvil face to a lesser extent, can experience wear, but this can be reduced by choosing an appropriate material for the weld tip. For ultrasonically welding aluminum, a tip made of high speed tool steel is sufficient. The last important setup condition for the ultrasonic welder is the weld timing system. After the materials are mounted and the clamping force is applied to the work pieces, the vibratory action of the weld is timed to make the strongest weld quality before the vibration is stopped. The amount of time required for a quality weld depends on many factors, which include the amount of power supplied, the frequency of the welder, the type (or types) of material being welded, and the thickness of the work pieces. Due to the high number of variables in the determination of weld time, the time required for a simple spot weld, for example, can range from 0.005 seconds to 1.2 seconds[2].

3.1.1.3 Aluminum Cable and Ultrasonically Welded Terminal Sample Preparation

The six aluminum cable samples prepared for SEM and AES analysis were simply individual wires cut from the cable bundle at a length of approximately an inch. These inch long wires were attached to the instrument's stage oriented so that the wires surfaces

would be analyzed. For the AES analysis, a single wire was taken from the outer edge of the bundle for each cable and was screwed to the stage for the Physical Electronics Industry PHI 660 AES used for this analysis. For the SEM analysis, multiple wires were taken from each bundle in different areas to see if the wire surfaces within the same cable were different at various depths within the bundle. Also, while in the SEM, the elemental composition of the samples was also analyzed for any contamination or inclusions on the aluminum. The SEM used for this analysis was a JEOL JIB 4500 Multi-Beam System equipped with an EDAX Apollo SDD EDS and the OM was the Zeiss Axiophot.

Samples for the XRD analysis were set up in two different ways. One way was to analyze the longitudinal orientation along the wires, and the other was to analyze the cross section of the wires. The longitudinal set up was prepared similar to the samples for SEM and AES, with many short pieces of the individual wires being laid flat in the XRD sample cup. These wires were held into the cup with wax and for minimizing the amount of wax being measured in the XRD, the wires were packed tightly together side by side, as shown in Figure 3-5 A. The cross sectional setup was different. The idea was to compare the XRD results from the wire surface (longitudinal) with aiming at the cross sectional cut of the wires. To analyze the cross section of the wire by XRD, a two inch section was cut off the end of the full cable and this section was mounted in epoxy. After the epoxy was fully set, a small slice of the mounted cross section was cut out by a Buhler IsoMet 1000 Precision Saw and polished smooth with a Struers PLANOPOL-2 grinding and polishing wheel. This slice was thin enough to fit in the XRD sample cup and was mounted such that the incoming x-rays would strike the face of the wire bundle cross

section. The embedded section of cable and the slice for XRD are shown in Figure 3-5 B. The XRD used for this analysis was Bruker D8 Advanced which uses Cu-K_α radiation.

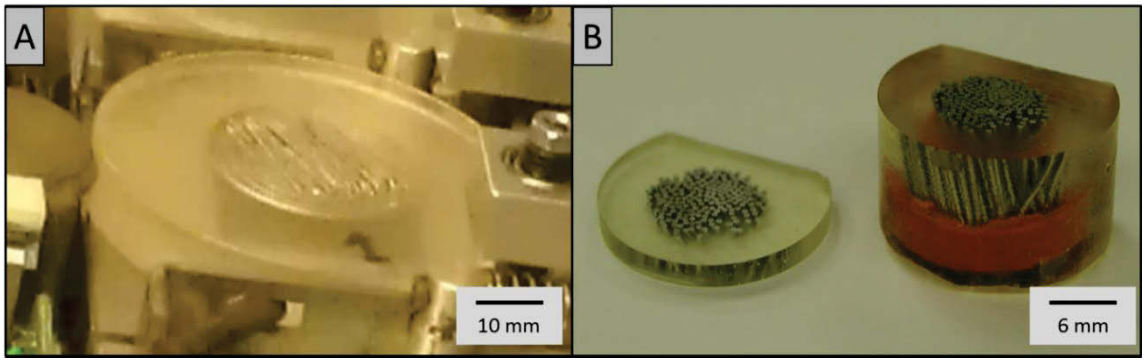

Figure 3-5: (A) Aluminum wires longitudinally mounted in XRD sample cup. (B) Section of aluminum cable which was embedded in epoxy with a thin slice taken out.

The second sample set of samples included the ultrasonic welds of the aluminum cable with the brass terminal. These samples were aluminum cables from the same manufacturer, welded ultrasonically to brass terminals, where one sample had passed the test for a successful weld and the other had not. As designations for the samples, the successful weld had red insulation covering the cable and the failed weld had pink insulation covering the cable. Before analyzing the weld itself, the aluminum cable was cut from the weld and it was analyzed by SEM and EDX in the same manner as the previous six cables. These cables were analyzed more thoroughly than the previous cables, by specifically selecting four equally spaced wires from the outside of the cable bundle.

For analysis of the weld zone, the weld interface needed to be exposed. This was done by cutting off the majority of the unwelded terminal plate and unwelded aluminum cable with a hacksaw. To cut the cable off from the weld, the hacksaw cut needed to be

performed approximately 5-10mm into the polymer insulation to prevent the aggressive cutting from ripping the wires out of the weld. All four samples, two red and two pink, were cut this way. The first method of exposing the weld interface involved mounting the sample in epoxy for easier sectioning. After the epoxy had hardened, the samples were cut with a low speed saw across the weld, using a diamond coated blade, through the middle, and then cut again along the weld through the center. The sample after cutting is shown in Figure 3-6 A. The sample was cut this way so that during the analysis of the weld interface, the interface could be also examined for any differences between the longitudinal cut face and the transverse cut face. These samples were observed by OM and SEM. Since these samples were embedded in a polymer epoxy, the samples needed to be sputtercoated with gold palladium in the Polaron Instruments Inc. SEM Coating Unit E5100 sputtercoater to avoid charging in the SEM from the polymer.

The other red and pink weld samples were not embedded in epoxy, because it was later determined that for better analysis the weld interface could be cut and polished by focused ion beam milling (FIB). For this process, it was decided that the sample should not be embedded in epoxy due to the charging effect of polymers in the SEM, which would make the FIB work more difficult. So the unembedded weld samples were carefully cut with the diamond saw as shown in Figure 3-6 B. One piece of the cut was mounted to an SEM stub which was cut at a 45° angle so the FIB would be angled to mill across the surface of the weld interface. The sample was mounted so the FIB would mill across the cross-sectional face of the terminal cut and expose the interface of the metals at a much higher degree of polishing than the polishing wheel could achieve.

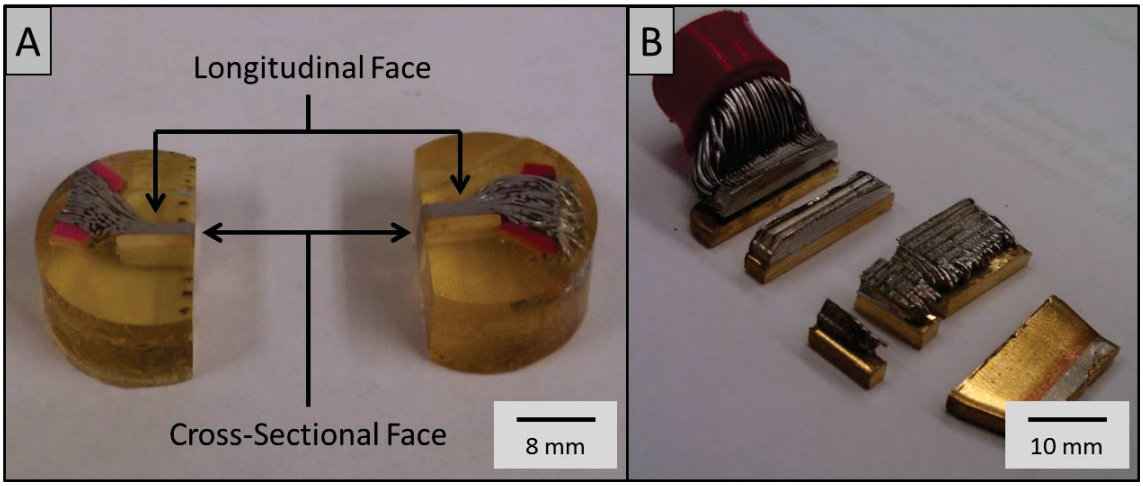

Figure 3-6: (A) Ultrasonically welded terminals after being embedded in epoxy and cut across the weld area in two directions. (B) Ultrasonically welded terminal cut into pieces.

During the analysis of the FIB polished interface, it was determined that further analysis of the interface between the metals could be achieved by transmission electron microscopy (TEM). A TEM cross section sample was prepared from the FIB polished section at an area previously investigated by SEM. To make a TEM sample using the FIB, a protective layer of carbon is deposited over the area selected for the TEM sample. After that, a large box is milled above and below the selected spot, and then a small section is milled to one side of the sample. Finally the sample is tilted and the underside of the TEM sample is cut, leaving only one side still attached to the surrounding material, as is shown in Figure 3-7 A. Before making the last cut, a nano-manipulator Omniprobe is inserted and brought down to rest on top of the TEM sample and tungsten is deposited over the contact point of the Omniprobe to effectively weld the sample to the probe. Then the final side of the sample is milled away and the probe lifts the TEM sample out of the bulk specimen, as shown in Figure 3-7 B. The sample attached to the probe is then moved to a TEM sample holder and is attached to it with a spot of tungsten. The tip of the probe

is then milled off the sample and the probe is removed. To be analyzed in the TEM, the sample needs to be 100 nm thick or less to make it electron transparent. To thin the sample to this desired thickness, the FIB is used to slowly mill away the sides of the sample until it is thin enough. Lastly, the FIB is set to a small beam size and the acceleration voltage is lowered to polish both sides of the thin sample.

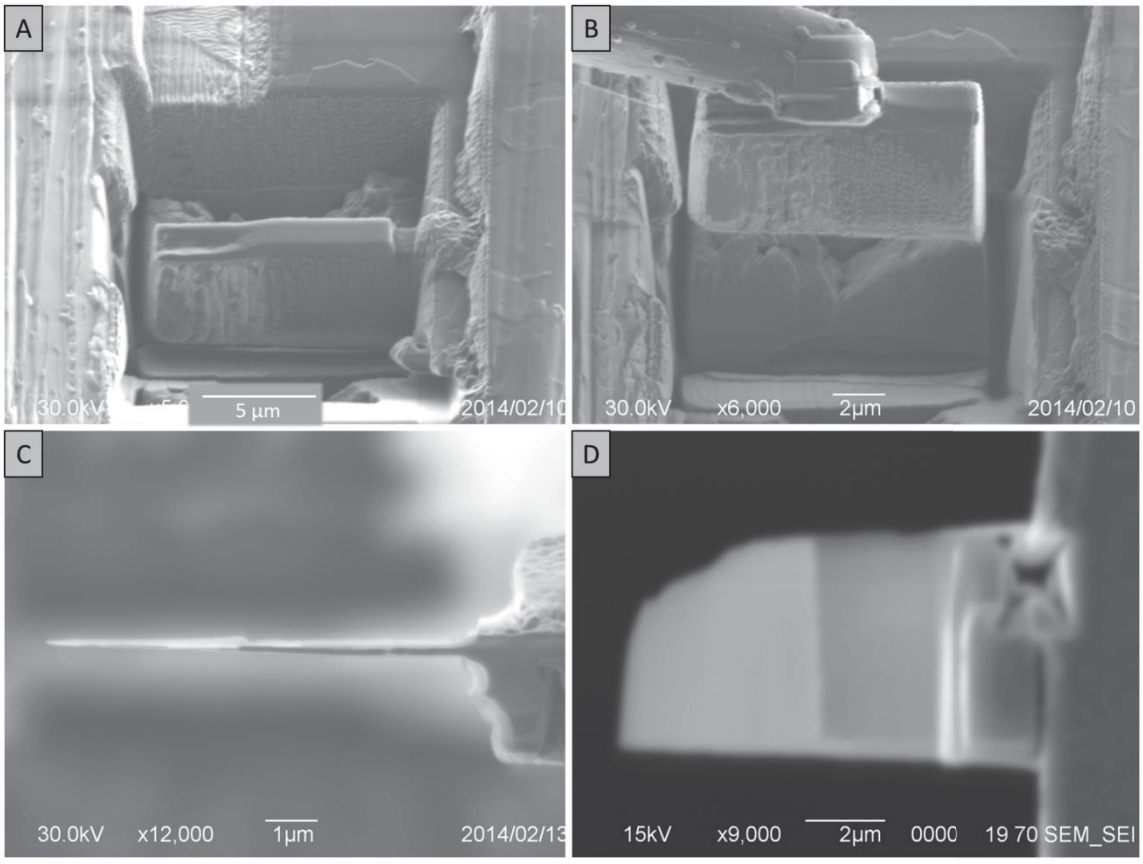

Figure 3-7: Preparing a TEM sample from the weld interface. (A) TEM sample mostly cut out from the interface. (B) TEM sample fully cut out and being lifted away with the Omniprobe. (C) FIB image of the top of the TEM sample attached to the TEM holder after being thinned to electron transparent thickness. (D) SEM image of the front of the thinned sample.

Along with the primary analysis of the ultrasonic weld interface, other experiments were performed to rule out other reasons for the welds being different. It was noticed in the

preliminary observation of the samples that the individual wires coming out from the insulation going towards the weld area were more spread out and tangled in the pink sample (from the failure group) than the red sample (from the pass group). This was thought to be a result of how well the cable's insulating cover was able to hold the wires in the bundle, so a chemical composition of the red and the pink insulation was performed by thermogravimetric analysis (TGA) to determine if there were any noticeable differences between the two insulations. For the TGA, a piece of pink and red insulation was stripped away from their respective cables and the pieces were broken up with a knife into tiny shavings. These shavings were to create more surface area of the sample for the TGA. The TGA used for this was TA Intruments TGA2050 Thermogravimetric Analyzer.

3.1.2 Impact Modified Polymers

The impact modified polymers were given by a group working at the research center of the same company which supplied the ultrasonic welding project. The samples to be analyzed were seven injection molded polymer bars with different base polymers and varying amounts of filler. The three base polymers were PA6 (nylon 6), PA66 (nylon 6,6), and polybutylene terephthalate (PBT), all blended with an impact modifier, and the fill was either glass fibers or glass beads and fibers. The samples, modified with polyolefin elastomers, and their fill amounts are outlined in the table below.

Table 3-1: Impact modified polymer samples

Sample #	Base Polymer	Fill Amount
1	PA6	Unfilled
2	PA6	30% filled
3	PA66	Unfilled
4	PA66	14% filled
5	PBT	Unfilled
6	PBT	20% filled
7	PBT	30% filled

The desired analysis on these samples included viewing and determining the polymeric domains between the base polymer and the impact modifier. It was also desired to get measurements of the fill fiber lengths.

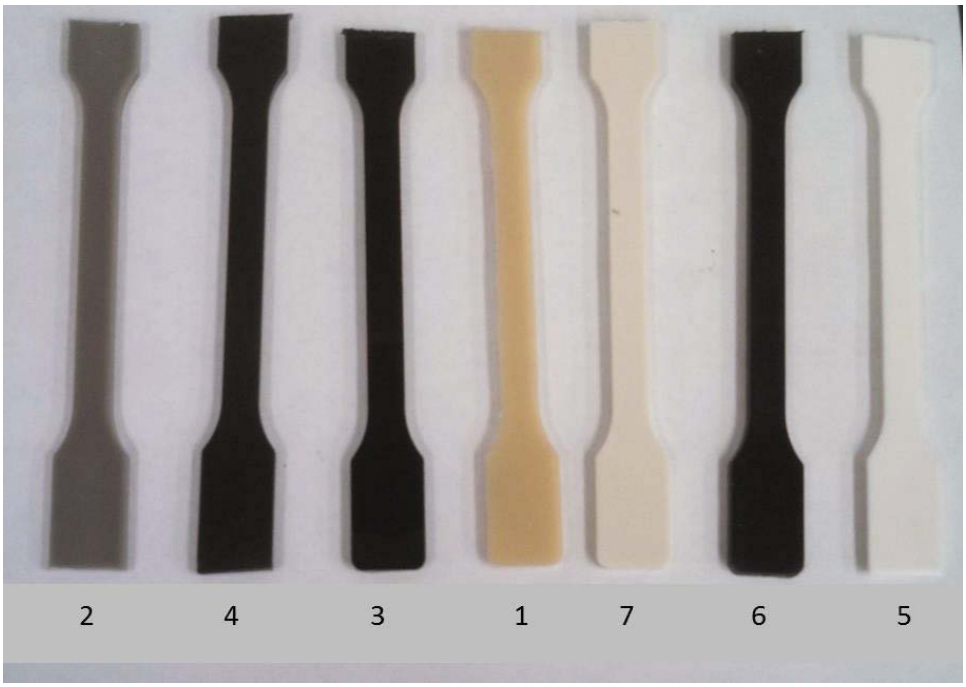

Figure 3-8: Impact modified polymer bars numbered according to Table 3-1.

3.1.2.1 Sample Preparation

Since imaging polymers in electron microscopes is not trivial, various methods were tried to get decent SEM images at various magnifications. Literature mentions that to view the polymeric domains, staining or etching the polymers is required to bring out the domains. The first attempt to view the polymers was without any staining or etching to get an idea of what the material looked like normally. This first attempt at viewing involved cutting a small section out of the injection molded bar with a hacksaw and then taking slices off the segment with a microtome. These microtome slices were then attached to SEM holder stubs with double sided carbon tape and then the edges were covered with copper tape and the whole stub was sputtercoated with gold-palladium to keep the sample from charging in the microscope. The cutting process and the mounted samples are shown in Figure 3-9.

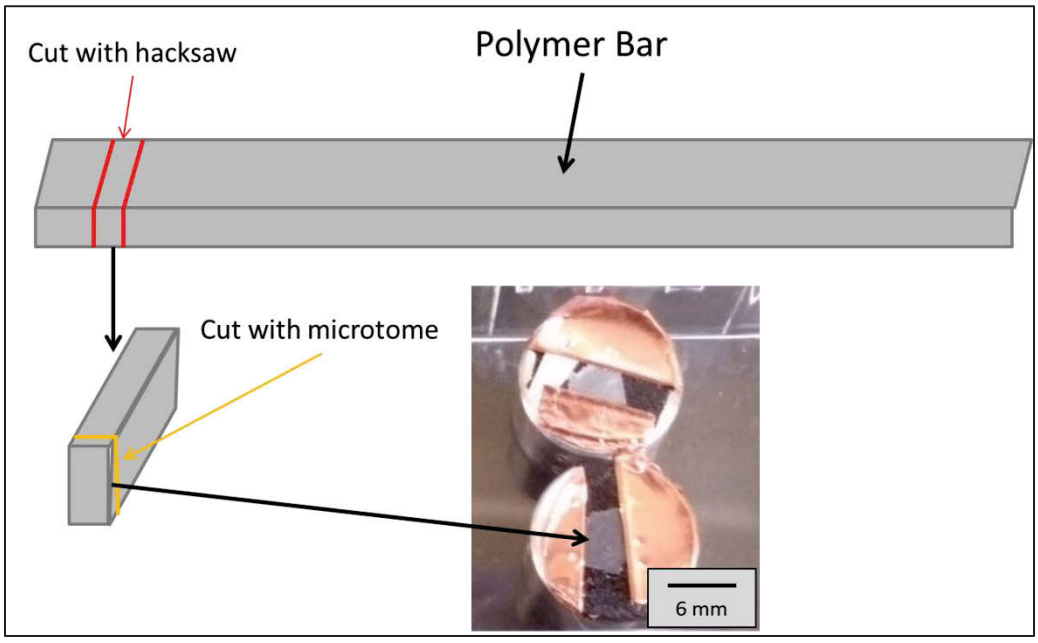

Figure 3-9: Diagram outlining how the microtome slices were taken from the polymer bars.

To bring out the domains in the polymer, literature suggests staining or etching. Etching was determined to be a preferential method. Etching polymers requires different methods for specific polymers and the first attempt to etch them involved chemical etching. Since PA6 and PA66 are both nylon based, they could both be etched by the same solution while the PBT needed another etching solution. It was found in literature that the nylon in PA6 and PA66 can be selectively etched with formic acid which would leave the blended impact modifier relatively untouched[27,28]. Similarly, the PBT could be selectively etched with potassium hydroxide[29]. Here, full concentration formic acid was used. Segments, which were approximately 5mm by 10mm, from each PA6 and PA66 sample were cut from the bar with a hacksaw and the rough edges were removed with a razor blade. These segments were placed in small beakers of full concentration formic acid and were left for about 10 hours. These samples completely dissolved, which left no surfaces to analyze. A second attempt involved cutting another piece from the polymers and placing a drop of full concentration formic acid on the surface for roughly a minute. Unlike the first attempt, this method left the piece intact, but the etched away material left a residue behind which left the surface difficult to view.

The literature also mentioned etching polymers by plasma etching[6]. Since the chemical etching was proving quite difficult, plasma etching was attempted. Plasma etching is not a selective type of etching, like chemical etching, but is useful because it will etch both polymers in the blend but one may be etched quicker than the other, leaving domains visible. Since this method is not targeting a specific polymer in the blend, both the nylon based and PBT based polymers could be etched this way. For this method, a Fischione Instruments Plasma Cleaner Model 1020 plasma cleaner was used since it uses the same

principle as a plasma etcher but is primarily used for removing surface contaminants from various samples. The plasma cleaner works by bombarding samples in the vacuum chamber with argon, which will remove small amounts of the material from the sample. More segments of the same size were cut from the bars and were attached with carbon tape to the small mounts which fit the plasma cleaners sample holder. The plasma cleaner is weaker than an etcher due to the fact that it is made for surface cleaning, so to compensate for this, the polymer pieces were left in the plasma cleaner for extended periods of time. The samples were run in the plasma cleaner for hour increments, and in between the hours they were quickly examined by OM. If the OM analysis did not show any change in the surface texture, then the samples were placed back in the plasma cleaner for another hour. This process was repeated until a slight texture was visible in an optical microscope. The total times of etching in the plasma cleaner were 4 hours for PA6 and PA66, and 3 hours for PBT.

To view and measure the glass fiber lengths in the filled samples, various methods were tried before finding a successful approach. The first attempt was to view them in the SEM from the microtome slices, but the force from cutting with the microtome broke up most of the fibers, so this method was not good. Next, larger pieces were cut from the injection molded bar and these were attached to the SEM holder stubs by the same process as the microtome slices. This way, the surface of the injection molded itself bar was viewed in the SEM, which should not have broken fibers. It was found by this method that the surface had very few visible fibers, and most of the fibers seen were not perfectly in the same plane as the surface, which made viewing complete fibers nearly impossible.

The final method yielded better results. This final attempt was to cut larger, more manageable pieces from the bar, then grind a thin layer from the bar surface and polish it quite smooth. These polished samples were observed by OM, where the fibers stood out much better than in the SEM. Analyzing these pieces in the OM was also much easier due to the fact that the samples didn't need to be prepared on SEM stubs with copper tape and sputtercoating to avoid charging.

3.2 Instrumentation

3.2.1 Scanning Electron Microscopy (SEM)

The scanning electron microscope (SEM) is an instrument for observing the microscopic structure of materials. This is done by focusing an electron beam on a sample and scanning it across the samples surface, which creates an image of the sample. Also by equipping the SEM with an energy dispersive x-ray spectrometer, the sample can be analyzed for its chemical composition.

The SEM works by emitting an electron beam from an electron gun, which is then focused by two condenser lenses and one objective lens to cause the beam to act as a probe. This electron beam probe has a diameter in the scale of nanometers. This probe is then scanned over the sample by using a beam deflection system in the objective lens and this moves the probe across the sample, then drops down one line and sweeps across again. During this process, electrons can be scattered elastically or inelastically. The elastically scattered electron is known as a backscattered electron (BSE), and the inelastically scattered electron is known as a secondary electron (SE). The BSE is the

electron from the electron beam which is scattered off from the surface of the sample, while the SE is an electron which was expelled from an atom in the sample due to the energy of the collision from the electron beam. Secondary electrons are useful for creating a topographic image. Backscattered electrons are used to show elemental composition contrast since the chance of generating a BSE is higher for elements with a larger atomic number. This creates contrast in the image since elements with higher atomic numbers generate more BSEs than elements with lower atomic numbers which makes the area where the electron originated brighter. Figure 3-10 shows where the detected SE and BSE originate from once the electron beam strikes the sample. The SEs have much lower energy than the BSEs, so even though they are emitted from the entire pear-shaped region, only the ones from a depth of 5-50nm are able to escape and reach the detector. The BSEs have nearly the same energy as the electron beam, so they are able to escape the sample from a higher depth of around 50-300nm[31].

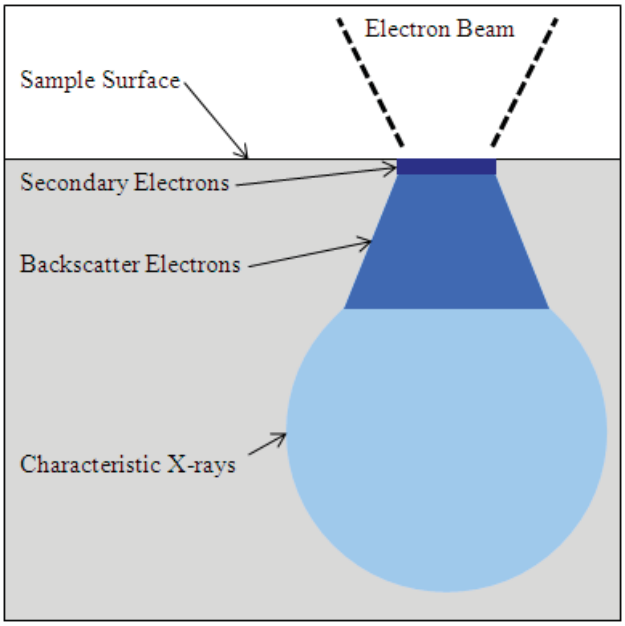

Figure 3-10: Diagram of where the electrons originate from in a sample[32].

It can also be seen in Figure 3-10 that X-rays are produced from the interaction of the electron beam and the sample. These X-rays are characteristic of the element from which they are emitted and can be used to determine the element. This process is done by an Energy Dispersive X-Ray Spectrometer, or EDS detector. EDS detectors are commonly integrated into SEMs for elemental analysis. The characteristic X-rays are collected by the detector and are shown as a spectrum, an example of an EDS spectrum is shown in Figure 3-11. The energy peaks in the spectrum are unique to the element and can be used to determine the composition of the material at the analyzed point. The downside to this method is that some energy peaks overlap others and may be overlooked. This is especially a factor when multiple peaks are generated by X-rays from different energy level shells. Besides elemental composition analysis at points or over an area, EDS can also perform line scans and can create composition maps. These are done by taking the spectrum at each point across the line or map and display the results for how the composition of the material changes through the line or area[33].

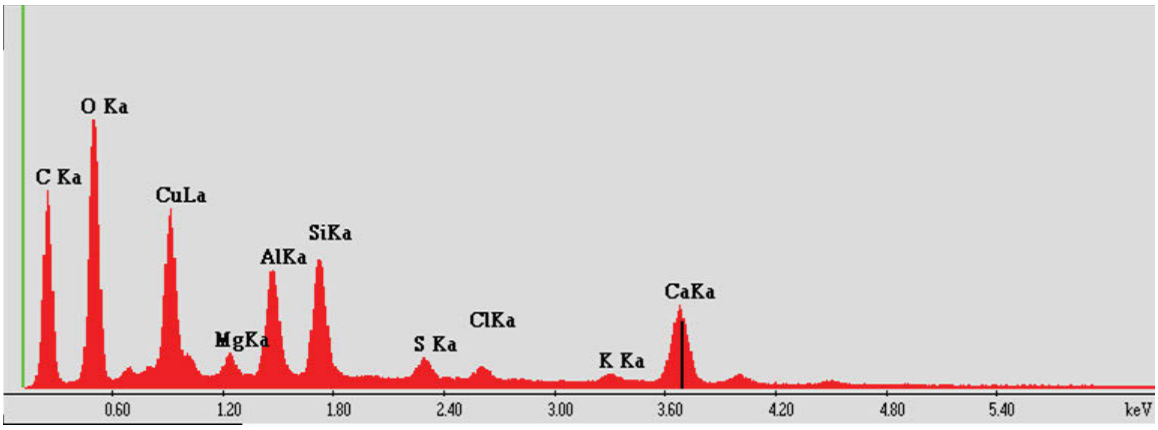

Figure 3-11: Example of a spectrum obtained by EDS.

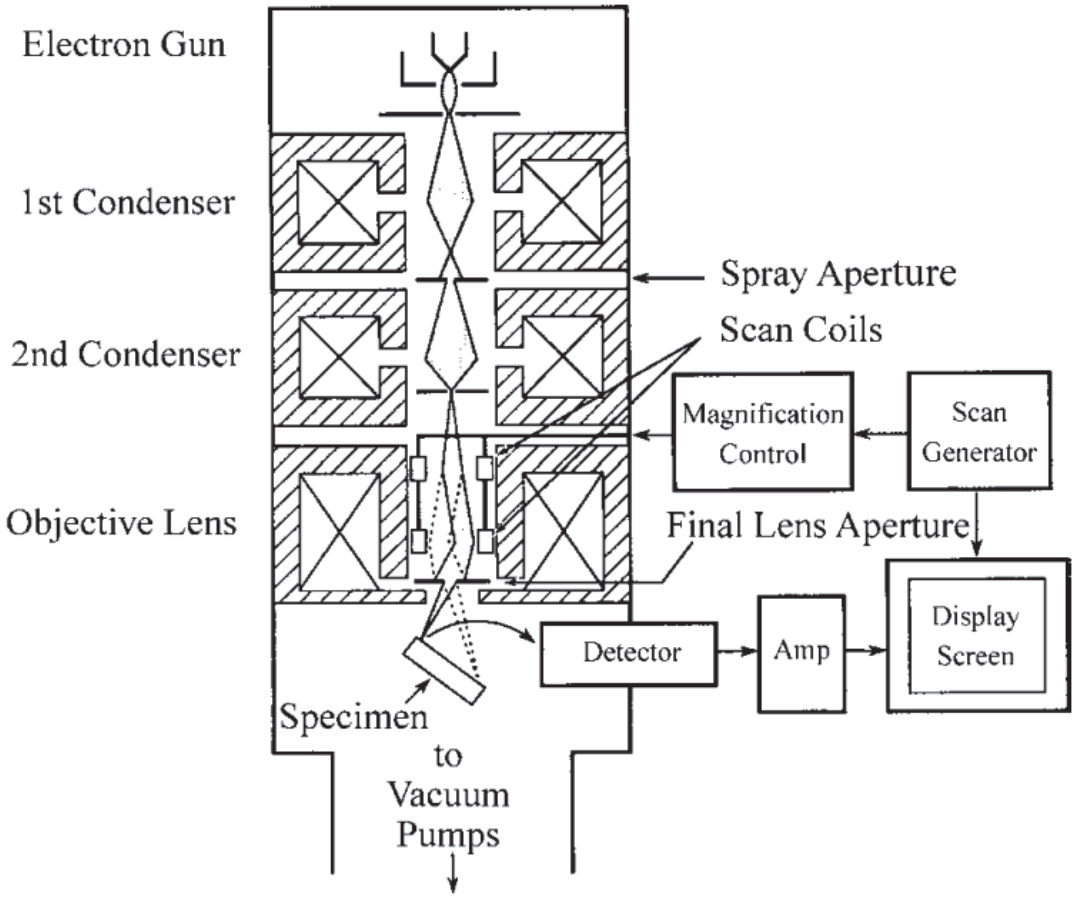

Figure 3-12: Schematic drawing of an SEM[31]

The schematic workup of an SEM is shown in Figure 3-12. The first component of the SEM is the electron gun, shown at the top of Figure 3-12. The electron beam is emitted from this gun downward through a series of lenses. The first two lenses are the condenser lenses, which reduce the crossover diameter of the beam. Next the electron beam passes through the objective lens, which focuses the beam down to a nanometer sized point, or probe, at the sample surface. The beam interacts with the specimen and produces secondary and backscattered electrons which are detected by the electron detectors. There may also be an X-ray detector if an EDS is integrated into the SEM. These electron and

X-ray signals are sent into a computer which is able to display the respective images and spectrums.

3.2.2 Optical Microscopy (OM)

Optical microscopy, or light microscopy, is a basic tool for examining the microstructure of materials. At its most basic, light microscopy is simply optics. Light microscopes use the principles of image formation, resolution, and magnification to produce images at desired amounts of magnification. These principles are achieved by utilizing two lenses, the objective lens and the projector lens. The way these lenses interact is shown in Figure 3-13.

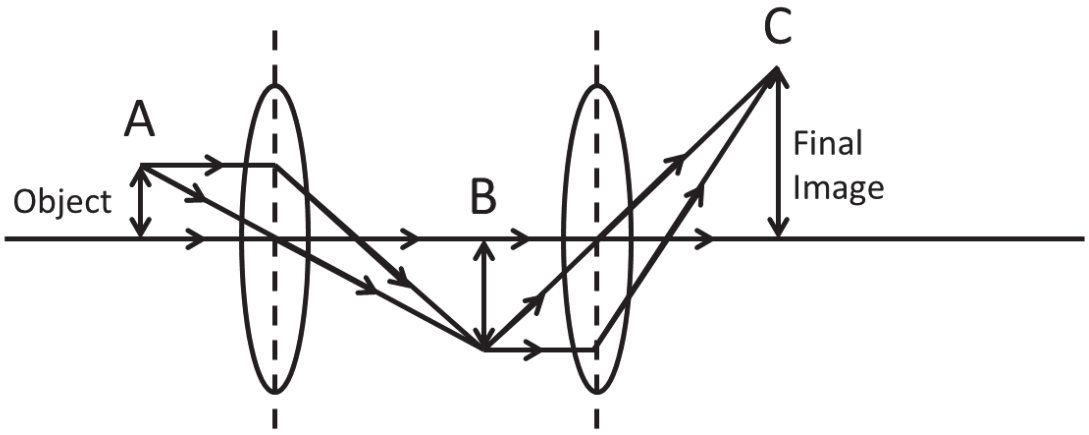

Figure 3-13: Diagram showing image formation using an objective lens and a projector lens[31].

The object to be magnified is shown at point A, and the light rays coming from the object pass through the objective lens which causes them to converge and focus at point B. This forms an inverted image at point B which then passes through the projector lens,

converging the light again to focus at point C, where the image is larger than the original object. The magnification of a singular lens can be calculated by the equation

$$M = \frac{v - f}{f} \tag{3.2}$$

where f is the focal length and *v* is the distance between the image and lens. This equation is for one lens; when finding the magnification of a microscope which has an objective lens and a projector lens, the magnifications are multiplied as can be shown in the following equation.

$$M = M_1 M_2 = \frac{(v_1 - f_1)(v_2 - f_2)}{f_1 f_2} \tag{3.3}$$

Another important principle of light microscopy is resolution. Resolution is based off of the minimum distance that two points can be individually distinguished. When a point is magnified by a lens, the magnified point is called an airy disk, symbolized as d, and is surrounded by diffracted rings. Basing this on the definition of resolution from above, resolution can be further defined as the minimum distance between the airy disks. Resolution can be calculated by

$$R = \frac{d}{2} \tag{3.4}$$

where R is the symbol for resolution[31]. The resolving power of an objective lens is determined by what is known as numerical aperture, where a better resolution is found with a higher numerical aperture. Numerical aperture is a measure of a microscopes ability to resolve an image of a specimen at a specified distance. Numerical aperture is related to the refractive index (n) of the medium between the specimen and the objective lens, and the angle of half the angular aperture. This angle (α) is shown in Figure 3-14 A.

Resolution can also be calculated by using the numerical aperture and the wavelength of the light (λ),

$$R = \frac{0.61\lambda}{n \sin \alpha} \tag{3.5}$$

where the denominator, *n*sin(α)*, is the equation for numerical aperture[34].

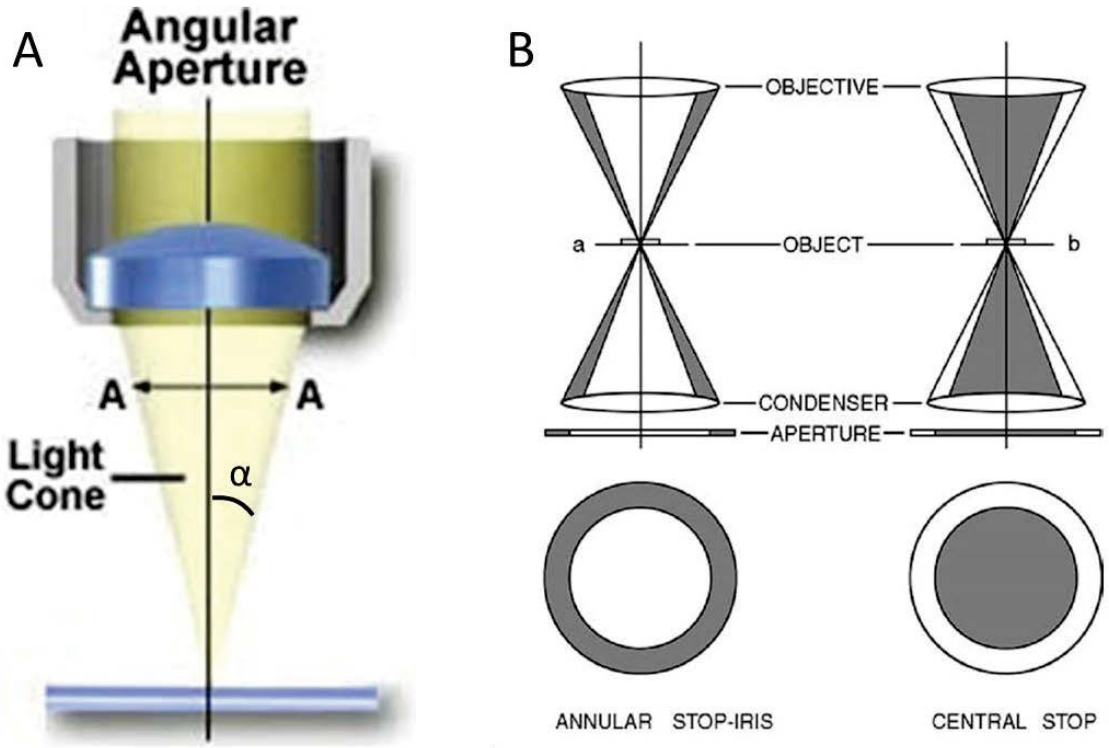

Figure 3-14: (A) Diagram showing the angle, α, of half the angular aperture, A[34]. (B) Diagram of bright field illumination (left) and darkfield illumination (right). Shaded regions indicate where light is blocked[31].

The differences in light wave properties which are reflected from the specimens surface are how images are seen in the human eye. Of the light wave properties, including amplitude, wavelength, and phase difference, the human eye can only detect differences in amplitude and wavelength. By physically changing these properties, the image will

vary and they can be compared to determine certain properties about the specimen. The most popular contrasting method is bright field and dark field, shown in Figure 3-14 B. Bright field is the most commonly used mode for viewing samples and their microstructure. Bright field works very simply using the optics properties of lenses explained earlier. The sample is evenly illuminated by a white light source and this light is reflected back into the lens of the microscope; imaging and magnification is done as explained earlier. Dark field, on the other hand, has the specimen illuminated by oblique light rays created by blocking the central region of the area of illumination. This makes it so light rays are required to scatter from the specimen surface to reach the objective lens and create an image. Both bright field and dark field images should be analyzed together since certain features which are invisible in one mode may visible in the other.

3.2.3 Auger Electron Spectroscopy (AES)

Auger electron spectroscopy is primarily a means to analyze the surface composition of a sample. The sample is struck with a focused beam of electrons from an electron gun. The electrons penetrate the surface of the sample up to about a micrometer and either a photon or another electron from the outer shell of atom being struck is expelled. This expelled electron is known as an Auger electron. This process is shown in Figure 3-15.

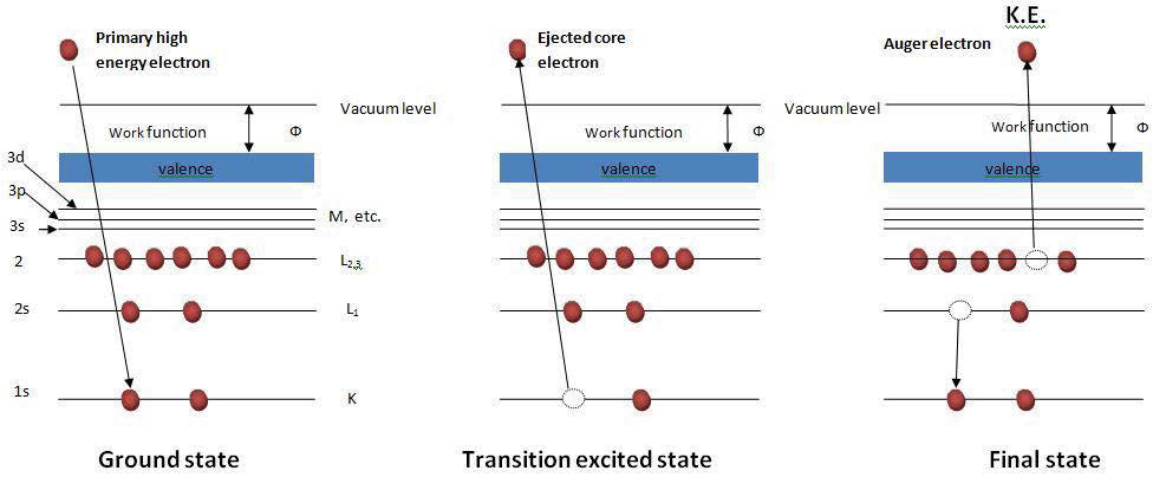

Figure 3-15: The process of Auger electron expulsion[35].

Since the electrons have varying energies, they can ionize a particle by penetrating at different electron levels. The Auger electron has a characteristic energy which reveals information about the atom from which the electron was expelled. This process can be used for elemental analysis. The Auger electron energies are measured and displayed on a varying background which is made of the measured inelastically scattered electrons. This spectrum is usually shown as differentiated because the background intensities are higher than they should be due to the inelastic scattering of the primary electrons and the

secondary electron emission at lower energies. This differentiation makes the peaks result in two peak amplitudes, one negative and one positive[36].

A diagram of the main components in the Auger electron spectrometer is shown below in Figure 3-16.

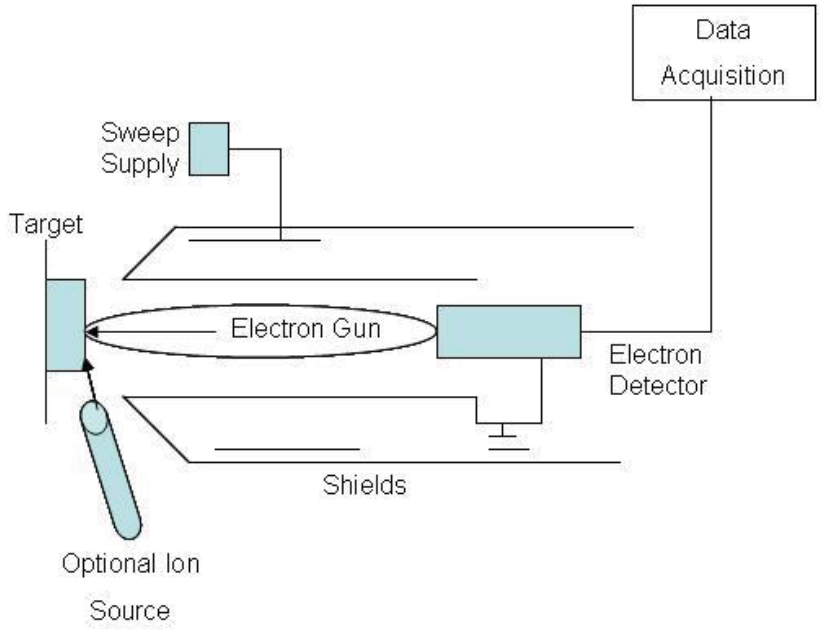

Figure 3-16: Schematic of the AES system[37].

The sample, labeled as Target in the diagram, is located in an ultra-high vacuum chamber between 10^{-8} and 10^{-10} torr. The electron gun is aimed at the specimen and fires an electron beam in that direction. The Auger electrons created from this are collected by the electron detector and the data is sent to a device for signal analysis. The ion gun, which also is aimed at the sample, is used to etch the specimen surface for use in depth profiling[31].

The electron gun is the source of the electron beam in Auger electron spectroscopy and is made with a filament of LaB_6 or tungsten which is surrounded by a Wehnelt cylinder. This filament is heated by a high voltage generator until electrons are emitted from the tip. Because the filament is a cathode, the electrons are drawn towards the nearest anode which is where they exit the gun and are shot toward the sample[38]. The diagram of the electron gun is shown below in Figure 3-17.

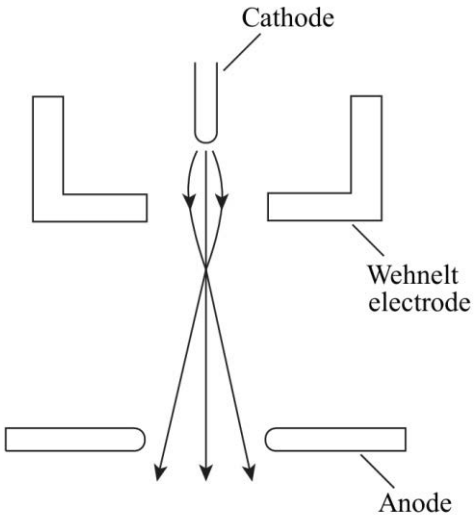

Figure 3-17: Schematic of the electron gun[31].

The ion gun in an Auger setup is primarily used for etching during depth profiling. The ion gun is made up of an ionization chamber, accelerating electrode, beam focusing lens, and deflection plates. The ionization chamber creates the ions and they are accelerated out through the flange, where they are focused by electrostatic lenses and are deflected out the end of the gun[36]. This process is shown in Figure 3-18.

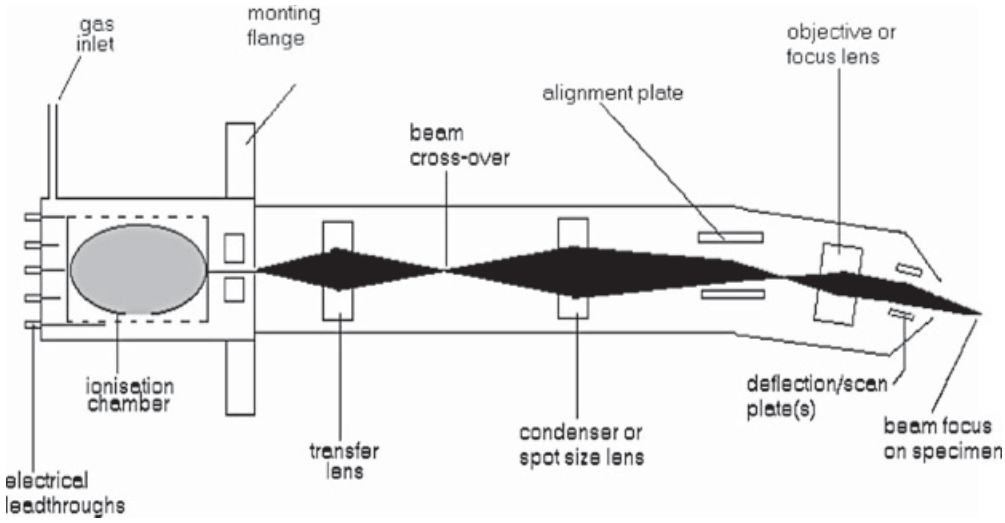

Figure 3-18: Diagram of an ion gun[36].

3.2.4 Focused Ion Beam (FIB)

A focused ion beam (FIB) is designed similarly to scanning electron microscopes (SEM), and while they may be found as a stand-alone unit, they are most commonly found working in tandem with SEM, Auger electron microscopy, and transmission electron microscopy (TEM). The FIB itself consists of various components, which include a vacuum system, ion column, stage, detector, liquid metal ion source, gas injection system, and -on certain models- a nanomanipulator.

The general way the FIB works is by creating ions on the order of 5 nm diameter by using a liquid metal ion source (LMIS). The most common metal used in the LMIS is gallium because of its low melting temperature, long source life, low vapor pressure, and its mechanical and electrical properties. For the ion source, the gallium is heated and it wets a tungsten needle, which then has an electric field applied to it. This process extracts gallium off the needle and ionizes it, creating a steady beam. These gallium ions are then

accelerated down an ion column where the beam is focused by condenser and objective lenses before reaching the sample surface[39].

The FIB has various purposes, such as imaging, deposition and etching. These are achieved by ion-solid interactions when the ions come into contact with the sample. When an ion contacts a sample it loses kinetic energy to the atoms in the sample. This energy transfer results in various reactions, such as ion backscattering, ion emission, and electron emission. Once the ions energy has been spent, it usually is implanted in the sample. These reactions in the sample cause sputtering from the materials surface. Also aiding in this material removal process is the collision cascade, which occurs if sufficient momentum is transferred to the materials surface, and it can cause an atom to be removed from its original site if the transitional energy that is transferred to the atom is greater than the displacement energy holding the atom in place. These phenomenons cause the FIB to mill away material from a sample[40]. The FIB can also be used to deposit specific metals and insulators onto the sample surface. This is done by injecting gas where the beam interacts with the sample. A controlled amount of tungsten (or some other metal) gas is introduced by a valve near where the beam interacts with the sample and the gas is deposited by chemical vapor deposition. The gas is adsorbed at the materials surface but it decomposes only where the beam hits. This decomposition process results in a buildup of the material at the interaction area.

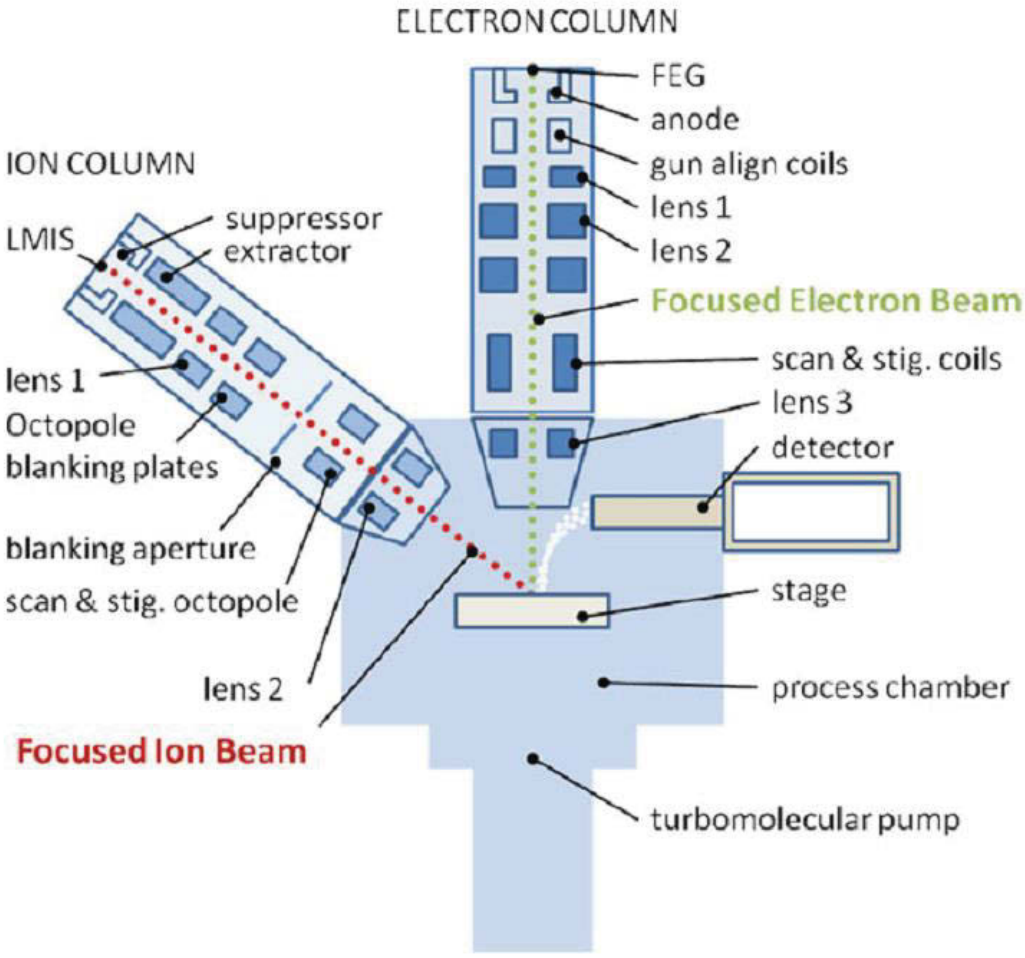

Figure 3-19: Diagram of a dual beam system, which includes a FIB as well as an SEM. The components for both columns are labeled[41].

Imaging is done the same as in SEM, but instead of using only electrons to form an image, secondary ions can also be collected with an appropriate detector. Although this is possible, simple observations are preferably done by SEM since FIB imaging might damage the sample. Using the processes of milling and deposition, it is possible to make electron transparent TEM samples using the FIB. This process is called FIB lift-out method. It works by using the FIB to etch into a material around one section to preserve a thin piece of material. This thin piece of material is then attached to a transfer fixture,

usually a nanomanipulator, and the final edge is etched away so the nanomanipulator can move the thin sample to a TEM grid inside the chamber. This version of the FIB lift-out method allows the sample to be further milled on the grid to thin the sample and also remove possible artifacts[39].

3.2.5 Transmission Electron Microscopy (TEM)

Transmission electron microscopy is an electron microscopy technique where a beam of electrons is passed through an electron transparent sample and the way the beam interacts with the specimen is analyzed. This interaction can be used to image the sample at high magnifications with high resolution as well as determining compositional and crystallographic information about the sample.

TEM works similarly to the SEM, but the instrumentation is more complicated. Like the SEM, there is an electron source which emits a beam of electrons and focuses the beam with various electromagnetic lenses. Since the data recording in a TEM is done at the bottom of the column, and the sample stage is located near the middle, there are lenses both above and below the sample stage. The lenses above the sample are two condenser lenses which focus the beam on the specimen. Below the sample are an objective lens, an intermediate lens and a projector lens, as well as apertures. Two apertures are located between the objective lens and the intermediate lens: the selected area diffraction (SAD) aperture and the objective lens aperture. Depending on which one of these apertures are inserted and which one is retracted, the viewing mode will change. If the SAD aperture is inserted and the objective aperture is removed, a select area diffraction pattern (SADP)

can be observed, and when the objective aperture is inserted and the SAD aperture is removed, an image of the specimen is observed.

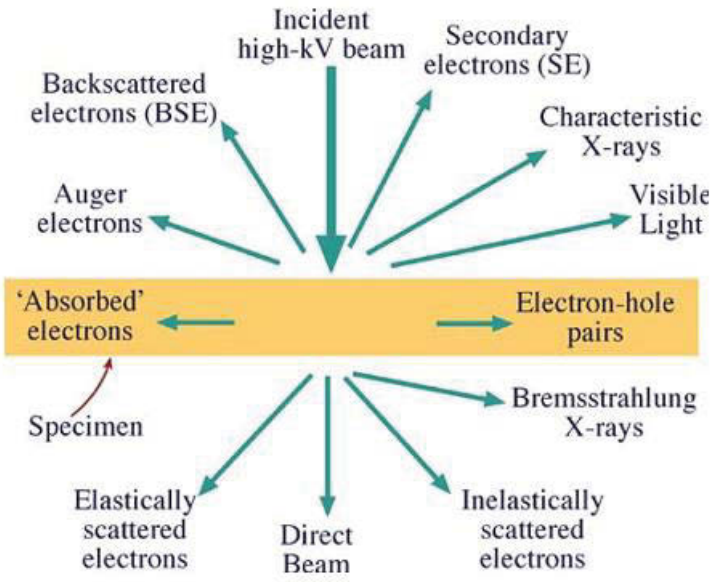

Figure 3-20: Signals generated from the sample as the result of electron beam/matter interaction[42].

In the TEM, the electron beam passes through the sample because it is thin enough to be electron transparent, and as it passes through, it produces many secondary signals such as secondary electrons, backscattered electrons, elastically scattered electrons, inelastically scattered electrons, among others, as shown in Figure 3-20[42]. In the TEM, the contrast in the image is done by the number of electrons that are scattered away from the incident beam. This electron deflection is from the interaction of the electrons and the atomic nuclei of the material in the sample. How much the electron deflects depends on the mass-density of the sample at that point. The objective aperture, used for image creation, will only allow the transmitted beam to pass through the aperture which cuts out the strongly scattered beams and creates an image on the screen below. In this image, the

darker areas are where the beam was more scattered and the brighter areas are where the beam was less scattered. This creates the contrast that forms an image of the sample.

The TEM can also be used in a diffraction mode which will create a SADP. This is done in crystalline samples where Bragg's Law is satisfied similar to the diffraction of X-rays in X-ray diffraction. A main difference between X-ray diffraction and the electron diffraction in a TEM is the diffraction angle is very small since the lattice planes are nearly parallel with the electron beam. This simplifies Bragg's Law and creates the equation:

$$\lambda L = Rd \tag{3.6}$$

Where d is the distance between the lattice planes, λ is the wavelength of the beam, R is the distance between the central point of the beam and a diffraction spot, and L is the distance between the sample and the photographic plate, which is known as the camera length. It is important to note that the camera length is not a physically measureable distance in the TEM since the lenses change the geometry of the path. Using the SAD aperture in diffraction mode, these principles create constructive diffraction from the lattice planes which form spots of high intensity on the screen. These spots are reciprocal lattice points on a reciprocal lattice plane of the crystal in the selected area. There are methods and techniques for indexing these diffraction patterns to give information about the crystal structure of the sample material[31].

CHAPTER 4: RESULTS

This chapter will detail the results of each of the projects mentioned in the experimental section. This chapter initially presents the results of the ultrasonically welded aluminum cables, followed by the results of the impact modified polymers side project. Each section will be broken down into subsections detailing the results for the parts of the respective projects. The aluminum cable section will be displaced into subchapters for the analysis on the cable alone, the insulation, and the ultrasonic weld. The impact modified polymer subsections will detail the measurement of fiber length and analysis of the polymeric domains.

4.1 Aluminum Cables and Ultrasonically Welded Terminals

4.1.1 Aluminum Cables

Initially, the six aluminum cables, which had been giving varying results when welded, were analyzed. The goal of this analysis was to determine the differences between the cables which would help isolate which properties were responsible for the poor welds. This was done by analyzing the surface of the wires in the bundle by SEM and the grain texture of the wires by XRD.

Analyzing the wires by XRD would show whether the grains in the aluminum were elongated by the drawing process. If the wires were annealed after the drawing process, the grains would be reset to normal sizes and shapes. Annealing is a common heat

treatment when drawing metal wires. The texture investigation was important to verify that all of the six manufacturers were annealing their product as a final step in their manufacturing process.

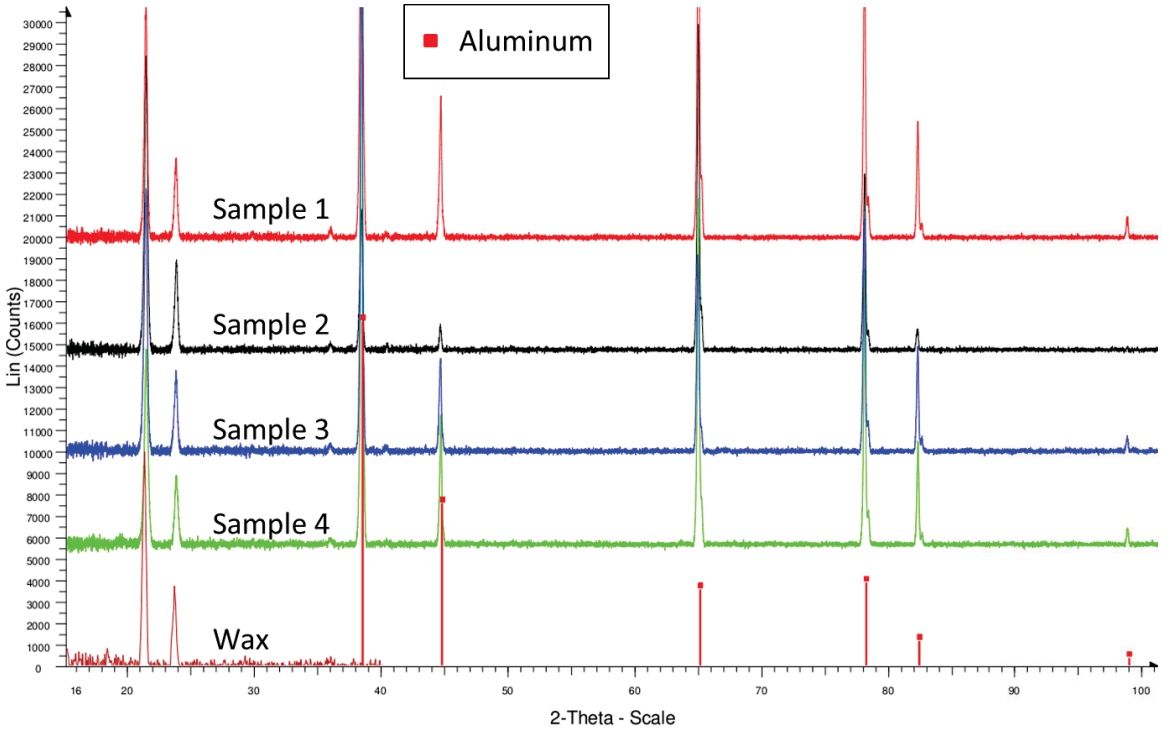

Figure 4-1: XRD analysis of the wires taken from 4 of the 6 cable samples. The spectrum from the wires was offset from the x axis to show the wax spectrum below it, which overlapped completely.

Figure 4-1 shows of the XRD results obtained from four samples and the wax used to hold the samples in the sample holder. The XRD spectra of all four samples show only one metal peak, corresponding to aluminum. The low 2-theta peaks are collected from the wax, as indicated by the wax spectrum. The peaks for all samples are quite narrow which indicate the quasi-uniform size and shape of the crystalline grains within all investigated samples. Therefore, it can be concluded that there are no crystalline texture differences among the samples. It seems that all samples have been annealed at the end of the

drawing process, as expected. The spectrum peaks would be much more broad from the elongated grains if the wires were not annealed, the closer the material is heated to the specific annealing temperature, the narrower the peaks will appear[43].

In the SEM analysis of the wires surface, it was found that three distinct defects were present: scratches and cracks, inclusions, and contamination and oxidation. The scratches were observed to be in two styles; one being small surface scratches, like what is shown in Figure 4-2 A, and the other being very long deeper scratches following the length of the wire. The long scratches are probably a result from the wires dragging along each other during the bundling process. The smaller scratches could be from a number of sources, including dirt getting into the wire bundle and rubbing against the aluminum wires as the cable gets flexed. Smaller striations, appearing like cracks, are evident, as shown in Figure 4-2 B, which are likely due to the drawing process. The striations were observed on all six samples to varying degrees, but there was not a sample that had significantly more or less than the others.

There were many inclusions embedded in the surface of the wires as well. Some of these inclusions were larger, Figure 4-2 C, but most of them were smaller and scattered through the surface, Figure 4-2 D. These embedded particles were analyzed by EDS to determine their composition, Figure 4-3 B. All the particles contained various metals, with iron (Fe) being easily the most common, but other metals like brass were found as well. In the EDS analyzed area, some of the Fe particles showed higher oxygen (O) peaks which would suggest that the particle was iron oxide, or rust. These larger metal particles were most likely from the drawing process when the wire is pulled through the die, which is commonly made of steel. It is certainly possible that very small pieces of the die break

off during drawing and get lodged in the surface of the material being drawn. This is also evidenced by the groove in the aluminum leading up to the larger particles, very much like in Figure 4-2 C. Much like the striations, the embedded particles were present in all samples and there was not a particular sample which clearly had more than the others. These particles probably have little effect on the weld quality since they comprise very little of the surface of the wires.

The last surface observation was of contamination. Some samples had localized contamination on the wire surface, such as shown in Figure 4-2 E. These spots of contamination were all primarily carbon based, but some had smaller quantities of other elements. An example of this is shown in Figure 4-3 A, where the highest weight percentage in the contamination is carbon (the aluminum is ignored since the wire material will always be recorded due to how the EDS gathers its data) and some other elements are present, such as a moderately high amount of chlorine (Cl). For the carbon contamination, sample 6 appeared to have more overall than the others, but without analyzing a large number of wires from the bundle, the sample size is not adequate to definitively state which are more contaminated. Oxidation is also present, and is shown as a slightly darker grey than the aluminum in backscattered images, and can also be identified by cracking, as can be seen in Figure 4-2 F. The oxidation appeared to be less abundant on the wire surface than the carbon based contaminants, but this is not indicative of less oxidation than contamination, rather that it is more difficult to distinguish on the wire surface. Since the contamination and oxidation was the most varying of the defects found between the different cables, further analysis of the contaminants was investigated by AES.

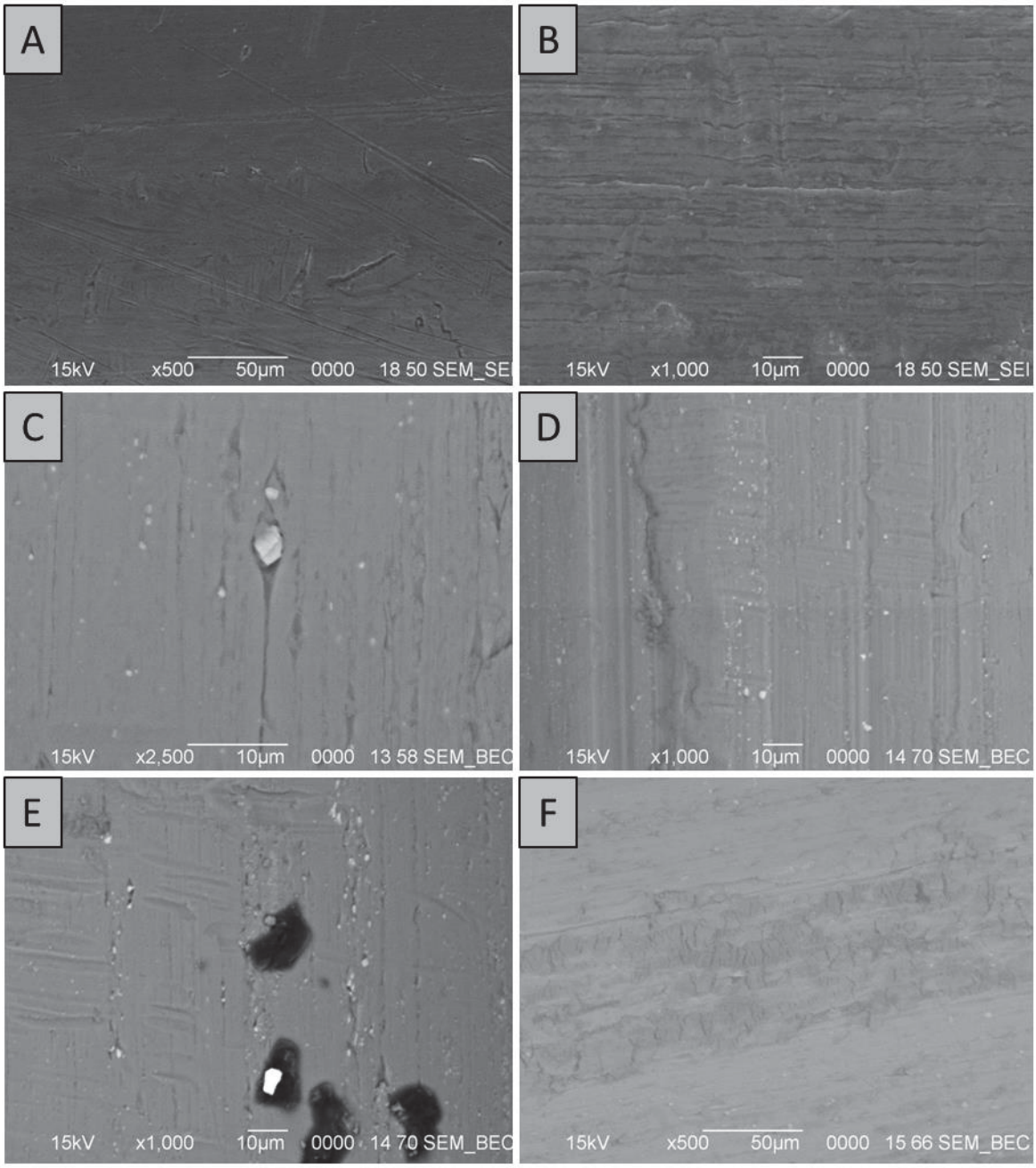

Figure 4-2: (A) Secondary electron image of randomly oriented small scratches on the wire surface on sample 4. (B) Secondary electron image of oriented scratches on the wire surface on sample 5. (C) Backscattered electron image of an example of a large inclusion embedded in the wire surface on sample 2. (D) Backscattered electron image of an example of small inclusions (whiter spots) embedded in the wire surface on sample 6. (E) Backscattered electron image of an example of contamination on the wire surface on sample 6. (F) Backscattered electron image of an example of oxidation on the wire surface on sample 5.

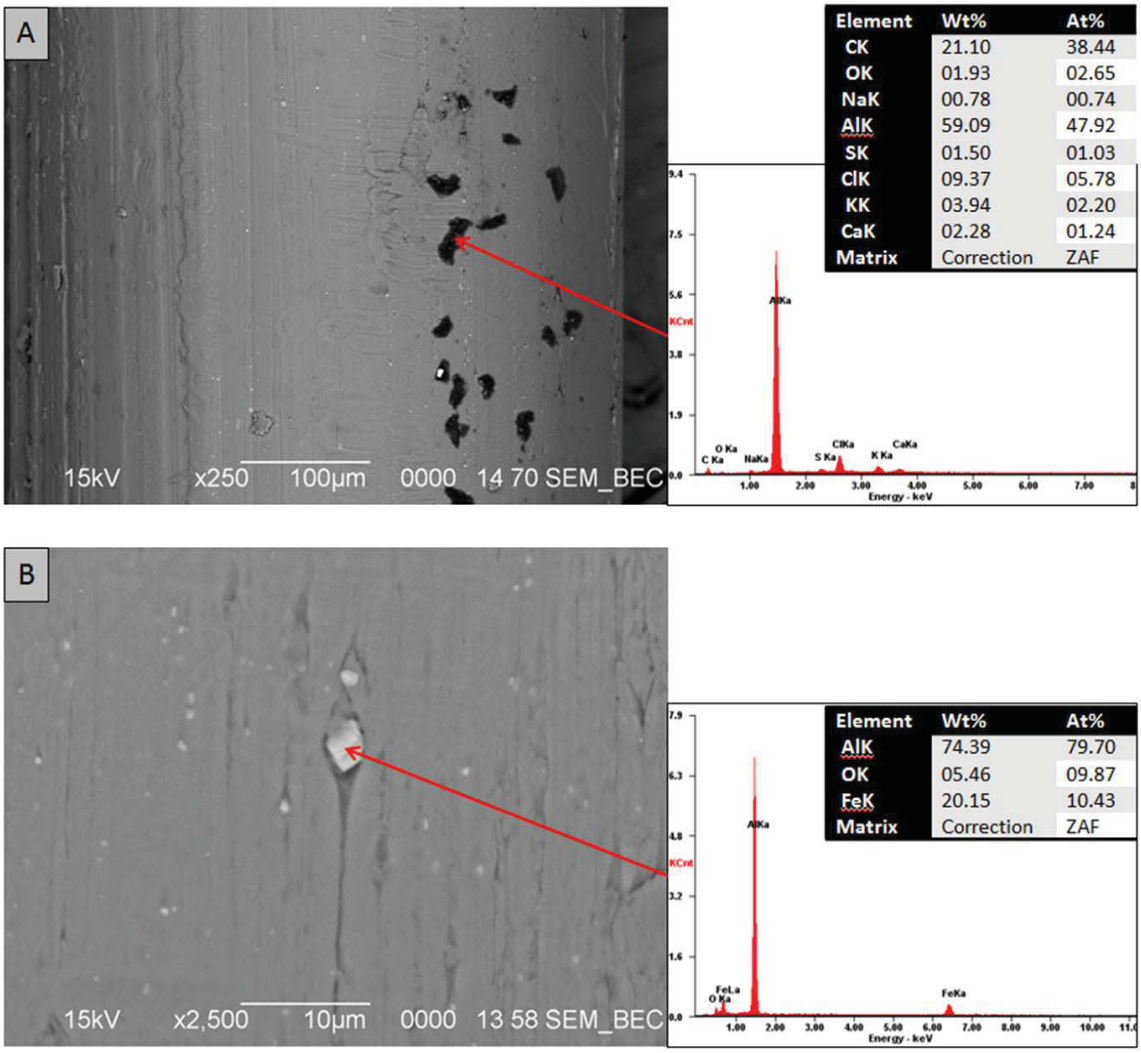

Figure 4-3: EDS analysis of (A) surface contamination on sample 6, and (B) embedded inclusion in sample 2.

AES was used to get a detailed look at the composition of the wire samples' surfaces. Depth profiles were taken with focus on how carbon, oxygen, and aluminum vary through the first 50-100nm of the sample surface. These depth profiles were then broken up to compare the amounts of carbon and oxygen between the samples to see if any had an unusual amounts of contamination or oxidation, and these results are shown in Figure 4-4. It should be noted that sample 4 and 6 are absent from the depth profile comparison;

this is due to incorrect data collected for those two samples, so they are unfortunately omitted from the AES analysis. It can be seen in Figure 4-4 A that sample 2 begins with significantly more carbon than the other samples, but because the plot for sample 2 drops off much more quickly, this means that the carbon layer at the analyzed point was thin and covered a large area. Conversely, sample 3 starts off with a moderate amount of carbon but takes longer to mill away than the other samples, indicating that the carbon layer on this sample was slightly thicker than the rest.

Figure 4-4 B shows the same type of comparison, but looking at oxygen concentration rather than carbon. All of the samples in this figure start off low because the analyzed surface is still covered in carbon, but as the carbon gets milled away, the oxide layer underneath begins to be measured. Then the oxygen measurements decrease, indicating that the oxide layer has been milled away leaving only aluminum metal to be measured. The width of this oxygen peak gives a rough approximation as to how thick the oxide layer is at the analyzed point. It can be seen in the comparison that sample 2 had a very thin oxide layer compared to the other samples. Sample 5 had a much thicker oxide layer than the other samples, since it can be seen that it does not decrease much within the scope of this graph. This very broad peak of oxygen in sample 5 may not be indicative of the oxide layer, since there is a possibility that the analyzed point had a clump of oxide present, and that clump took a longer time to etch through.

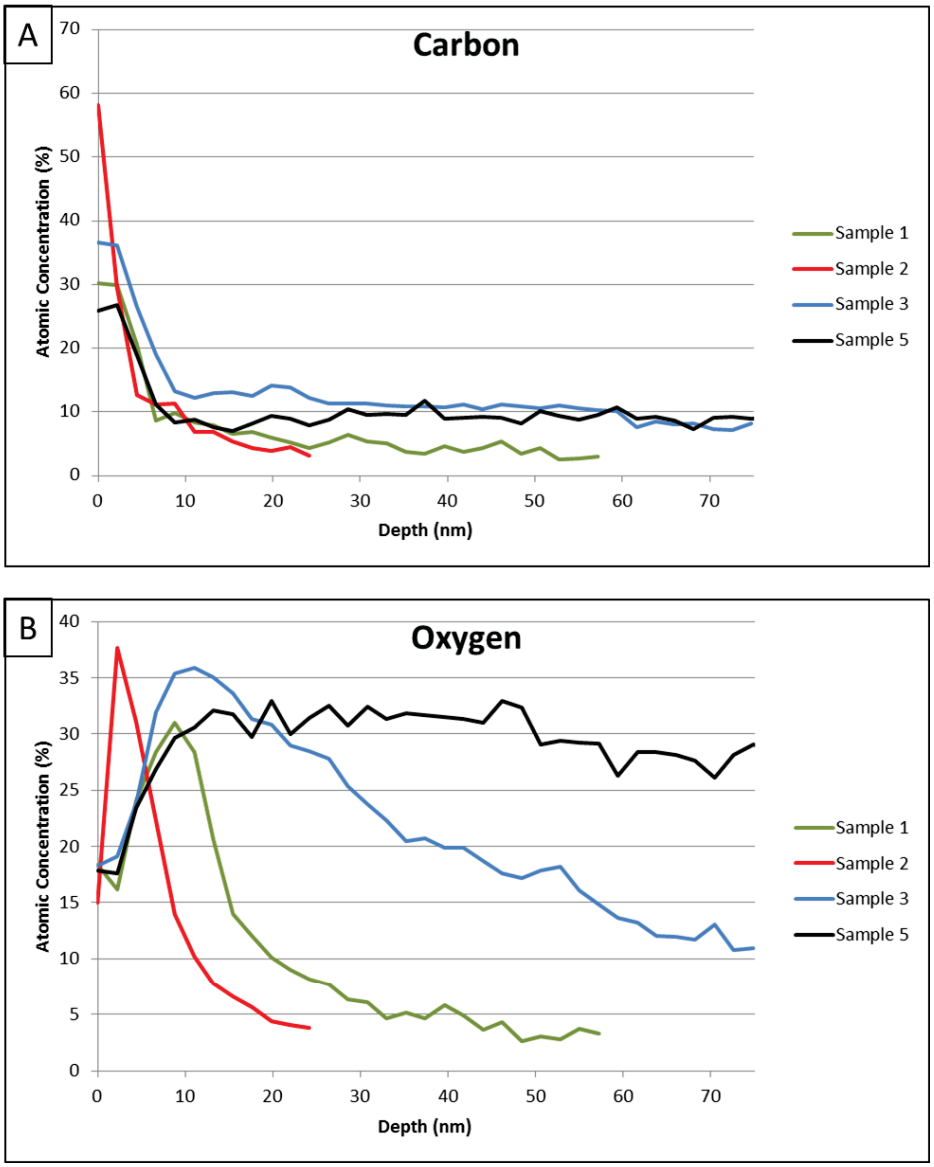

Figure 4-4: AES depth profile results of 4 of the 6 cables. (A) Graph of carbon concentration as a function of depth into sample surface, (B) Graph of oxygen concentration as a function of depth into sample surface.

Other than the possible thick oxide layer in sample 5, none of the amounts of carbon or oxygen were large enough to be significant. Especially since most literature on ultrasonic welding claims that films and oxide layers are dispersed during the welding and therefore do not affect the weld. Due to this claim, it is not likely that the variation in success of welds is a result of the wire surface contaminants.

The next samples to be analyzed were the red and pink ultrasonically welded terminals where one set of weld samples were considered successful (red sample) and the other was considered unsuccessful (pink sample). Before looking at the weld interface, the cables leading to the weld were analyzed by SEM and EDS for the differences between the pink and red wires, same as the previous six cables. Four wires were taken from both the red and pink wire bundles. Since it was determined from analyzing the six cables that the most likely important factors for the weld quality was the carbon contamination and the oxidation layer, these were what the SEM and EDS analysis of the pink and red wires focused on.

The wires from the red cable were all similar, with some scratches, inclusions, and contaminations, as had been seen before when analyzing the six manufacturers' cables. Three of the four wires from the pink cable showed nearly the same, with slightly more surface contamination than the red cable. One of the four wires taken from the pink cable was significantly rougher than any of the other analyzed wires, as shown in Figure 4-5 A and B. The entire surface area of this inch long sample had this rough surface texture. Viewing the wire with the backscattered electron detector, the wire showed darker areas down in the numerous crevices, which were analyzed by EDS (shown in Figure 4-5 C) to show a composition very close to the one shown in Figure 4-3, but with a much lower measurement of aluminum and an absence of chlorine. This low count of aluminum suggests that this contamination layer is thicker than the contamination spots seen on the previous cables. This makes sense since the contamination, likely to be lubricant from drawing, would deposit in the low spots of the jagged wire and be less likely to be worn off throughout the rest of the wire processing. The presence of this very rough and dirty

wire suggests that surface texture and contamination on the wires which are bundled together to make up the cable, could have a negative impact on the quality of the ultrasonic weld.

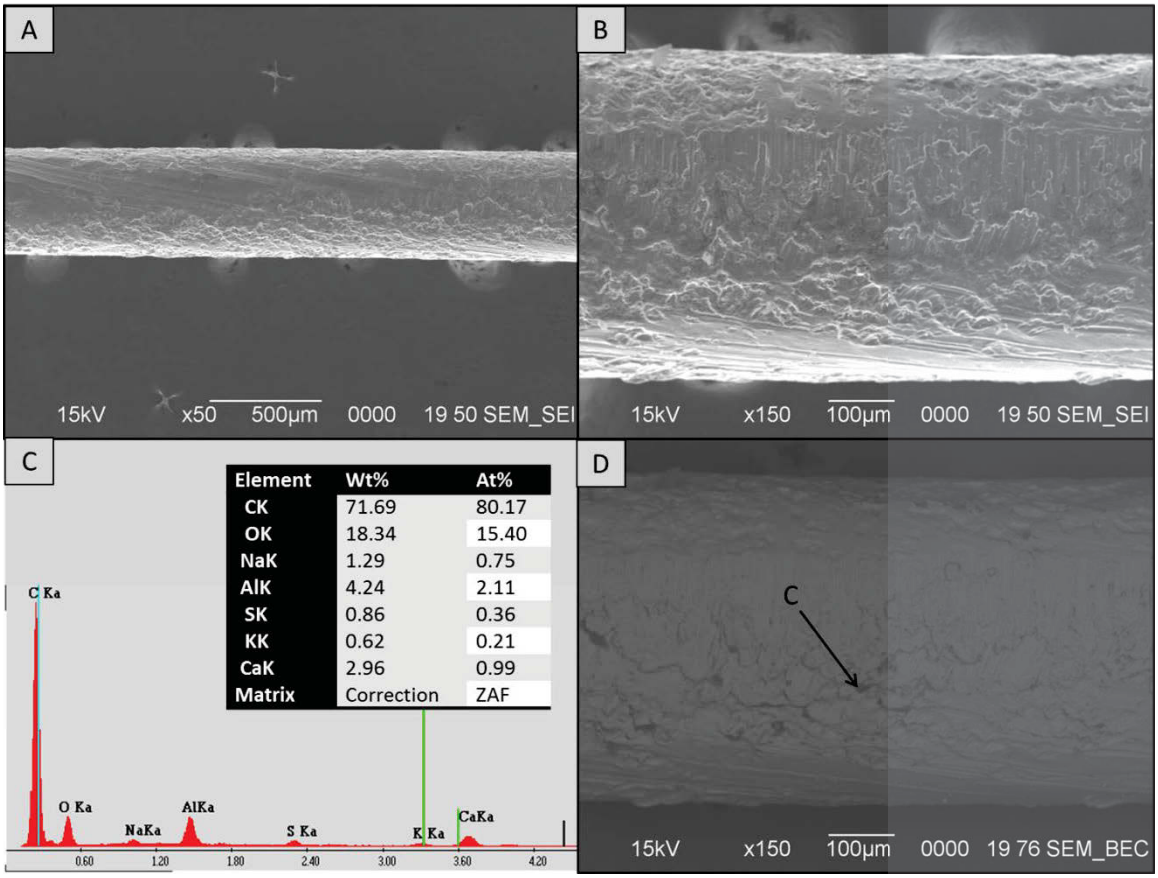

Figure 4-5: One wire from the pink cable bundle. (A) Secondary electron image showing the rough surface texture of the carbon covered wire. (B) Secondary electron image at a higher magnification. (C) EDS spectrum and quantification of the spot labeled 'C' in D, showing the majority of this area as carbon. (D) Backscattered electron image of the same area as in B.

After identifying this rough wire in the pink bundle, it was desired to observe the cable further and determine if both red and pink samples had more wires with this texture. To determine this, for both red and pink samples, the end of the whole cable was viewed with a low magnification stereo microscope. It can be seen by comparing Figure 4-6 A

and B that all of the wires of the red cable that are in focus are quite smooth and shiny, while the majority of the wires of the pink cable appear rough and dull.

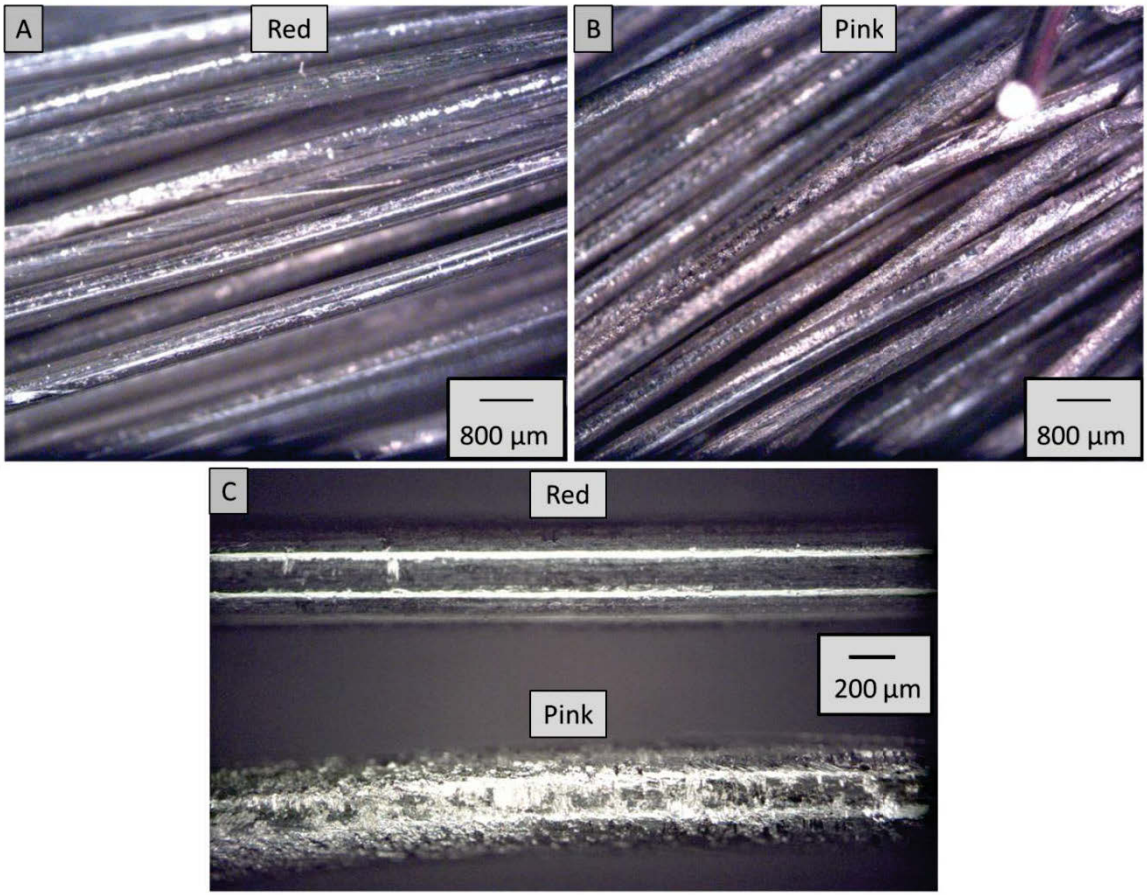

Figure 4-6: (A) Optical microscope image of the red sample wire bundle, where the wires appear quite smooth overall. (B) Optical microscope image of the pink sample wire bundle, where a majority of the wires appear rough. (C) Optical microscope image comparing one wire from each sample, red and pink.

Each wire in the bundle was observed individually and was judged to be rough or smooth. It was determined by judging each wire in the bundle that 86% of the wires in the pink cable had a significantly rough surface. This suggests that the surface quality of the wires in the pink cable is very poor, overall, in comparison to the wires in the red cable. Comparing one randomly selected wire from each cable, as shown in Figure 4-6 C,

the comparison between the two samples is obvious, with the red wire having only minor abrasions and the pink wire being completely coarse.

4.1.2 Cable Insulation

TGA was performed on the cable insulation to rule out the possibility that the pink and red polymer insulation were of different composition, which may affect the weld in some way. Three samples of both pink and red insulations were made for TGA analysis to give a small average of the results. The six samples were analyzed in the TGA and the results are shown in Figure 4-7.

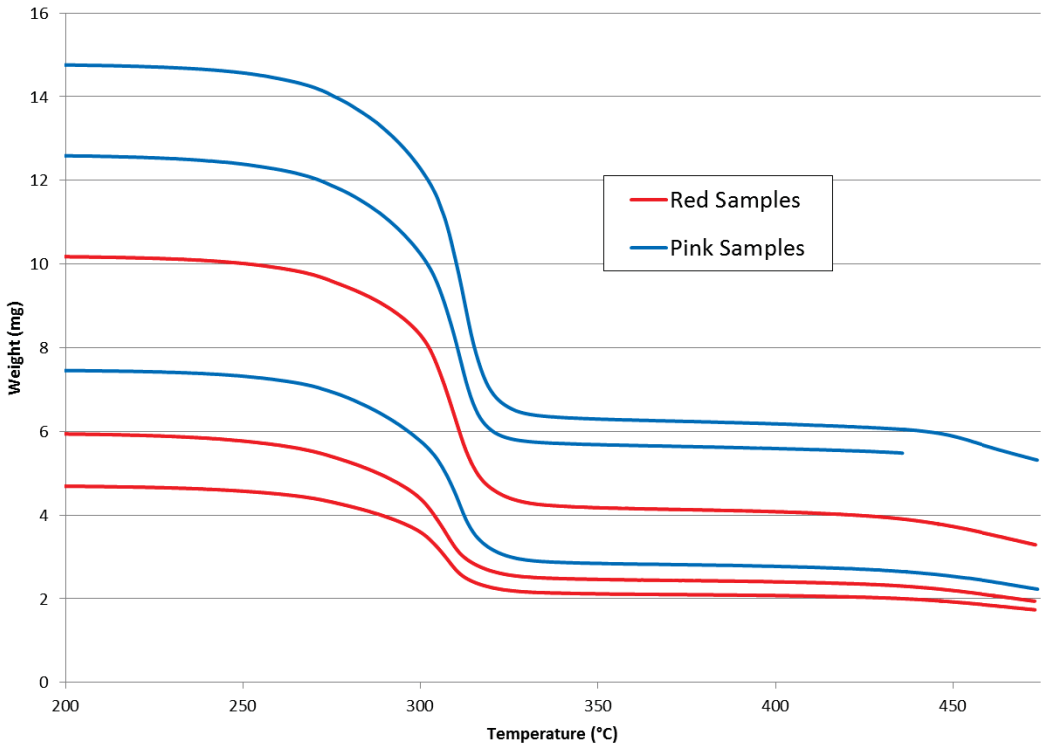

Figure 4-7: TGA results of the pink and red samples' insulation. Three samples of each were performed, where blue is the pink insulation samples and red is the red insulation samples.

The different weights of the samples were not important since this doesn't affect the temperature at which the decomposition takes place. The results show that all six samples decompose through the same temperature range, which indicates that there are no compositional differences between the red and pink samples' insulation. If they were different in chemical composition, one set of either pink or red would have had its decomposition take place at a different temperature than the other, or it may have had another secondary decomposition which the other did not have. Since this was not the case, it was determined that the two samples' cable insulation were compositionally the same, so the insulation should not have any effect on the quality of the ultrasonic weld.

4.1.3 Ultrasonically Welded Terminals

The first step of sample preparation for the weld analysis was by embedding in epoxy. These samples were cut to expose two directions of the interface, longitudinal and transverse (referred to as cross-sectional cut), as shown in Figure 3-6 A. Primarily, the investigation was to look at the interface and determine why the red sample was considered a better weld than the pink one, but it was also of interest to look at the weld from different directions and determine if there was any sensible difference in between them for a given sample.

The preliminary observation of the cut faces was performed by OM. By using the microscope on the brightfield view without filters, features in both samples were clearly identifiable. The first noticeable feature was that the thickness of the aluminum at the weld zone was different between the two samples. The aluminum in the red sample was approximately 400μm thicker than the aluminum in the pink sample, as can be clearly

seen by comparing the aluminum thickness between Figure 4-8 A and B. This thickness may vary from weld to weld, so this difference may not be indicative of all red and pink weld samples.

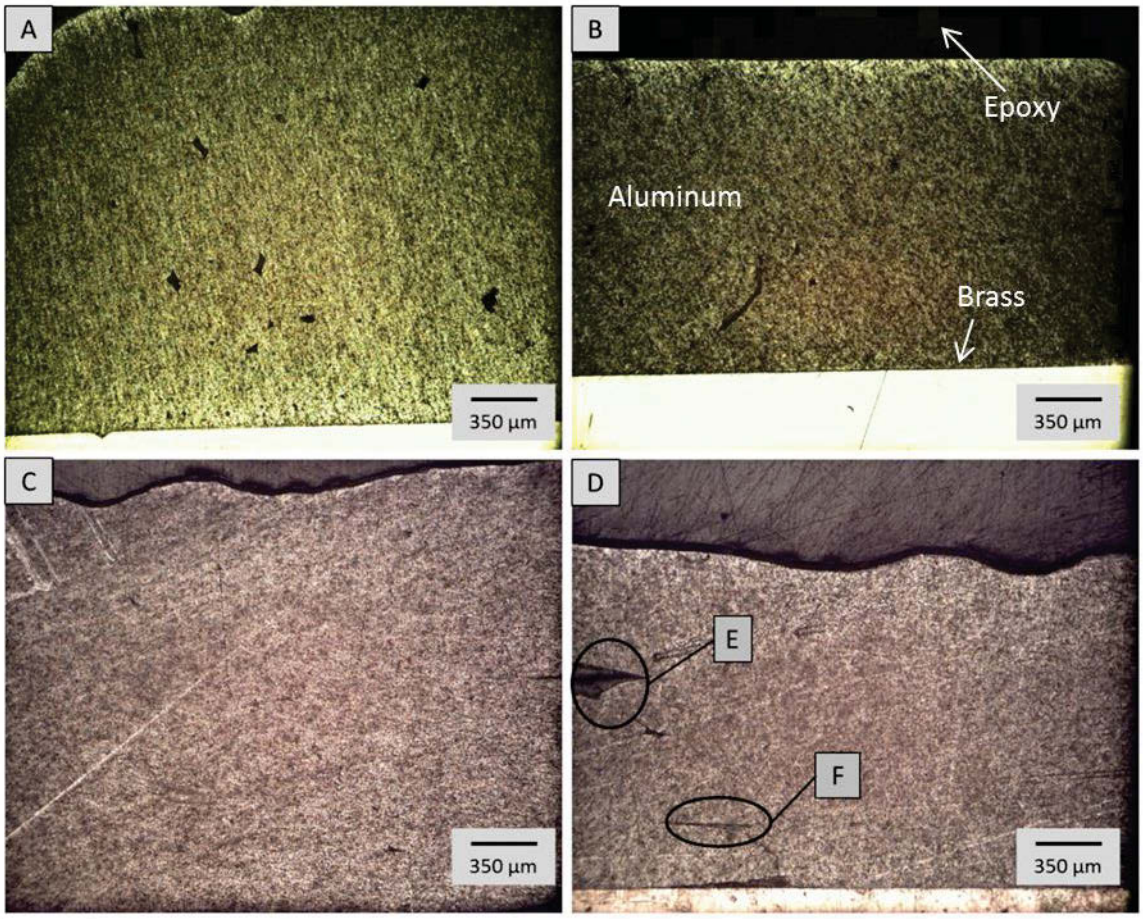

Figure 4-8: OM images of the gaps in the aluminum (upper, grey material) of the weld zone of the terminals. (A) Image of the cross-sectional cut face of the red sample. (B) Image of the cross-sectional cut face of the pink sample. (C) Image of the longitudinal cut face of the red sample. (D) Image of the longitudinal cut face of the pink sample. The large encircled gap (E) seems to be created by two separate wires coming into the weld zone, and the circled gap (F) is an example of one of the long slender voids in the aluminum.

Another notable feature was that the aluminum side of the interface had many voids. On the cross-sectional face, these appeared as odd shaped spots, shown in Figure 4-8 A and B, and on the longitudinal face they appeared as long slender openings, and example of

which is shown in Figure 4-8 D, labeled as F. The large gap labeled E in Figure 4-8 D is not an opening in the weld zone: this area is at the edge of the weld zone and the gap is simply where the unwelded wires come into the weld zone. The size and shape of the openings indicate that the aluminum wires were not completely welded into one solid. It seems that the majority of the aluminum had been welded together. However, for an unknown reason, several areas between individual wires were not bonded. This feature was seen in both pink and red samples. The red sample appeared to have slightly more openings than the pink sample on the cross-sectional cut face, but the pink sample had more on the longitudinal cut face. The visible gaps in the aluminum in the red sample were all located toward the edge of the weld zone, while the gaps in the pink sample were dispersed through the whole weld zone.

Looking at the weld interface between the aluminum wires and terminal, the differences between the samples were shown. The interface in the red sample was shown to be tight and without voids along both cut directions, suggesting that the two materials were successfully joined throughout the weld. There could still be areas in the interface which were not joined, but along the lines where the cuts were made into the weld, none were present. The pink sample, however, showed various gaps and cracks between the two materials. Small gaps was seen along a majority of the face, as is shown in Figure 4-9 B. This gap is noticeable due to the slightly darker, out of focus line in the aluminum following the interface and is comparable to the voidless Figure 4-9 A.

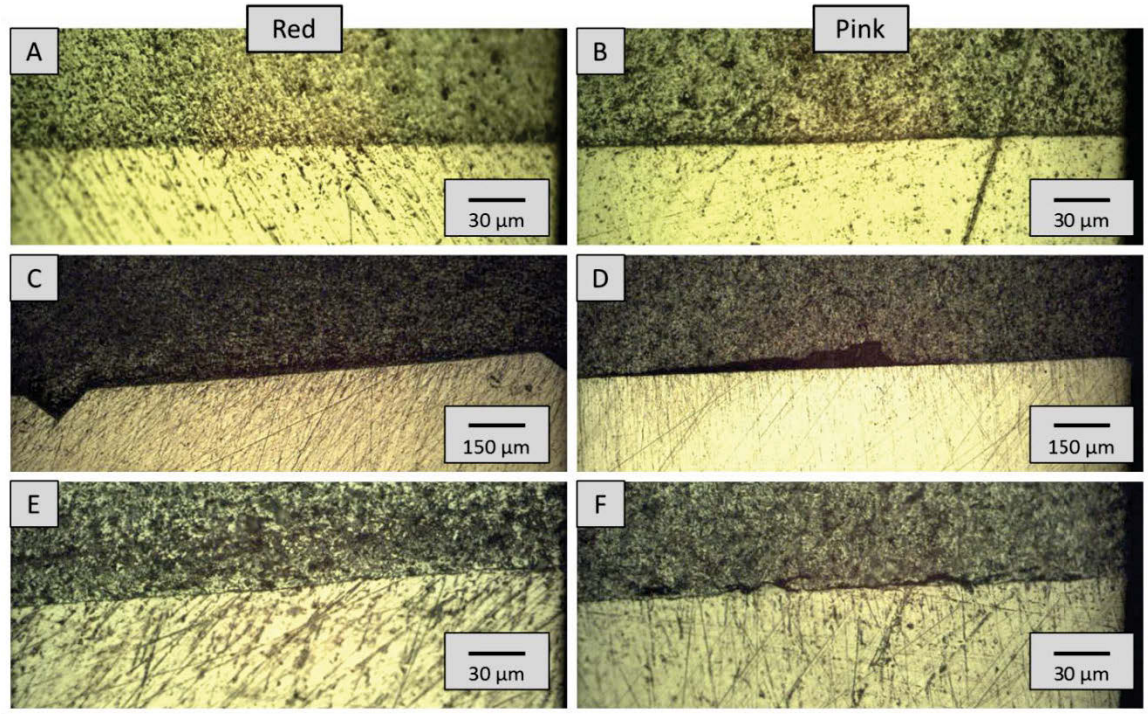

Figure 4-9: OM images of the weld interface of aluminum (grey upper material) and copper (golden lower material) showing the differences between the red sample (left images) and the pink sample (right images). (A) Red sample weld interface from the cross-sectional cut face showing a tight joining between materials. (B) Pink sample weld interface from the cross-sectional cut face showing a small gap between materials. (C) Red sample weld interface from the longitudinal cut face showing no gaps. (D) Pink sample weld interface from the longitudinal cut face showing a large open void in the aluminum along the interface. (E) Red sample interface from the longitudinal cut face showing no gapping. (F) Pink sample weld interface from the longitudinal cut face showing a crack like void between the two materials.

Looking at the longitudinal direction of the weld, which is the direction of the cable wires, there were many differences between the two samples. Once again, like the cross-sectional face, the interface between the two metals in the red sample appeared well bonded and lacked voids. The pink sample, on the other hand, had many defects, some being quite large. The largest defect was a void, shown in Figure 4-9 D, which was approximately 800µm in length and approximately 70µm high. This void was also so deep into the cut face that the light from the microscope could not illuminate much of the

voids depth. This larger area where no bonding occurred between the metals was located close to the edge of the weld zone where the cable was leading into the weld. Being close to the edge of the weld zone may have been a possible cause for this void to form; if the pressure applied to the horn of the welder was not evenly distributed, there could have been less pressure towards the outer edges of the weld zone which may have not been enough to bond the metals. However, this thought does not provide a difference between the red and pink samples since both samples were made on the same instrument with the same input parameters. The large void was not the only defect found along the weld interface on the pink sample. There were also numerous small voids along the interface. One such void, appearing like a crack, is shown in Figure 4-9 F. This void appears as though the metals at this point were lightly joined during the welding, but at some point after broke apart. The fact that this void has jagged edges and branches in some places indicates that the interface had actually fractured.

It is also important to note that the brass terminal plate had diamond shaped points pressed into its surface to give the aluminum more surface area to bond with. An example of one of these dents can be seen on the left side of the weld interface shown in Figure 4-9 C, and half of another one on the opposite side of the same figure. These dents were on the brass terminal plates for both the red and pink samples; whether they showed up in the images or not, depended on if the cut to expose the weld interface passed through a set of the dents. In both samples, the dents always appeared completely filled by the aluminum and the materials seemed bonded well. The only exception to this was near the weld edge were the cable came into the weld zone, but the partial filling in this area was present in both samples, so this was ruled out as a difference.

Further investigation of the weld interfaces was performed by SEM to gather images at higher magnification and to obtain some elemental composition results by EDS. The longitudinal cut face was examined since EDS analysis of the gaps and cracks in the pink sample's interface was desired. The longitudinal cut face of the red sample was analyzed as well to compare to the pink sample. The red sample had no notable gaps to analyze, so high magnification images of the interface of the metals were taken to compare to where the pink sample's interface was well bonded. In all SEM images, the aluminum is the material above the interface and the brass was the lower material. This comparison, shown in Figure 4-10 A and B, shows that the successfully welded sections are nearly identical between the samples, other than the interface of the pink sample being slightly more jagged than the interface in the red sample.

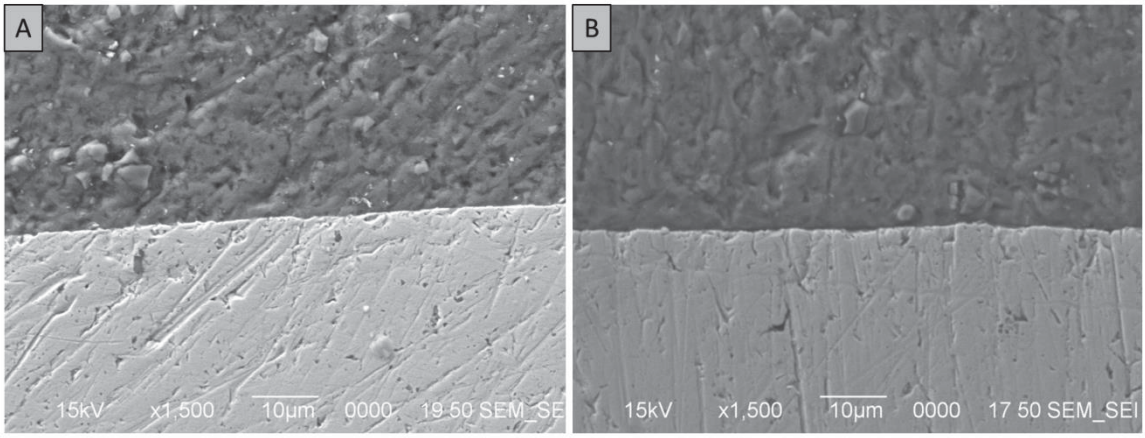

Figure 4-10: (A) SEM secondary electron image of the interface of metals in the red sample. (B) SEM secondary electron image of the interface of metals in the pink sample.

After comparing the successfully welded interfaces of the two samples, the voids and cracks of the pink sample were analyzed. The large void shown in Figure 4-9 D had epoxy filling most of the open space, so for SEM and EDS analysis was done on a corner

of the large void where it appeared to not have been filled with epoxy. This selected area is shown in Figure 4-11 along with the EDS results from inside the void.

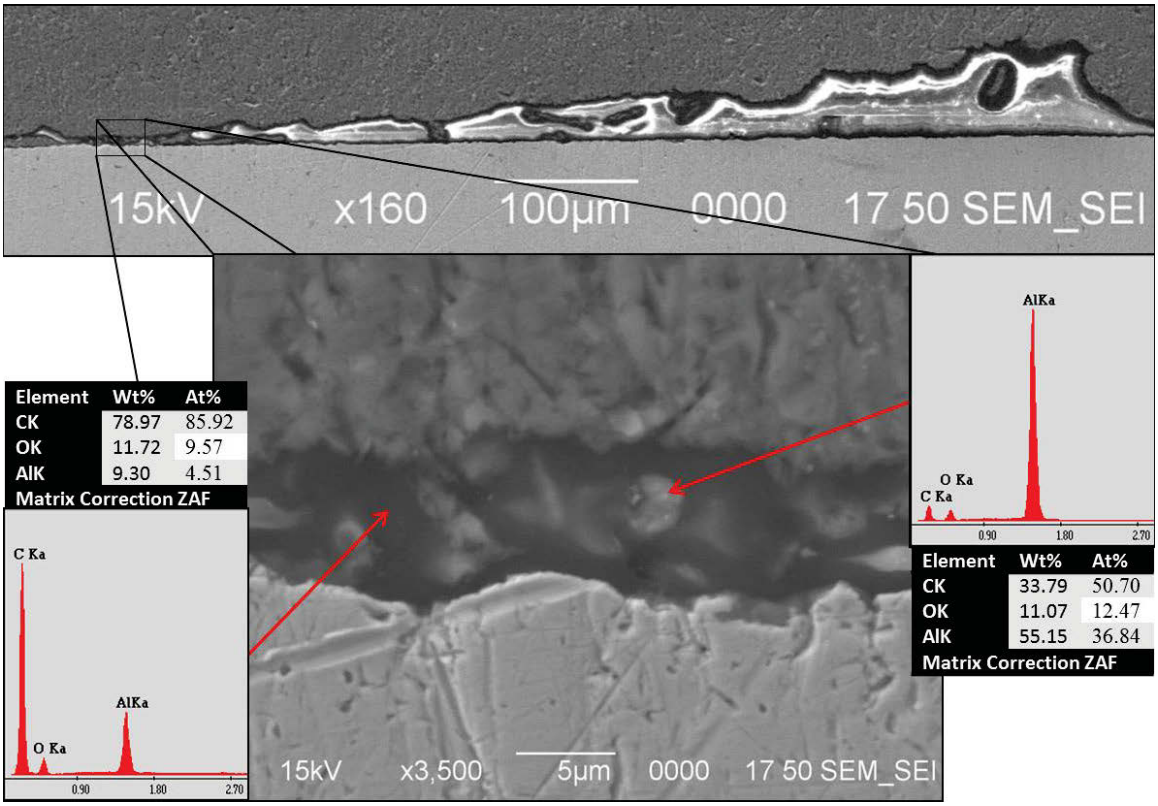

Figure 4-11: The upper image shows the large gap at the interface (where the upper material is aluminum and the lower material is brass) which had been seen previously by OM and the boxed region of the gap is expanded in the lower image. The EDS results are shown from the analysis of the lower image, where the dark area at the back of the void is shown in the left EDS analysis and one of the protruding areas is shown in the right EDS analysis.

The EDS results from this void showed that the deeper, dark areas are mostly carbon and some oxygen with a small amount of the aluminum from underneath being detected. The back of the void was not smooth, and the areas that protruded out from the back were analyzed by to show that they were aluminum, but still had a significant amount of carbon and oxygen present. These results show that the void was formed only in the aluminum side of the interface and there is a large amount of carbon in that area which

may have been the cause for the lack of bonding. This detection of carbon in the void is not conclusive of surface contaminants, since the carbon detection may be from the epoxy which this sample was mounted in.

Another void along the interface of the pink sample, one of the many which were much smaller than the larger one previously shown, was selected and analyzed as shown in Figure 4-12. This small gap was approximately 2.5μm high with a length which was hard to determine. The length of the gap itself was between 40μm to 50μm, but past this length in either direction, the interface appeared mostly unbonded. The gap itself was not very deep, since the back was mostly visible and a few particles were observed within the void. This void and the particles were analyzed by EDS. The darker backside areas of the void were analyzed, shown in Figure 4-12 A, where the aluminum was largely detected but also a large amount of oxygen and a decent amount of carbon was present. This suggests that there was a significant amount of contamination and oxidation was present at this area of the weld, which may have been the reason why bonding did not occur there. The particle in the void, Figure 4-12 B, was also analyzed by EDS. This analysis showed some of the surrounding aluminum and brass (Cu and Zn) but the particle itself was iron rich. There was also a lot of oxygen detected at this point, but it is difficult to tell whether it is oxidation on the aluminum or if the particle is iron oxide. The rest of the EDS analysis at this point showed a composition similar to the carbon-based contamination previously seen when investigating the aluminum cables. This contamination could be a factor in the cause of the void in the weld interface. It is also worthwhile to note that since the iron particle appeared to the located at the center of the gap, it may have been an influence on the poor weld in this area. It was previously

assumed that the particles embedded in the aluminum wires were from the die during the drawing process, so it may be likely that the lubricant used during drawing is around this particle and could be the carbon-based contamination seen in this void. This cannot be confirmed without analyzing the lubrication and comparing it to the contamination found in both the weld and cable samples to determine if this carbon composition is the lubrication or the epoxy.

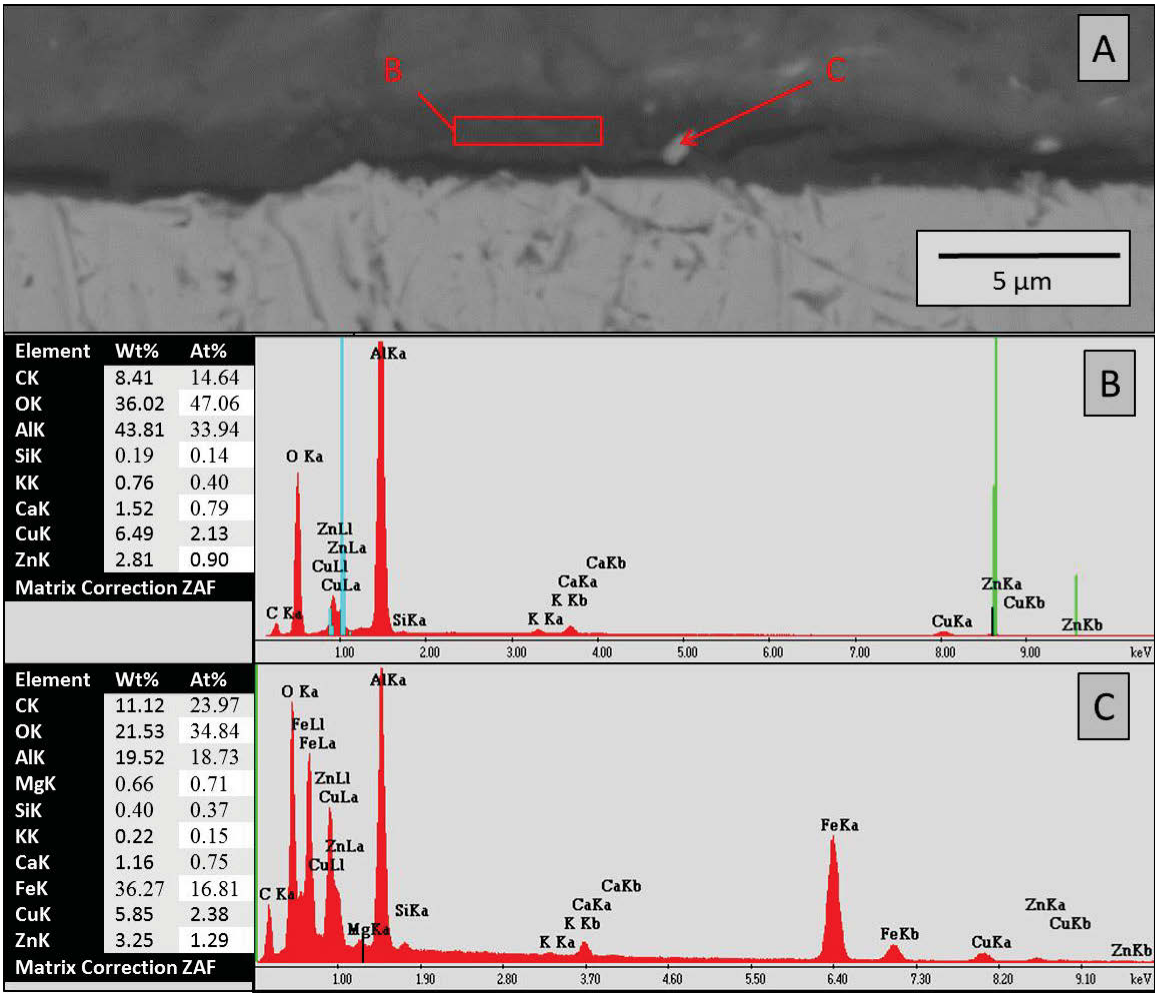

Figure 4-12: SEM backscattered image, (A), showing one of the small gaps in the weld interface. The two places analyzed were the empty area of the void, shown as B, and the particle located at the center of the void, shown as C. The corresponding EDS analysis at these points are shown below the image.

For a more detailed analysis of the terminal interface, the terminal was milled with a focused ion beam (FIB) to avoid the artifacts induced by the cutting and polishing process. The first sample prepared with this technique was the red sample. This was done by using the terminal which was not embedded in epoxy and milling straight down into the exposed interface, like the one shown in Figure 4-10 A. To make the milled face smooth, the surface was coated with a carbon deposition before milling down into the sample.

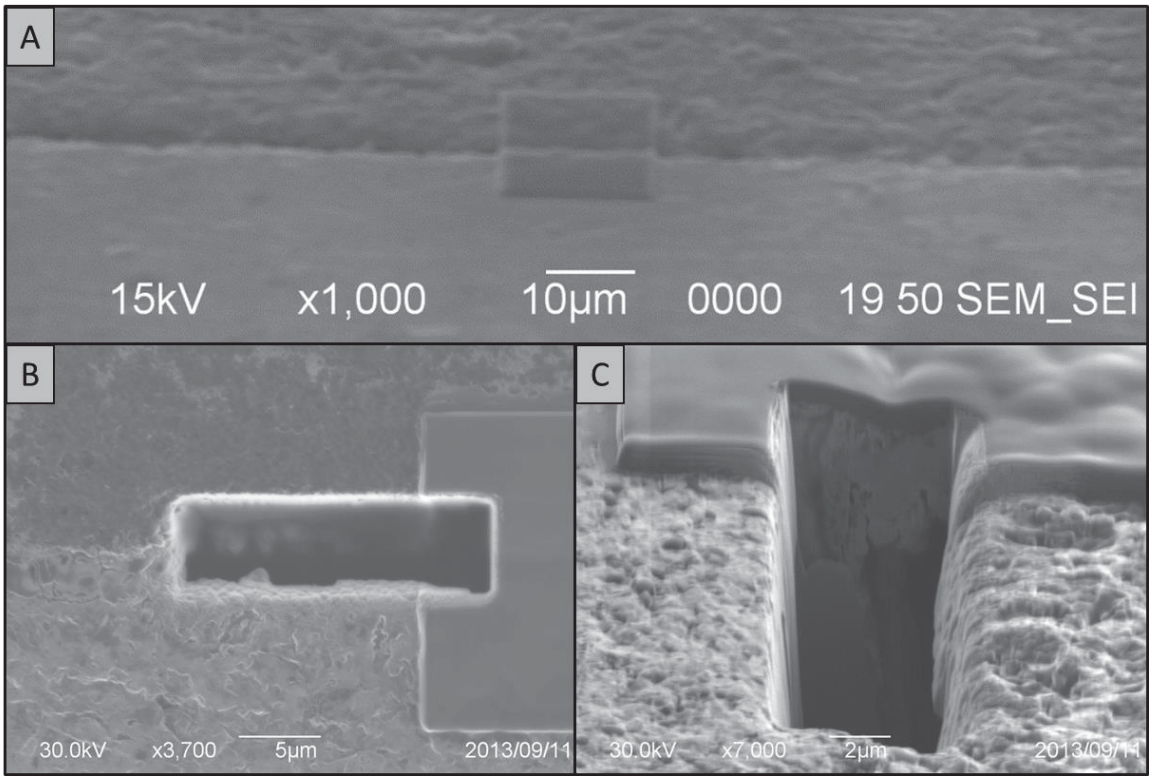

Figure 4-13: (A) SEM image of area to be milled with the carbon deposition shown in the center of the image. (B) FIB image of the milled area. (C) SEM image showing the interface after being exposed by milling with the FIB. The black area is a large void in the interface.

This milling exposed the interface of the materials, shown in Figure 4-13 C. A large void can be observed in this figure. This observation came as a surprise since the milled

sample was the red one, and no voids were previously observed in this sample by OM and SEM. This void was large enough that it extended beyond the area that was milled away, so the length could not be measured. The interface was milled slightly wider to see the full width of the void and this exposed another interesting feature, which is shown in Figure 4-14. In this Figure, where the brass was on the left of the interface and the aluminum was on the right, the void showed brass on both sides of the void rather than the void separating both metals, as would have been expected. EDS was collected around this region, shown in Figure 4-14, which supports this affirmation. The area above the void shows significant amounts of both metals which may suggest diffusion through the interface. The phenomenon of the brass appearing on both sides of the void was never discovered a second time, so the cause of this is undetermined.

Since the section milled out by the FIB revealed a large void, the sample was milled again to find out if there were more voids in the red sample, since no voids were observed by OM and SEM in the metallographically prepared red sample. To get a larger sample size without milling down into the sample multiple times, a new stage setup was configured to mill across the face so as to view a longer section of highly polished interface. This configuration included making a sample stage to hold the sample at a 45° angle so the FIB could be easily angled to mill evenly across the surface of the interface. The sample attached to the custom holder with double sided carbon tape is shown in Figure 4-15 A along the direction on which the FIB milled the sample (an SEM view of this direction and the area of interest is shown in Figure 4-15 B), and the direction the sample will be viewed to see the interface. The sample was milled across the surface with a large beam over a wide area to roughly even out the sample surface. With the large

beam size, a significant amount of curtaining effect was imposed on the sample, so further milling with a smaller beam was necessary to polish the interface.

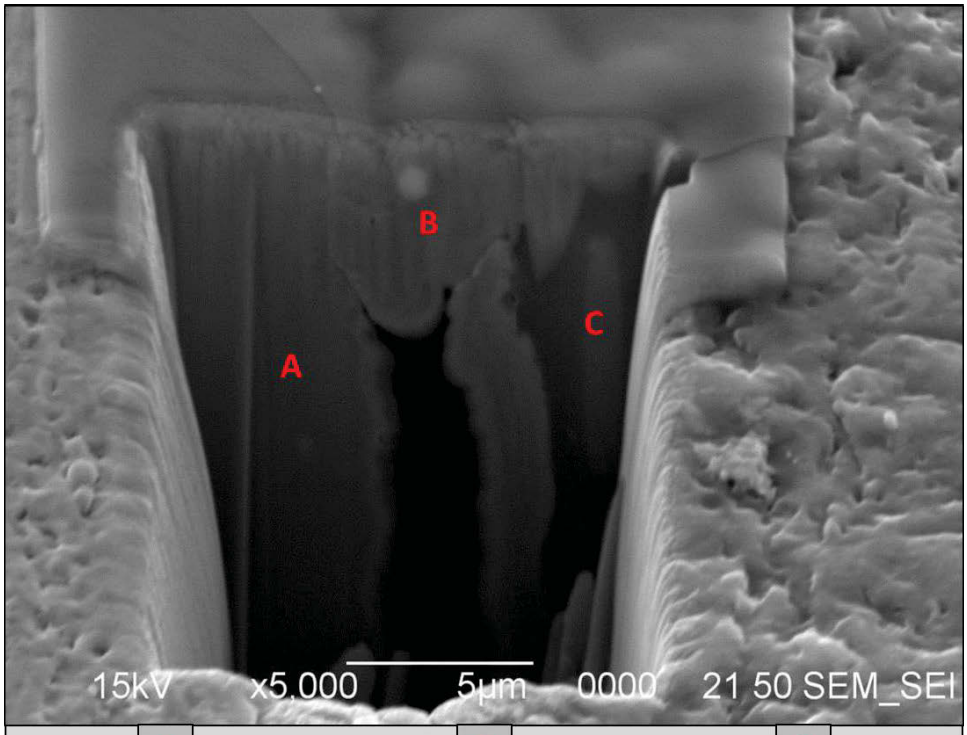

A			B			C		
Element	Wt%	At%	Element	Wt%	At%	Element	Wt%	At%
CuK	64.41	54.99	CuK	46.82	32.15	AlK	90.47	90.37
ZnK	24.44	20.28	ZnK	14.42	9.62	CuL	3.10	1.32
AlK	9.47	19.03	AlK	19.40	31.38	OK	4.49	7.56
OK	1.68	5.69	GaL	12.86	8.05	GaL	1.94	0.75
Matrix	Correction	ZAF	OK	5.31	14.49	Matrix	Correction	ZAF
			CK	1.19	4.31			
			Matrix	Correction	ZAF			

Figure 4-14: SEM image of red sample interface exposed by FIB, where the left side of the interface is brass and the right is aluminum. The black area is the open void. The EDS analysis for each of the points, A, B, and C, are respectively shown below the image.

To remove the curtaining, a small amount of carbon was deposited on the surface facing the FIB at the interface of the metals. This deposition will make the milling of the sample within the deposition area much smoother, which removes curtaining. The FIB was set to a smaller beam size and milling was performed within the area of deposition for a

significant amount of time to expose a decent area of the interface which is much smoother than before. The sample in Figure 4-15 C shows the sample after both millings.

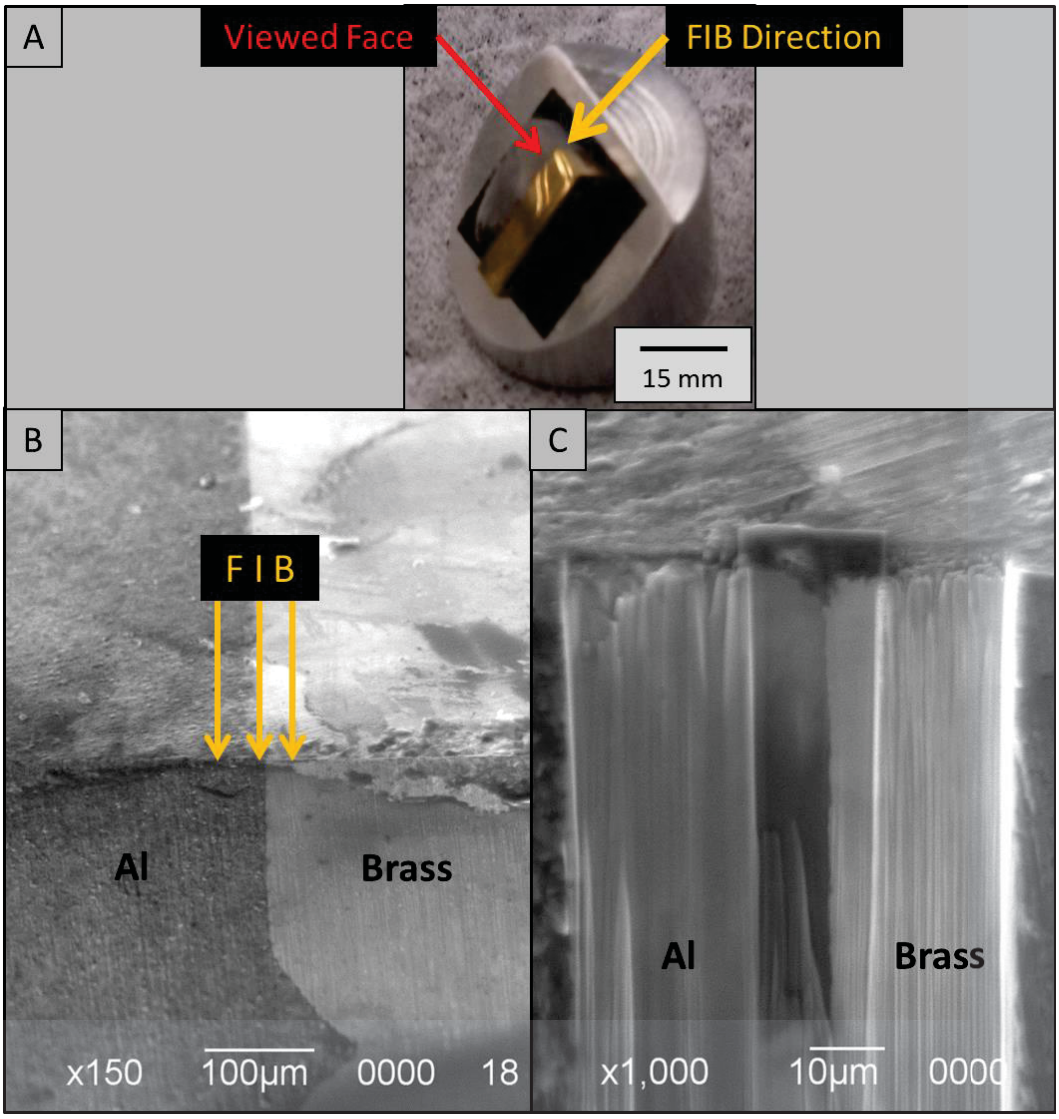

Figure 4-15: (A) Custom made sample holder with the sample attached to it. (B) SEM image of the selected area and the direction of the milling. (C) SEM image of the milled area. Curtaining effect can be observed on both sides of the wider milled section.

The smaller area in the middle of the image was polished with a small beam size and is curtaining free. The dark area above the narrow milling area is the carbon deposition. It is important to note that along this long polished section, no large voids were found, which

would suggest that the gap found during the previous FIB milling was not typical of the whole weld and discovering it was a rare circumstance.

The sample was rotated around 180° so that the FIB was directly imaging the exposed surface. Imaging with the FIB shows grains and contrast quite well, due to ion channeling contrast[39]. The exposed interface, shown in Figure 4-16 A, reveals a mixing of contrasts where the metals come together. The darker material on the left is the aluminum and the lighter material on the right is the brass, but at the interface of these two, a mixing of the two contrasts might suggest a layer of diffusion which is approximately 1-2 μm thick. A closer view of this layer is shown in Figure 4-16 B. This layer is approximately even throughout the interface except in a few places where it arcs out to be significantly thicker, as shown in Figure 4-16 C. The EDS line scan across the arcing area shows that the material is almost entirely aluminum on the left of the image and only brass across the interface. The arcing area is entirely brass. Based on this observation it seems that the interface contrast is probably due to some morphological changes of the contact surfaces during the ultrasonic welding process. The other notable features are the visible grains in the two metals. The grains are readily observed in these scanning ion images due to ion channeling contrast[39]. The grains in the brass were observed at a lower magnification, which can be clearly seen in Figure 4-16 A, but the grains in the aluminum were not clear until a higher magnification, which can be seen in Figure 4-16 B and C (the aluminum is the left material).Since it was not very clear if the mixing contrasts along the interface was due to morphological changes, it was desired to analyze the interface further with TEM. Before the analysis of the red sample by TEM, the pink terminal was FIB polished the same as the red sample to make a comparison.

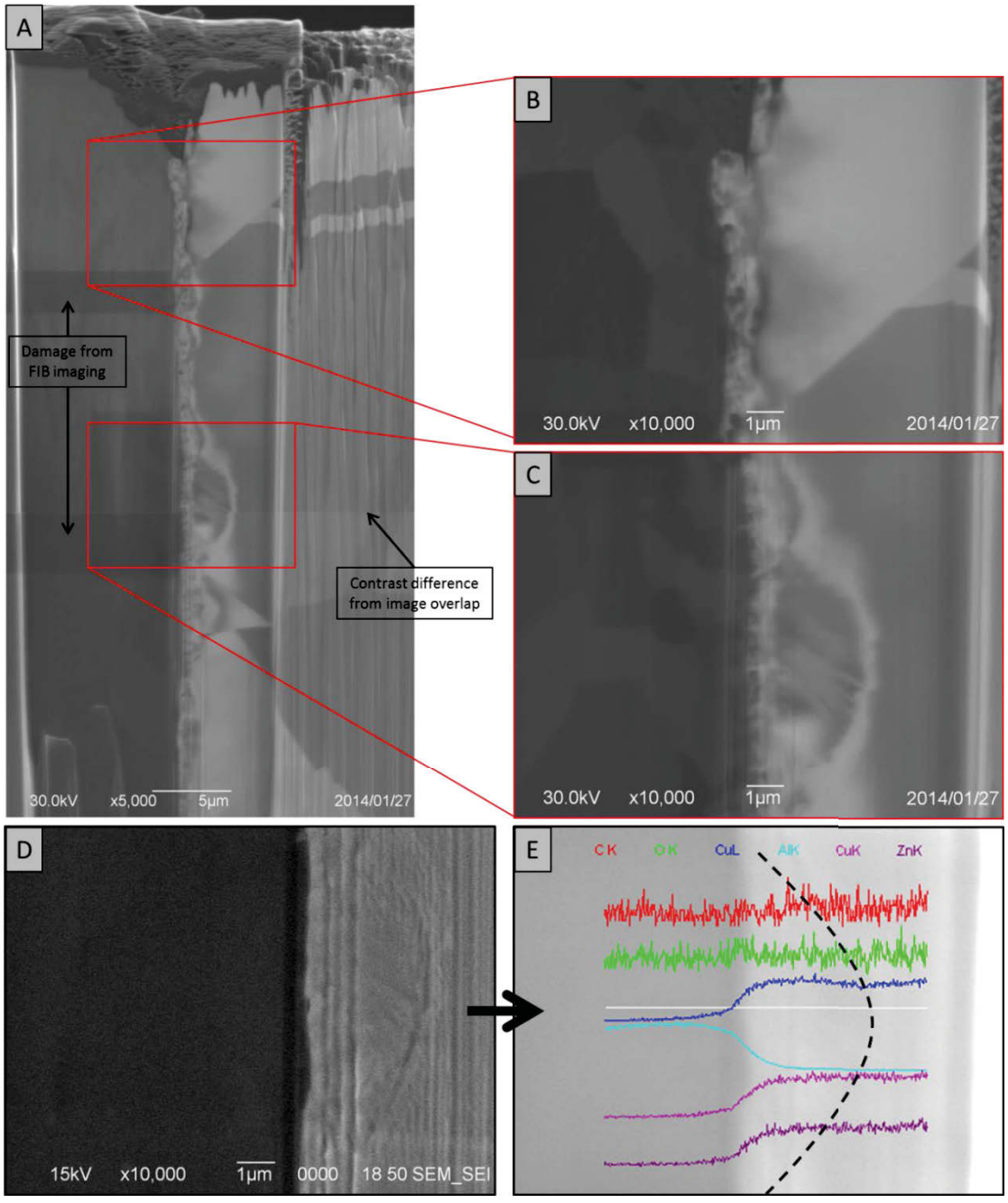

Figure 4-16: (A) Multiple FIB images overlapped to make one image showing the finely milled section of the red sample interface. Aluminum is on the left and brass is on the right. (B) Close up of the interface where the intermixing of contrast is possibly due to morphological changes of the materials at the interface following ultrasonic welding. (C) Close up of the interface where the contrasts mix further into the brass (right) than the rest of the interface. (D) SEM image of the arc shown in C. (E) EDS line scan over image D where the black dotted line approximately follows the edge of the arc. The white line is the line of scanning with the colors being the elemental composition across the scanned line coordinated with the legend at the top of the image.

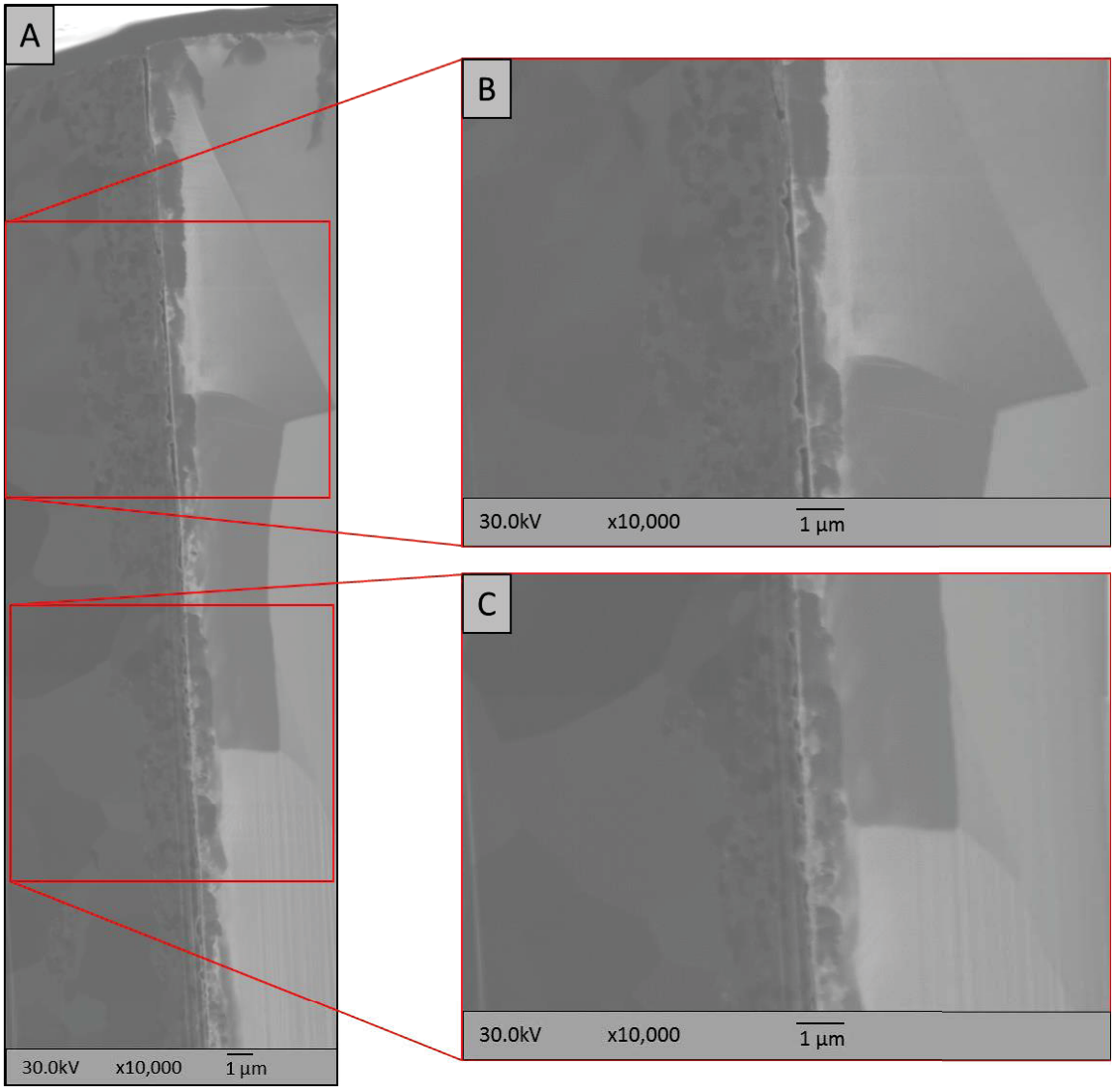

Figure 4-17: (A) Multiple FIB images overlapped to create one image of the polished interface of the pink sample. The material on the left is aluminum and the material on the right is brass. The grains can be seen quite clearly in both metals as differences in contrast. (B) and (C) show higher magnification images of the interface which has many small voids all the way along it.

The sample was prepared the same way as the red terminal sample and the result is shown in Figure 4-17 A. The grains in both metals are shown quite clearly as sharp contrast changes. The grains in the brass appear quite large and only a few are seen. However, in the aluminum, there are many grains present and they appear to get smaller

in size as they get closer to the weld interface. When comparing Figure 4-17 A (pink terminal) with Figure 4-16 A (red terminal), it is shown that the intermixing contrasts along the interface are much less mixed in the pink terminal, though there darker areas in the brass following the interface. The immediate area where the metals come together is also not smooth in the pink sample as they are in the red sample. The pink terminal interface has a much more defined edge between the metals with a large amount of small gaps that are shown throughout the length of the exposed interface, as seen in Figure 4-17 B and C. These voids show that the pink sample is much less bonded than the red sample, which would directly affect the strength of the weld. The presence of so many voids makes the creation of a TEM sample a difficult task, since a well bonded area is necessary to keep the TEM sample from falling apart when thinned, and no such well bonded area exists in the exposed interface section.

Focusing on one of the many voids in the pink terminal interface, EDS was performed on a highly magnified area, shown in Figure 4-18. The actual numerical percentages presented from this figure are not accurate due to standardless analysis, but it still shows an approximate representation of what is measured in a specific spot. This analysis shows that the material on the left side is the aluminum and on the right side is brass, which was already known, but needed confirmation. The EDS at point B shows that oxygen is present in the void, while no oxygen was measured on either side of the weld. It is still unknown whether the presence of oxide is the cause of the lack of bonding, or if the lack of bonding caused the oxide film to not be dispersed.

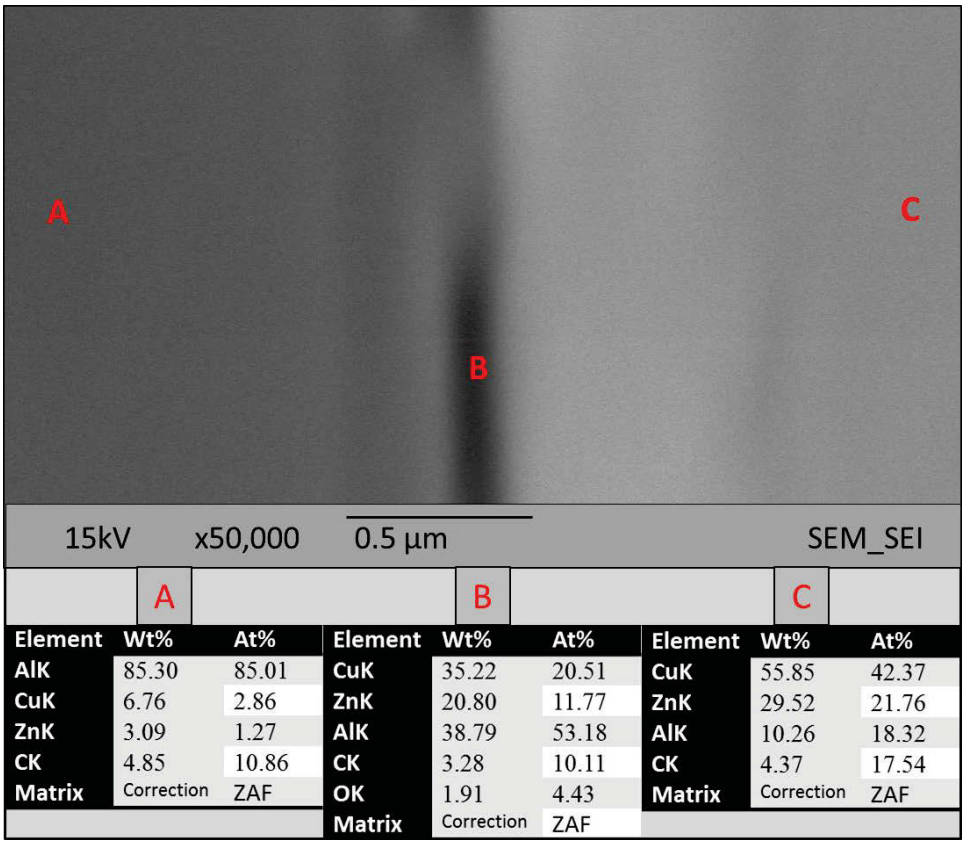

	A			B			C	
Element	Wt%	At%	Element	Wt%	At%	Element	Wt%	At%
AlK	85.30	85.01	CuK	35.22	20.51	CuK	55.85	42.37
CuK	6.76	2.86	ZnK	20.80	11.77	ZnK	29.52	21.76
ZnK	3.09	1.27	AlK	38.79	53.18	AlK	10.26	18.32
CK	4.85	10.86	CK	3.28	10.11	CK	4.37	17.54
Matrix	Correction	ZAF	OK	1.91	4.43	Matrix	Correction	ZAF
			Matrix	Correction	ZAF			

Figure 4-18: EDS analysis of one of the many gaps in the pink terminal interface. The EDS analysis shows: (A) aluminum is the left material, (C) brass is the right material, and (B) shows a small trace of oxygen in the gap that was not present in the analysis of either metal.

From the FIB polished interface comparison between the red and pink terminals, it is shown that even at a microscale the pink terminal has very little bonding of the metals, while the red terminal is quite well joined. The final investigation of the weld interface was to be performed with a TEM to obtain information on the structure of the bonding and what effects the welding process has on the materials just outside of the weld interface. Unfortunately, since a TEM sample could not be taken from the pink terminal, a comparison between the two samples cannot be made, but the TEM analysis of the red weld will offer valuable insight into the structure of the interface when bonding does occur.

The TEM sample for the red terminal was taken from the FIB polished section where the layer of contrast mixing was thin and even. The TEM sample was made as outlined in the sample preparation section; the thinned sample was viewed first in scanning transmission electron microscopy (STEM) mode with a low magnification darkfield image, as shown in Figure 4-19. The left material is the brass and the right material is the aluminum. It can

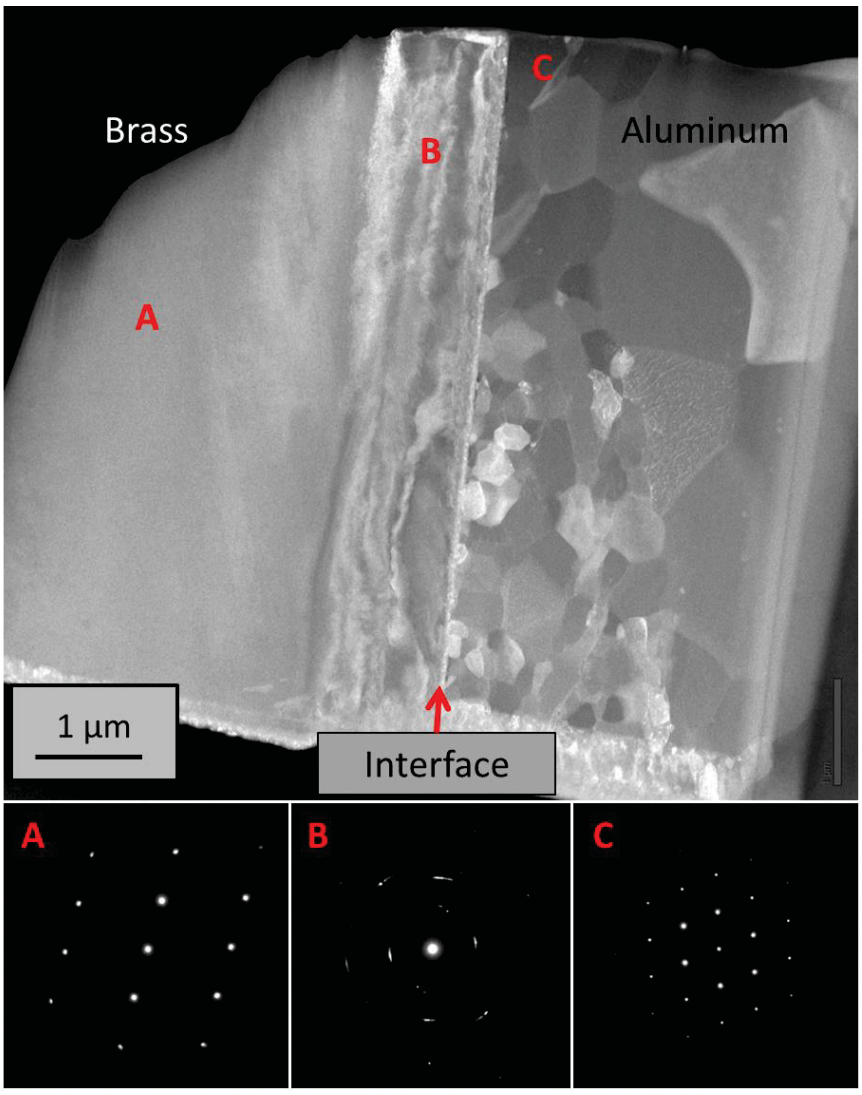

Figure 4-19: Darkfield STEM image of the entire TEM sample of the red terminal interface. SADP were taken at locations (A), (B), and (C) which are shown below the image.

be seen along the interface on the brass side, there is a quite wide layer that appears rough, having different contrast compared to the rest of the brass, as shown at Figure 4-19 B. This layer was also observed in the FIB polished sample, as discussed above, Figure 4-16 A. On the aluminum side of the sample, it is quite clear that the aluminum grains get smaller as they get closer to the interface, which has been seen before in the FIB polished pink sample. This observation correlates with results shown in literature[16,18]. The grain size reduction toward the interface is most likely caused by the forces imposed by the ultrasonic process. SADP were taken at places shown in Figure 4-19. These diffraction patterns show that at point B, in the rough-looking brass section, the brass is highly deformed where at points A (brass) and C (aluminum), the material is not deformed.

After the darkfield image analysis, high magnification analysis of the weld interface was performed. It can be seen in Figure 4-20 A that the aluminum is crystalline, evident by the structure being quite uniform, while the crystallinity on the brass side is broken up showing randomly oriented nanocrystalline grains, further suggesting that the brass is highly deformed near the interface. This image also shows that between the aluminum and the brass is a bright layer of amorphous material. This unstructured amorphous layer is what is bonding the metals together. This amorphous layer is present throughout the majority of the sample interface before it tapers off toward the right side, as shown in Figure 4-20 B.

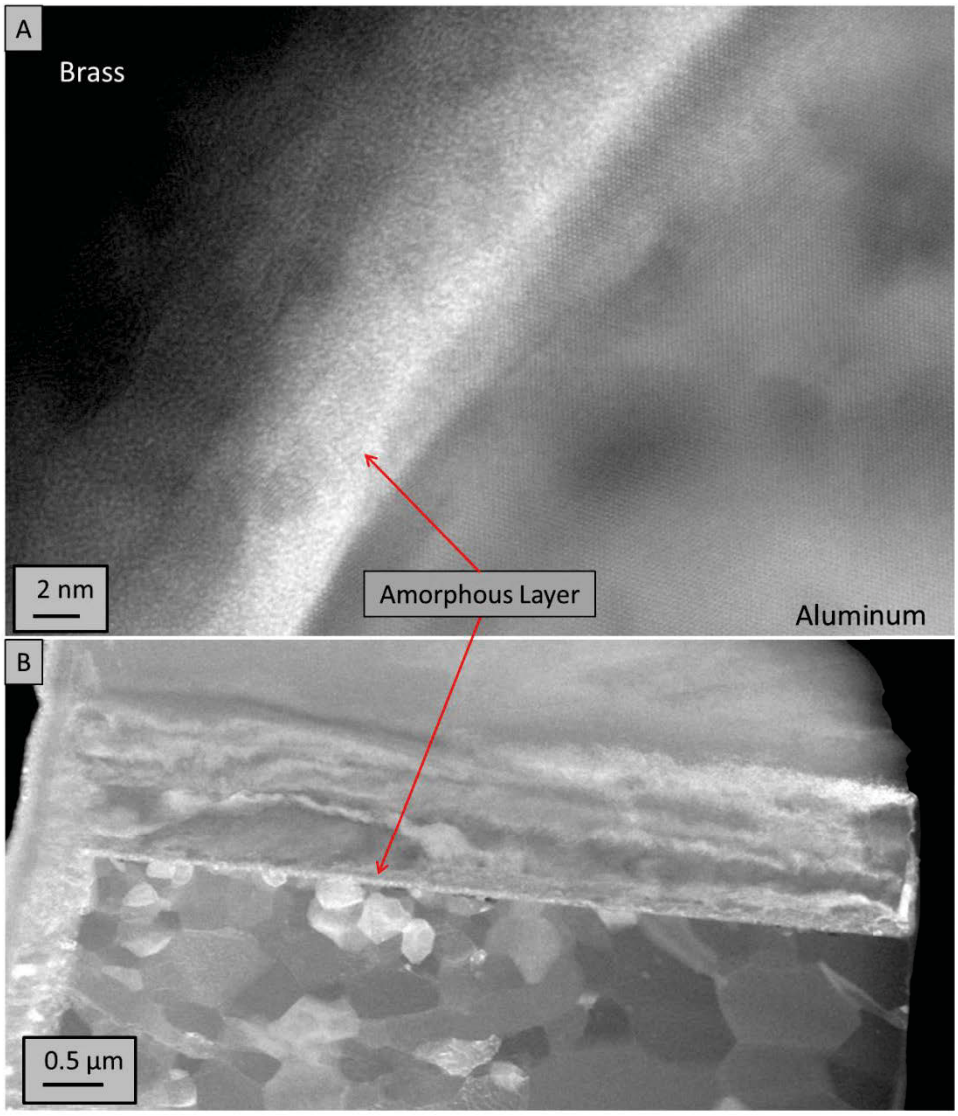

Figure 4-20: (A) High magnification TEM image of the interface where the bright band of randomly arranged structure represents a layer of amorphous material. (B) Low magnification darkfield STEM image showing the amorphous layer between the metals running through nearly the entire sample.

At a few places along the weld interface of the sample, the interface line was not quite as uniform at higher magnifications. As shown in Figure 4-21, these couple of spots along the interface showed the crystalline aluminum overlapping the white amorphous layer.

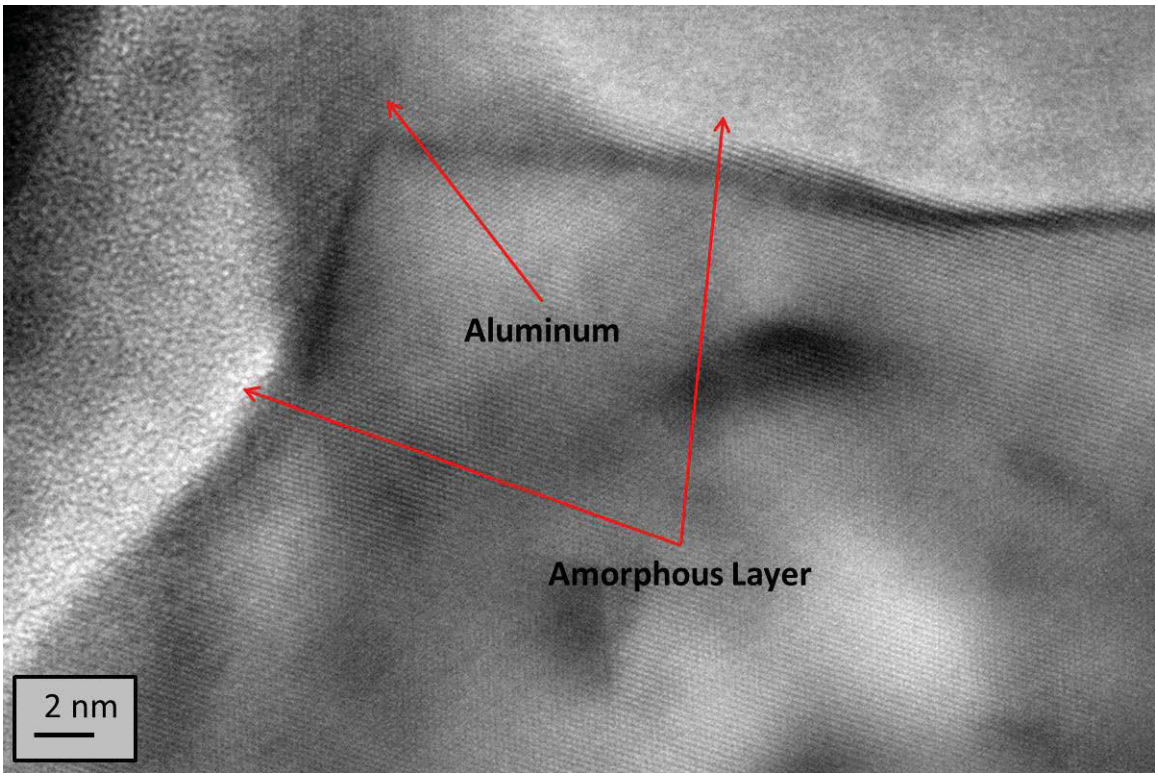

Figure 4-21: High magnification TEM image of the red sample interface showing a small area where the aluminum overlaps the amorphous layer.

Compositional analysis of the amorphous layer was performed in STEM mode with the assistance of EDS. The results are shown in Figure 4-22. The area analyzed is shown in Figure 4-22 A, and the spots where EDS was performed is shown by arrows pointing from the corresponding results, B through D. The area selected also highlights one of the only three very small voids found along the interface in the entire TEM sample. The EDS analysis at point B shows that the material is only copper and zinc, and the EDS at point D shows essentially only aluminum. The EDS analysis at the amorphous layer is shown by point C, which shows aluminum, copper, and zinc, as well as trace amounts of carbon and oxygen which were not present in the solid metals on either side if the interface layer. This finding suggests two things. First, the presence of Al, Cu and Zn in the amorphous

layer may suggest the diffusion of aluminum cable and brass terminal constituents. Second, the surface contaminants are also present in the amorphous layer and could affect the quality of the weld. For this sample, these elements are only found in small amounts, which mean that the amorphous layer is mostly a mix of aluminum, copper, and zinc. But it was found in the wire analysis that there were more contaminants in the pink sample, which leads to the assumption that the few places of bonding in the pink sample weld would have more carbon present in its amorphous bond, which could further weaken the bond.

To approximate the diffusion between the materials, which would be considered nonsteady-state diffusion, Fick's second law can be used. This law can be written as

$$\frac{\partial C}{\partial t} = \frac{\partial}{\partial x}\left(D\frac{\partial C}{\partial x}\right) \tag{4.1}$$

where C is the concentration, commonly expressed as kg/m^3, and D is diffusion coefficient expressed in m/s. The solution of this equation gives the concentration in terms of position as well as time. The diffusion coefficient is dependent on temperature, T, the diffusion activation energy, Q_d, and a temperature-independent preexponential, D_0, by the equation

$$D = D_0 \exp\left(-\frac{Q_d}{RT}\right) \tag{4.2}$$

For this expression, D_0 and Q_d are known values which are specific to the diffusion system[44].

For the diffusion found in this study, the ultrasonic welding parameters were not known, therefore without a known temperature, the diffusion cannot be modeled at this time.

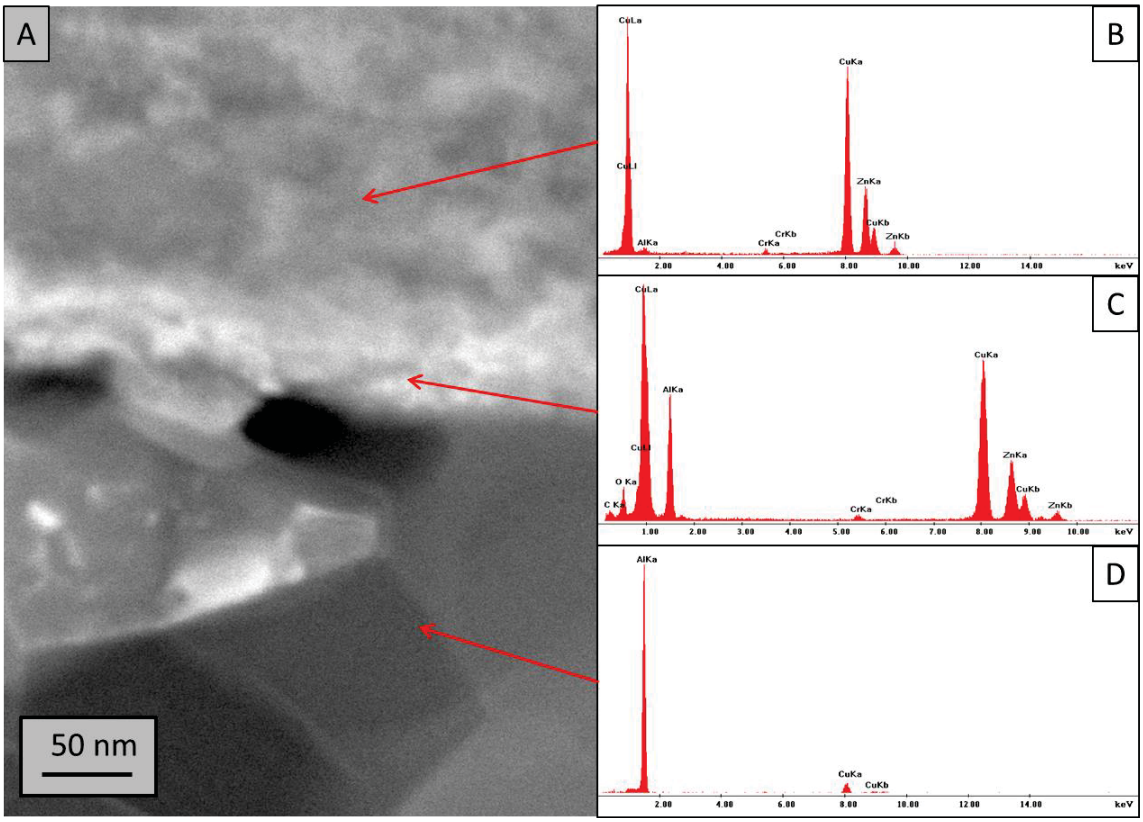

Figure 4-22: (A) High magnification darkfield image of the amorphous layer in the red sample with a small void shown in the center of the image. (B), (C), and (D) show EDS analysis at the places shown by their respective arrows.

4.1.4 Discussion

It was shown through multiple methods that the ultrasonic weld of the pink sample was unsuccessful compared to the red sample due to the numerous voids discovered at the weld interface. Based on the differences found between the red samples and pink samples, it is assumed that the cause for the poor quality of the pink sample weld is due to the roughness of the wires in the cable bundle. It is not certain whether the texture of the wires was the reason for the low quality weld or if the carbon contamination which was present in the low areas of the roughness is the cause, or even a combination of both.

It was mentioned by various sources[2] that during the ultrasonic process, surface films and oxide layers are dispersed, but it was never discussed as to what thickness of surface films becomes too thick to be dispersed. Due to this, it cannot be confirmed that the carbon contamination on the wires has any effect on the quality of the weld.

However, literature review on surface conditions for ultrasonic welds shows that the surface texture of the materials to be welded and the welder tools, does affect the strength of the weld. Since in this research, the weld samples were performed by the same ultrasonic welding apparatus, the surface quality of the welder tip and anvil would have been the same, so any differences this would create do not apply to this study. The surface condition of the welded materials is a major difference in this project, as is clearly shown in Figure 4-6. It was previously reported that the materials surface plays an essential role in the quality of the ultrasonic weld. The surface quality effect on the breaking force of the ultrasonic weld is shown in Figure 4-23. The 'smooth ground aluminum' has a rougher surface condition than 'polished aluminum'. It requires more force to break an ultrasonic weld of aluminum if the surface is smoother, especially if the electrical power input to the ultrasonic welder is higher[14]. This clearly shows that welding materials with a rougher surface creates a weld with a lower breaking strength, which is the determination of a successful weld in this research. This suggests that the poor quality of the pink weld is more due to the roughness of the aluminum wires in the cable, rather than the surface contaminants on the wires.

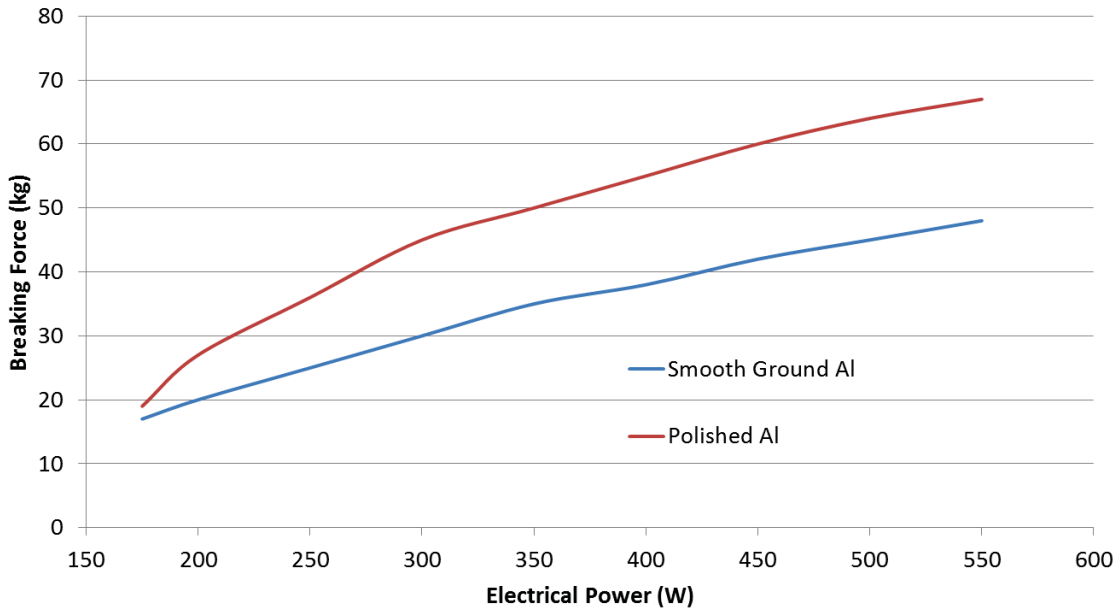

Figure 4-23: Graph showing the amount of force required to break the ultrasonic weld depending on the electrical power put into the weld. Two different welds were compared with differing surface roughness[14].

4.2 Impact Modified Polymers

4.2.1 Measuring Glass Fiber Length

The preliminary observation of the polymers was performed on the microtome slices using SEM. One microtome slice from each of the seven samples was observed. Samples 1, 3, and 5 were the unfilled bars so the SEM images showed nothing other than a uniform surface with minor scratches made by the microtome blade. Samples 2, 4, 6, and 7 were the filled samples and the SEM images are shown in Figure 4-24. The figure shows that sample 2 was filled with both fibers and beads, while samples 4, 6, and 7 were filled only with different amounts of fibers. These fibers were analyzed by EDS to confirm that they were glass. It can be also seen in Figure 4-24 that samples 6 and 7 were

cut against the direction of the fibers, showing the cross sectional area of the specimens. The important note about the images of the microtome slices is that all of the exposed fibers are broken in multiple places. This suggests that, in order to accurately measure the lengths of the glass fibers, a method which is less aggressive than mictrotomy is required.

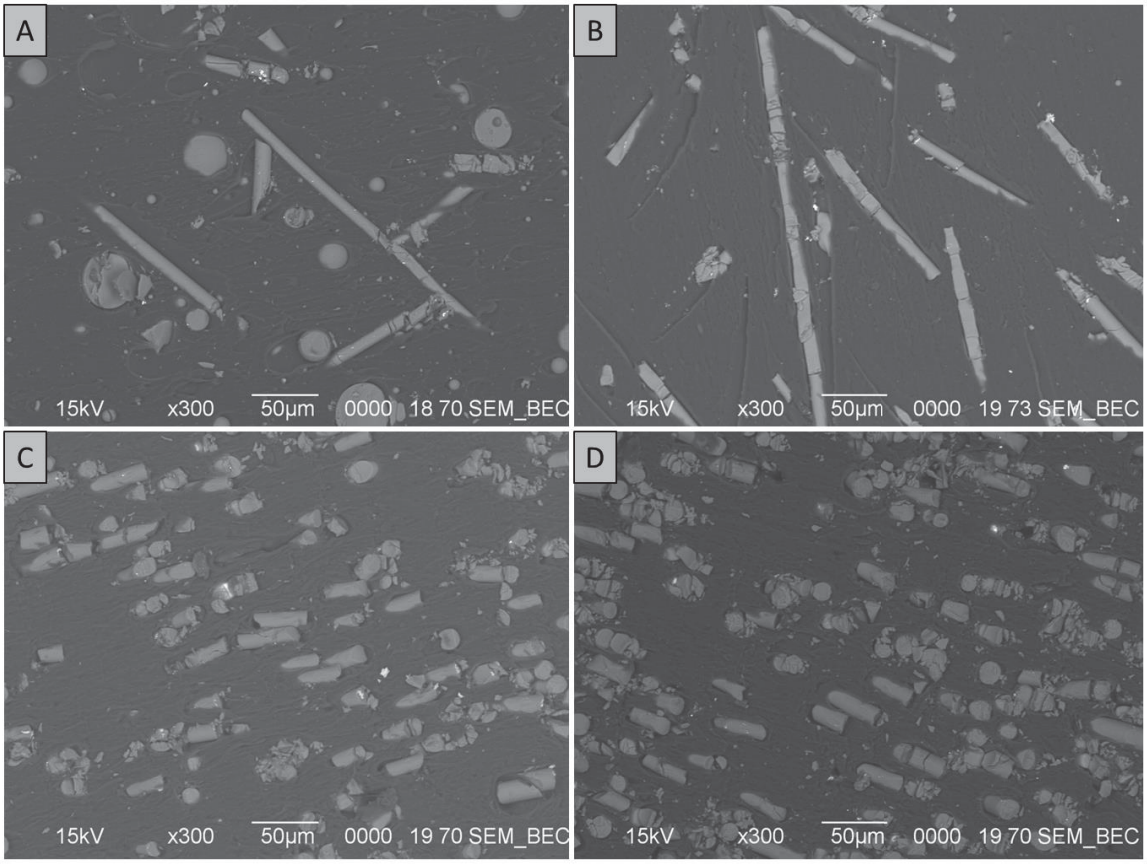

Figure 4-24: SEM backscatter images of the microtome slices (A) sample 2, (B) sample 4, (C) sample 6, (D) sample 7.

To prevent the breaking of the fibers, it was attempted to view the fibers at the surface of the polymer bar using SEM. This method failed to yield any results since very few fibers were located at the bar surface, and none of them were parallel to the surface, which is necessary to measure the full length.

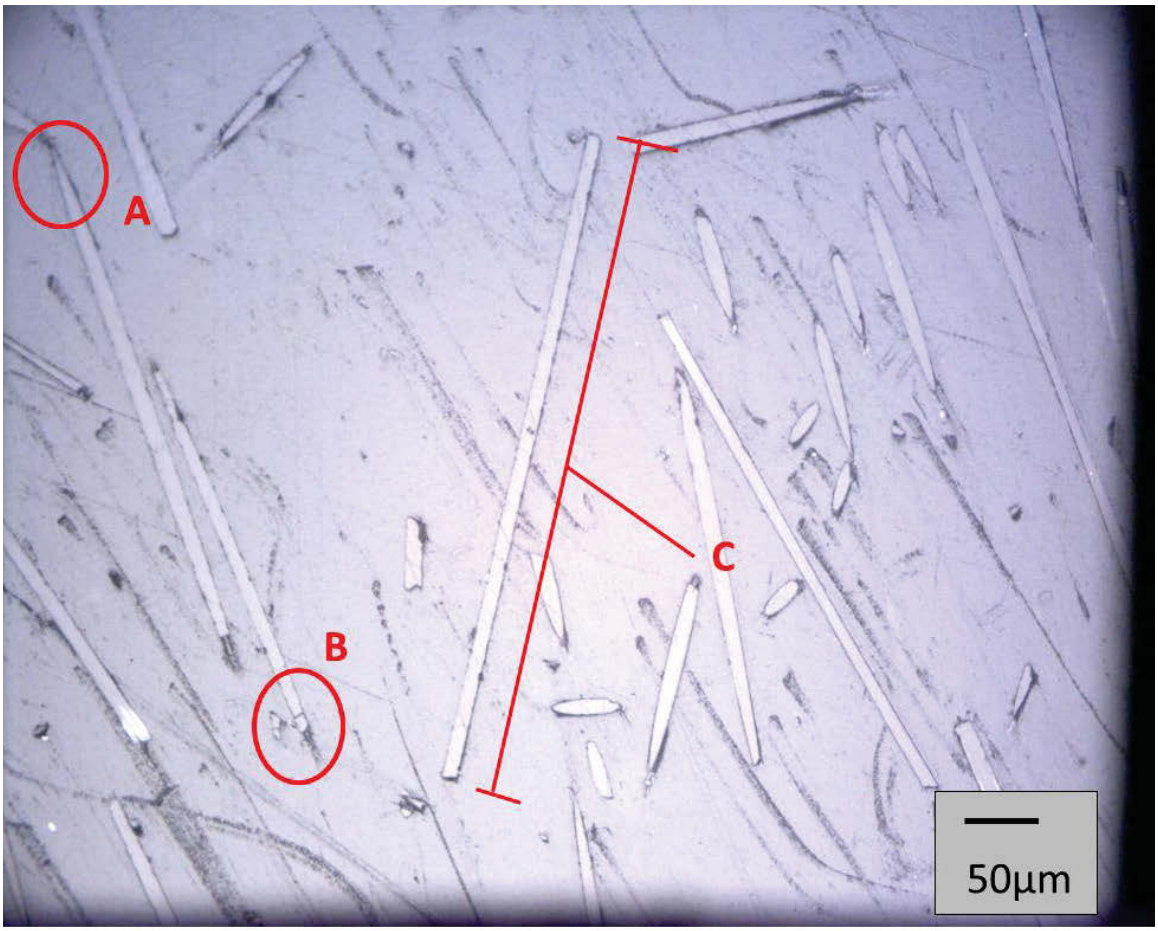

Figure 4-25: OM image showing multiple fibers from sample 4. (A) and (B) point out two separate reasons for a fiber to be excluded from measuring, while (C) shows an example of a fiber selected for measurement, which would be approximately 440 µm.

The next attempt to view the glass fibers proved more successful. Sections taken out of the polymer bars were ground and polished, then were viewed by OM. With these samples, the fiber length could be measured. To accurately measure the lengths, the visible fibers had to be carefully selected. The fiber was excluded from being measured if either end of the fiber was pointed or broken off, as shown in Figure 4-25 A and B, respectively. These both signify that the fiber is not quite parallel to the viewing surface; a pointed fiber end occurs when the fiber recedes below the polymer part of the surface, while a broken end occurs when the fiber would have continued upward into the polymer

that was ground away, which caused the brittle glass fiber to break. There were actually two kinds of broken tips: the first having an absence of polymer where the fiber would have continued, signifying that the fiber broke away after the polymer had hardened (during the grinding/polishing sample preparation), and the second type having the polymer tightly packed around it, signifying that the fiber broke before the polymer solidified (during the making of the polymer bar). The first broken type was the one excluded from the fiber measurement selection process.

Using this method and selection criteria, the glass fiber lengths were measured for samples 2 and 4, which were the two filled nylon samples. When polishing sample 6 and 7, the PBT samples, the glass fibers were completely shattered, making accurate measurements impossible. The polishing was repeated multiple times, and each time the fibers were observed to be completely broken. These fibers were broken during the grinding and polishing process since there were always voids where the shards were carried away, indicating that they were not broken during the creation of the polymer bars, otherwise the fiber pieces would have been surrounded by polymer. This fiber shattering may have been due to the fact that the PBT is a harder polymer than the nylon and therefore may have carried the impacts from the grinding into the fibers and breaking them, rather than absorbing the impacts like the softer nylon might have done. For the nylon samples, slightly over 20 fiber measurements were taken. These averages are listed in the table below.

Table 2: Average lengths for the measured glass fibers.

Sample #	Base Polymer	Average Fiber Length (μm)
2	PA6	387
4	PA66	493

The company which supplied this project had expected fiber lengths between 800 μm and 5000 μm, which is a significantly higher range than what was measured. This data would suggest that the glass fibers are broken down during the creation process of the polymer or during the injection molding process.

4.2.2 Viewing the Polymeric Domains

To expose the polymeric domains of the seven polymer samples, each sample was plasma etched as outlined in the experimental section. After etching, the samples were first viewed using OM. For the unfilled polymers, sample 1, 3, and 5, OM showed a definite texture across the polymer surface which was not present before the etching. The comparison of the surface can be seen in Figure 4-26 A and B. Higher magnification images were also taken with OM, as shown in Figure 4-26 C, but using the SEM at approximately the same magnification showed better resolution and better definition of the texture, as shown in Figure 4-26 D.

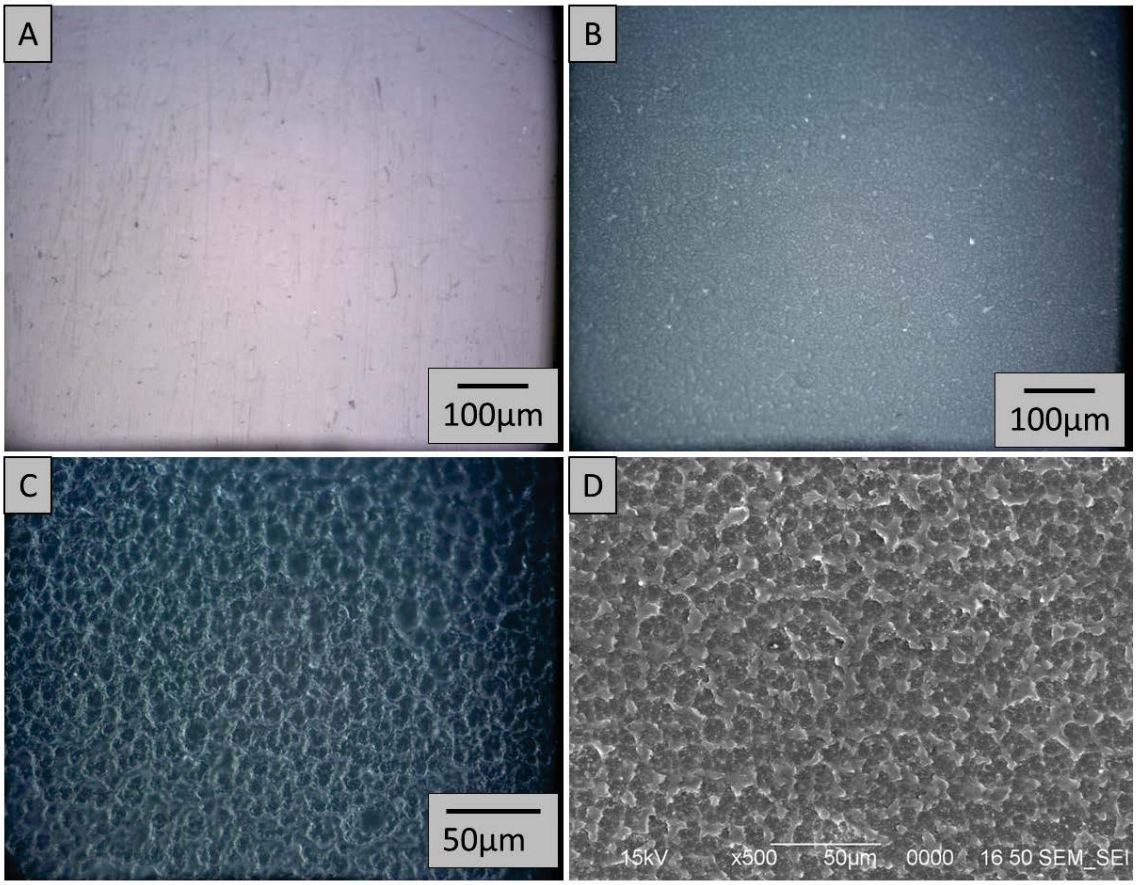

Figure 4-26: OM images of the surface of sample 1 (PA6 unfilled) before etching (A) and after etching (B) show texture differences. (C) OM darkfield image of sample 1 at higher magnification. (D) SEM image of sample one showing a better definition of the texture.

For higher magnification than the OM could achieve, the plasma etched surface was analyzed in the SEM. Figure 4-27 shows each sample, except sample 2, at a magnification high enough to observe the details of the texture and also avoid interference from the glass fibers in the filled samples. In sample 2, the glass fibers and beads were so abundant that it was difficult to find an area which displayed only the etched texture in the polymer without a fill particle obstructing the view. As shown in Figure 4-27 A and B, the etched textures of unfilled PA6 and PA66, which are both nylon

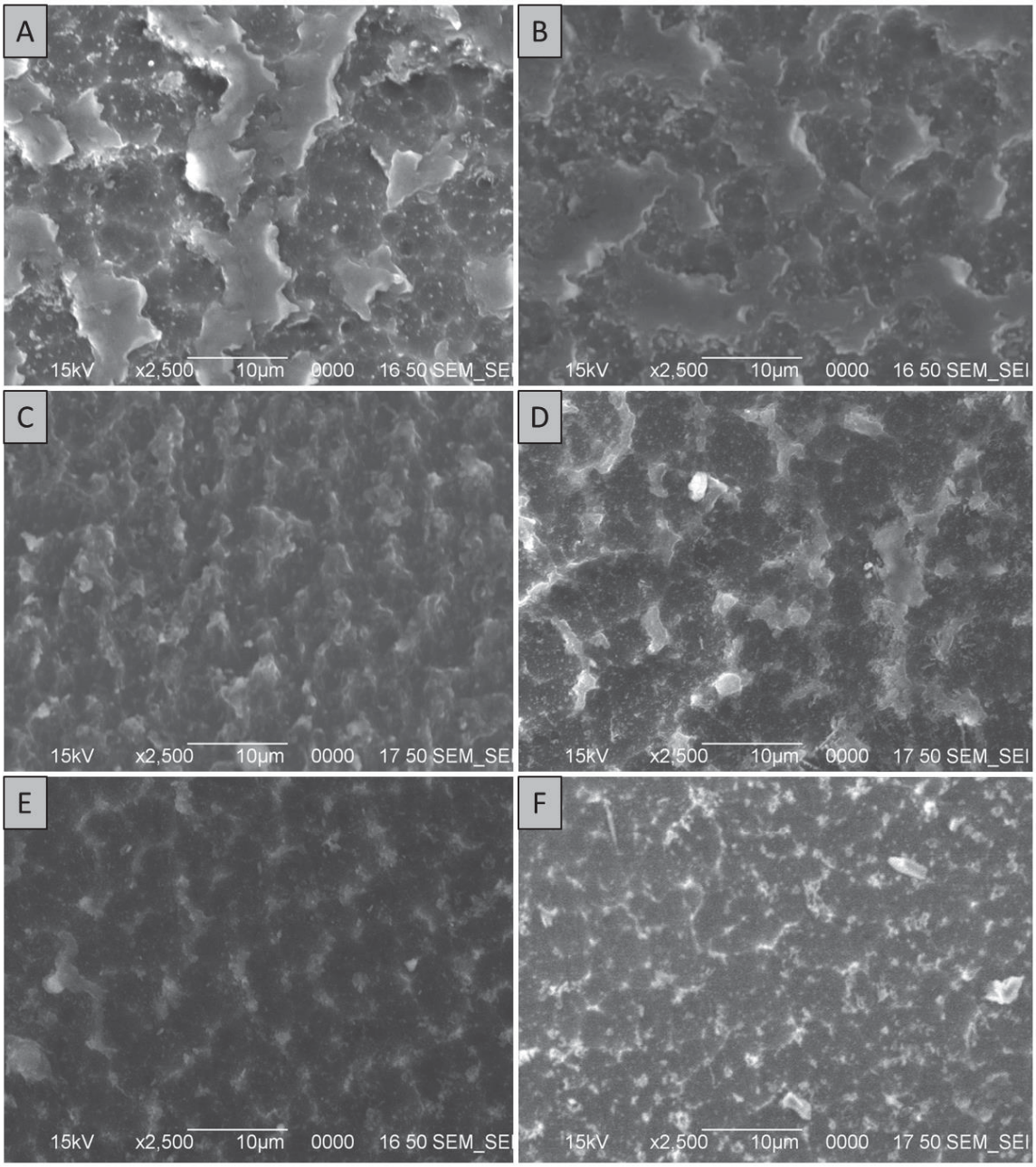

Figure 4-27: SEM images of the etched surface of: (A) sample 1, (B) sample 3, (C) sample 4, (D) sample 5, (E) sample 6, and (F) sample 7. For the glass fiber filled samples, these images were taken between any fill particles to give a good comparison between samples. For this reason, sample 2 is not shown because it contained so many glass fibers and beads that it was difficult to see an area of the etched polymer without interference from fill.

based polymers, appear nearly identical. However, in the PA66 with 14% fill, the raised portions appeared thinner and less massive (Figure 4-27 C). The unfilled PBT, shown in

Figure 4-27 D, had less raised portions which were much thinner than what was seen in the unfilled nylon based polymers. The raised sections were even lower and thinner in both of the filled PBT samples (Figure 4-27 E and F), compared to the already low and thin unfilled PBT. With the current data it is difficult to determine the different domains in the polymer samples. Regardless, it appears that whatever the raised section is, there is more of it in the nylon based polymers than in the PBT based polymers. There also seems to be less of the raised material when more fill is present in the polymer, as is shown that the raised areas are less massive in the filled PA66 than in the filled PA66. The same trend also appears in the PBT samples, as there seems to be less raised sections in the 20% filled PBT than the unfilled PBT, and possibly even less than that in the 30% filled PBT.

While it is possible that the texture brought out by plasma etching was just an artifact and not the polymeric domains, the etching showed two very different textures between the nylon based polymer and PBT based polymer. The comparison in Figure 4-28 of the unfilled PA6 and the unfilled PBT shows definite differences between the etched samples. It seems reasonable that the less etched domain would be the base material since the blended impact modifier should likely be a tougher material considering the purpose of it is to ‘harden’ the polymer. If this is the case, the fact that the raised sections are thinner and more spread out in the PBT would suggest that the impact hardener blended into it is more distributed through the base polymer than the nylon, or there is less of it altogether.

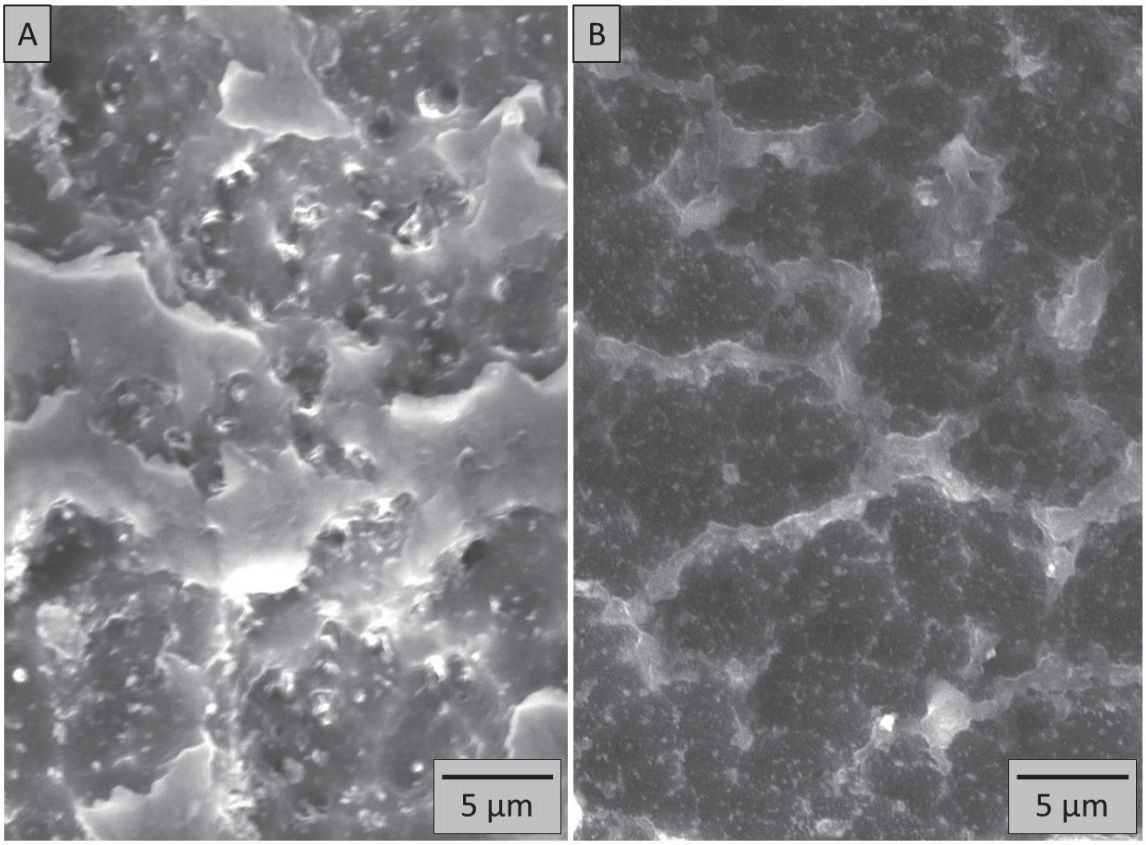

Figure 4-28: High magnification SEM images of the etched surface of the unfilled nylon based polymer (A), and the unfilled PBT polymer (B).

CHAPTER 5: CONCLUSION

5.1 Aluminum Cables and Ultrasonic Welds

Various analytical techniques have been used to study the aluminum cables and the ultrasonic welds, to determine the causes of failure between two sets of samples. Through the analysis of the first six aluminum cables, which are composed of bundles of aluminum wires, it was determined that in most respects, the wires of the cable were quite similar. The XRD analysis showed all the cables samples to be annealed after drawing, which means that they all exhibited typical, non-elongated, equiaxial grains. The observations by SEM showed that all of the cables had slightly varying amounts of embedded particles in the surfaces of the wires, though the amount of these particles is small enough to have a negligible effect on ultrasonic welding characteristics. The SEM analysis also showed small amounts of oxidation and carbon contamination in all samples. The AES investigation shows that the samples had varying thicknesses of carbon contamination and oxide layers on the wire surfaces. It was found through literature that these surface layers have no effect on the ultrasonic weld, unless the layers are significantly high, which was not the case in this projects samples.

What was found to be significant was the work piece surface roughness. The pink cable (which was the cable used for the ‘unsuccessful weld’) had a majority of wires with surfaces showing very significant roughness. This roughness on the wire surface was compared to the very smooth wires in the red cable, which was used in the ‘successful weld’. This result was confirmed through literature, that the surface quality of the welded

parts affects the strength of the weld, where rough surfaces on the parts make for poor welds.

The terminals were cut apart to expose the interface to see what effect the different conditions had on the bond between the metals. By analyzing the weld interfaces with OM and SEM, it was found that the pink sample weld had several large voids along the interface. By FIB polishing, submicron sized voids were also observed in the pink sample. By comparison, the red sample weld had no visible voids, large or small.

The red sample weld interface was analyzed by TEM to observe how a successful weld of aluminum to brass appeared at high magnification. The TEM results show significant deformation in the brass, which is assumed to have been brought on by the ultrasonic welding process. The aluminum was also affected by the welding, but differently than the brass: the aluminum grains were shown to decrease in size as they approached the weld interface. This result was confirmed in various literature accounts. At the interface of the weld, the crystalline structure completely disappeared, where an amorphous layer was observed. This amorphous layer along the interface was shown to follow the entire length of the TEM sample, and it was shown by EDS to contain both aluminum, copper, and brass. This diffusion amorphous layer is what was found to be the bond between the two metals.

5.2 Impact Modified Polymers

For the impact modified polymers, the goal was to find the lengths of the glass fibers which were used to fill the polymer blend, as well as to expose and image the different

domains in the blend. The fiber lengths were ultimately measured using OM after a moderate amount of polishing the sample surface. Only the fibers in the two nylon based polymers, PA6 and PA66, were able to be measured, due to the fibers in the PBT samples being shattered no matter the amount of fine polishing. The company which extended this project, had expected the fibers in the polymer to be between 800 μm and 5000 μm, but the average of the measured fiber lengths were 387 μm and 493 μm for the PA6 and PA66, respectively. Obviously these measurements were significantly lower than what was expected, suggesting that the fibers were broken down more during the processing of the polymers than was anticipated.

For viewing the polymeric domains, the samples were eventually decided to be etched via plasma etching, and the etched surface was observed in OM and SEM. The SEM provided the resolution to see the exposed texture at high magnifications. It was found that the texture for the two nylon based polymers appeared to be the same, and specific regions appeared to become thinner in the samples with more glass fiber fill. The PBT samples showed the same type of texture, although in the PBT sample, there appeared to be less raised regions and they were smaller. The same trend of smaller raised features in samples with more glass fiber fill continued with the PBT samples. In the present work it was not possible to determine whether the texture on the plasma etched samples was actually representative of the polymeric domains or if they were simply artifacts induced by the etching process. This issue could be further investigated using field emission SEM and TEM imaging techniques.

CHAPTER 6: REFERENCES

1. Matsuoka, S. and Imai, H. (2009). Direct Welding of Different Metals Used Ultrasonic Vibration, Journal of Materials Processing Technology, vol. 209(2), 954-960.
2. Kaiser Aluminum (1978). Welding Kaiser Aluminum. Second Edition. Kaiser Aluminum & Chemical Sales, Inc.
3. Balle, F., Huxhold, S., Wagner, G. and Eifler, D. (2011). Damage Monitoring of Ultrasonically Welded Aluminum/CFRP-Joints by Electrical Resistance Measurements, Procedia Engineering, vol. 10, 433-438.
4. Zhou, B., Thouless, M.D. and Ward, S.M. (2006). Predicting the Failure of Ultrasonic Spot Welds by Pull-Out from Sheet Metal, International Journal of Solids and Structures, vol. 43(25-26), 7482-7500.
5. Magniez, K., Fox, B.L. and Looney, M.G. (2009). Silver Sulfide as a Staining Agent for Scanning Electron Microscopy of Nylon 6/MXD6 Blends, Polymer International, vol. 58(8), 858-862.
6. Sawyer, L., Grubb, D. and Meyers, G.F. (2008). Polymer Microscopy. Third Edition. New York, NY: Springer Science+Business Media.
7. Copper Prices and Copper Price Charts [Internet]. Available from http://www.infomine.com/investment/metal-prices/copper/
8. Aluminum Prices and Price Charts [Internet]. Available from http://www.infomine.com/investment/metal-prices/aluminum/
9. Pryor, L., Schlobohm, R. and Brownell, B. A Comparison of Aluminum vs Copper as Used in Electrical Equipment [Internet]. GE. Available from http://www.geindustrial.com/sites/geis/files/gallery/White%20paper%20-%20Aluminum%20vs.%20copper%205-08.pdf
10. Weigl, M., Albert, F. and Schmidt, M. (2011). Alternative Methods to Increase the Long Term Performance of Laser-Welded Copper Aluminum Connections for Electronic Applications in Mobile Systems, Automotive Technologies, 39-47.

11. Neppiras, E.A. (1965). Ultrasonic Welding of Metals, Ultrasonics, vol. 3(3), 128-135.
12. Shakil, M., Tariq, N.H., Ahmad, M., Choudhary, M.A., Akhter, J.I. and Babu, S.S. (2014). Effect of Ultrasonic Welding Parameters on Microstructure and Mechanical Properties of Dissimilar Joints, Materials & Design, vol. 55, 263-273.
13. Astashev, V.K., Babitsky, V.I. and Khusnutdinova, K. (2007). Ultrasonic Processes and Machines. Springer Berlin Heidelberg.
14. Daniels, H.P.C. (1965). Ultrasonic Welding, Ultrasonics, vol.3(4), 190-196.
15. Elangovan, S., Semeer, S. and Prakasan, K. (2009). Temperature and Stress Distribution in Ultrasonic Metal Welding-An FEA-Based Study, Journal of Materials Processing Technology, vol. 209(3), 1143-1150.
16. Kenik, E.A. and Jahn, R. (2003). Microstructure of Ultrasonic Welded Aluminum by Orientation Imaging Microscopy, Microscopy and Microanalysis, vol. 9(S02), 720-721.
17. Kim, B.K. and Szpunar, J.A. (2001). Orientation Imaging Microscopy for the Study on High Temperature Oxidation, Scripta Materialia, vol. 44, 2605-2610.
18. Allameh, S.M., Jahn, R. and Soboyejo, W.O. (2003). Microstructual Characterization of Ultrasonically Welded Aluminum, Ford Scientific Laboratory.
19. Mark, J.E. (1999). Polymer Data Handbook. Oxford, NY: Oxford University Press.
20. Borggreve, R.J.M. and Gaymans, R.J. (1989). Impact Behaviour of Nylon-Rubber Blends: 4. Effect of the Coupling Agent Maleic Anhydride, Polymer, vol. 30(1), 63-70.
21. Lievana, E. and Karger-Kocsis, J. (2003). Impact Modification of PA-6 and PBT by Epoxy-Functionalized Rubbers, Macromolecular Symposia, vol. 202(1), 59-66.
22. Peng, J., Qiao, J., Zhang, S. and Wei, G. (2003). A Novel Impact Modifier for Nylon 6, Macromolecular Materials and Engineering, vol. 287(12), 867-870.
23. Wong, S.C. and Mai, Y.W. (1999). Effect of Rubber Functionality on Microstructures and Fracture Toughness of Impact-Modified Nylon

66/polypropylene Blends: 1. Structure-Property Relationships, Polymer, vol. 40(6), 1553-1566.

24. Borggreve, R.J.M., Gaymans, R.J. and Eichenwald, H.M. (1989). Impact Behaviour of Nylon-Rubber Blends: 6. Influence of Structure on Voiding Processes; Toughening Mechanism, Polymer, vol. 30(1), 78-83.
25. Borggreve, R.J.M., Gaymans, R.J., Schuijer, J.F. and Housz, I. (1987). Brittle-Tough Transition in Nylon-Rubber Blends: Effect of Rubber Concentration and Particle Size, Polymer, vol. 28(9), 1489-1496.
26. Borggreve, R.J.M., Gaymans, R.J. and Schuijer, J.F. (1989). Impact Behaviour of Nylon-Rubber Blends: 5. Influence of the Mechanical Properties of the Elastomer, Polymer, vol. 30(1), 71-77.
27. Qin, S.H., Yu,J., Zheng, Q., He, M. and Zhu, H. (2008). The Effect Of Blending Sequence On Phase Morphology Of Nylon 6/ABS/SMA Blends. 高分子科学, *26*(1), 73-80.
28. Mamat, A., Vu- Khanh, T., Cigana, P., and Favis, B. D. (1997). Impact Fracture Behavior Of Nylon- 6/ABS Blends. Journal Of Polymer Science Part B: Polymer Physics, 35(16), 2583-2592.
29. Qin, S. H., Yu, J., Zheng, Q., He, M., And Zhu, H. (2007). Morphology And Mechanical Properties Of Nylon 6/PBT Blends Compatibilized With Styrene/Maleic Anhydride Copolymer. Chemical Research in Chinese Universities, 23(6), 726-732.
30. El Wakil, S.D. (1998). Processes and Design for Manufacturing, Boston, MA: PWS Publishing Company.
31. Y. Leng (2008). Materials Characterization, John Wiley and Sons Inc.
32. Skoog, D.A., Holler, F.G. and Crouch, F.A. (1998). Principles of Instrumentation Analysis. Fifth Edition. Brooks Cole.
33. Goodge J. Energy-Dispersive X-Ray Spectroscopy (EDS) [Internet]. [2013 Dec 14]. Available from: http://serc.carleton.edu/research_education/geochemsheets/eds.html
34. Abramowitz, M. and Davidson, M.W. Microscope Objectives: Numerical Aperture and Resolution. [Internet]. [2004 Apr 22]. Available from: http://micro.magnet.fsu.edu/primer/anatomy/numaperture.html.
35. Auger Electron Spectroscopy (AES) [Internet]. [2010 Oct 17]. Available from: http://wiki.utep.edu/display/~ckroy/Auger Electron Spectroscopy (AES).

36. Hoffman, S. (2013). Auger and X-Ray Photoelectron Spectroscopy in Materials Science. Springer Series in Surface Sciences.
37. Rangel, V.R. Auger Electron Spectroscopy (AES) [Internet]. [2010 Oct 12]. Available from: http://wiki.utep.edu/pages/viewpage.action?pageId=39193859.
38. Voutou, B. and Stefanaki, E. Electron Microscopy: The Basics (2008). [Internet]. Available from: http://optiki.files.wordpress.com/2013/03/electron-microscopythe-basics.pdf.
39. Giannuzzi, L. A. and Stevie, F. A. (2005). Introduction To Focused Ion Beams: Instrumentation, Theory, Techniques And Practice. Springer.
40. Volkert, C. A. and Minor, A. M. (2007). Focused Ion Beam Microscopy and Micromachining. MRS Bulletin, 32(05), 389-399.
41. Castillo, R.C. (2013) Functional Nanostructure Fabricated by Focused Electron/Ion Beam Induced Deposition. Doctoral Thesis, University of Zaragoza, Spain.
42. Williams, D. B. and Carter, C. B. (1997). Transmission Electron Microscopy: A Textbook For Materials Science. Micron, 28(1), 75-75.
43. Cullity, B.D. (1967). Elements of X-Ray Diffraction. Addison-Wesley Publishing Company, Inc.
44. Callister, W. D. and Rethwisch, D. G. (2010). Materials Science and Engineering an Introduction. John Wiley & Sons, Inc.